

# GAMMA-RAY LINES FROM ASYMMETRIC SUPERNOVAE

by

Aimee Louise Hungerford

---

A Dissertation Submitted to the Faculty of the  
DEPARTMENT OF ASTRONOMY

In Partial Fulfillment of the Requirements  
For the Degree of

DOCTOR OF PHILOSOPHY

In the Graduate College

THE UNIVERSITY OF ARIZONA

2004

UMI Number: 3145077

### INFORMATION TO USERS

The quality of this reproduction is dependent upon the quality of the copy submitted. Broken or indistinct print, colored or poor quality illustrations and photographs, print bleed-through, substandard margins, and improper alignment can adversely affect reproduction.

In the unlikely event that the author did not send a complete manuscript and there are missing pages, these will be noted. Also, if unauthorized copyright material had to be removed, a note will indicate the deletion.

**UMI<sup>®</sup>**

---

UMI Microform 3145077

Copyright 2004 by ProQuest Information and Learning Company.





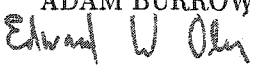
All rights reserved. This microform edition is protected against unauthorized copying under Title 17, United States Code.

ProQuest Information and Learning Company  
300 North Zeeb Road  
P.O. Box 1346  
Ann Arbor, MI 48106-1346

The University of Arizona ®  
Graduate College

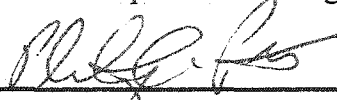
As members of the Final Examination Committee, we certify that we have read the  
dissertation prepared by AIMEE LOUISE HUNGERFORD  
entitled GAMMA-RAY LINES FROM ASYMMETRIC SUPERNOVAE

and recommend that it be accepted as fulfilling the dissertation requirement for the  
Degree of Doctor of Philosophy

 PHILIP PINTO	<u>9-13-04</u> date
 DAVID ARNETT	<u>9/10/04</u> date
 JILL BECHTOLD	<u>9/13/04</u> date
 ADAM BURROWS	date
 ED OLSZEWSKI	<u>9-13-04</u> date

Final approval and acceptance of this dissertation is contingent upon the candidate's submission of the final copies of the dissertation to the Graduate College.

I hereby certify that I have read this dissertation prepared under my direction and recommend that it be accepted as fulfilling the dissertation requirement.

 Dissertation Director: <u>PHILIP PINTO</u>	<u>9-13-04</u> date
---	------------------------

### STATEMENT BY AUTHOR

This dissertation has been submitted in partial fulfillment of requirements for an advanced degree at The University of Arizona and is deposited in the University Library to be made available to borrowers under rules of the Library.

Brief quotations from this dissertation are allowable without special permission, provided that accurate acknowledgment of source is made. Requests for permission for extended quotation from or reproduction of this manuscript in whole or in part may be granted by the head of the major department or the Dean of the Graduate College when in his or her judgment the proposed use of the material is in the interests of scholarship. In all other instances, however, permission must be obtained from the author.

SIGNED: \_\_\_\_\_

A handwritten signature in dark ink, appearing to be 'M. Q.', written over a horizontal line.

## ACKNOWLEDGEMENTS

Many thanks to my advisor Philip for being a great sounding board and morale booster; thank you in particular for letting me venture out from Arizona to find an army of advisors at UC-Santa Cruz and Los Alamos National Laboratory. A great many people helped out along the way: thanks to Tom and Todd for convincing me that code verification is the key to not losing sleep over unexpected results, and thanks to Peter for sheer perserverence in convincing me that code comparisons, however painful, are the ideal code verification. Thanks to Gabe for clever SDF utilities to ease the final months of analysis, and to Richard at Beomax for all my high-memory computing needs. Special computing mention also goes to the Space Simulator beowulf cluster in the Theoretical Astrophysics group at LANL, without which I would likely have retired as a grad student. This thesis research was performed under the auspices of the U.S. Department of Energy (DOE) by Los Alamos National Laboratory, under contract W-7405-ENG-36. Funding was also provided by DOE SciDAC grant number DE-FC02-01ER41176 and the National Science Foundation (CAREER grant AST 95-01634).

And finally thanks to Michelle, Audra and Chris. I attempt in this paragraph to thank these people to whom I am so indebted that no amount of saying thank you can begin to repay their efforts on my behalf. To Michelle, half of a thesis is the non-scientific details of staying enrolled, filling out grad college forms, fedexing proposals and just knowing how to check out the projector for talks. You've told me before that this is what you're here for, but the contagious smile and two-steps-ahead-of-me attitude with which you accomplish these tasks go above and beyond the call of duty. To Audra, for being there, regardless of where "there" ended up being. And to Chris, you are my most enthusiastic cheerleader and my most severe critic; I'm not sure how that works, but I am eternally grateful that it does. I am also grateful that Willy was right and you were wrong!

## DEDICATION

To my mom, for applauding my every accomplishment along the way...assuring me that no star was out of reach, and listening patiently as I explained why most stars are.

And to my dad...the existence of this thesis is one of a very few things that *can* be explained by the perihelion precession of Mercury in its elliptical orbit about the sun.

## TABLE OF CONTENTS

LIST OF TABLES . . . . .	8
LIST OF FIGURES . . . . .	9
ABSTRACT . . . . .	16
CHAPTER 1. INTRODUCTION . . . . .	17
1.0.1. Supernova 1987A . . . . .	19
1.1. The Cassiopeia A Supernova Remnant . . . . .	24
CHAPTER 2. CODE DEVELOPMENT AND VERIFICATION . . . . .	33
2.1. Monte Carlo Transport Technique . . . . .	33
2.1.1. Ejecta . . . . .	36
2.1.2. Photon Source . . . . .	40
2.1.3. Photon Interaction Processes . . . . .	46
2.2. Code Comparisons . . . . .	50
2.2.1. Overall Spectra . . . . .	52
2.2.2. Line Profiles . . . . .	56
2.2.3. Line Fluxes . . . . .	59
2.2.4. Summary of Comparisons . . . . .	64
CHAPTER 3. GAMMA-RAY LINE EMISSION FROM BIPOLAR SUPERNOVAE . . . . .	69
3.1. Explosion Simulations . . . . .	70
3.1.1. Numerical Schemes . . . . .	71
3.1.2. Explosion and Nickel Distribution . . . . .	74
3.2. High Energy Spectral Calculations . . . . .	83
3.2.1. Numerical Schemes . . . . .	83
3.2.2. Hard X-ray and Gamma-ray Spectrum . . . . .	85
3.2.3. Gamma-ray Line Profiles . . . . .	87
3.3. Summary . . . . .	92
CHAPTER 4. GAMMA-RAY LINE EMISSION FROM UNIPOLAR SUPERNOVAE . . . . .	95
4.1. Explosion Simulations . . . . .	98
4.1.1. Numerical Schemes . . . . .	98
4.1.2. Explosion and Nickel Distribution . . . . .	101
4.2. High Energy Spectral Calculations . . . . .	113

TABLE OF CONTENTS—*Continued*

4.2.1. Numerical Schemes . . . . .	113
4.2.2. Hard X-ray and Gamma-ray Spectrum . . . . .	114
4.2.3. Gamma-ray Line Profiles . . . . .	116
4.2.4. Summary . . . . .	120
CHAPTER 5. SUMMARY . . . . .	123
APPENDIX . . . . .	129
REFERENCES . . . . .	136



## LIST OF TABLES

TABLE 2.1. Characteristics of Transport Codes in Comparison . . . . .	37
TABLE 2.2. Important Gamma-ray Lines for $^{56}\text{Ni}$ and $^{56}\text{Co}$ Decays. Lines studied in this work are listed in bold font. All ratios are from the 8th Table of Isotopes (1996). . . . .	41
TABLE 2.3. Characteristics of SN Ia Explosion Models . . . . .	51
TABLE 3.1. Explosion simulation parameters. . . . .	72
TABLE 5.1. Line and continuum fluxes for the four models investigated in this thesis at various epochs. . . . .	127
TABLE 5.2. Lifetimes for the radioactive isotopes included in Maverick. . . .	130

## LIST OF FIGURES

FIGURE 1.1. High energy spectrum from FASTGAM simulation using progenitor model 10H. (from Pinto & Woosley 1988a, reproduced by permission of the AAS) . . . . .	20
FIGURE 1.2. Line profile for [FeII] 18 $\mu\text{m}$ and 1.26 $\mu\text{m}$ lines from SN 1987A. Both lines exhibit a redshift of roughly 500 km/s relative to the systemic velocity of the LMC (280 km/s). (from Spyromilio, Meikle & Allen 1990)	22
FIGURE 1.3. Line profile for the $^{56}\text{Co}$ 847 keV line from SN 1987A. Like the IR lines, this too exhibits a redshift of roughly 500 km/s relative to the systemic velocity of the LMC (280 km/s). (from Tueller et al. 1990, reproduced by permission of the AAS) . . . . .	23
FIGURE 1.4. Million-second Chandra/ACIS X-ray image of Cas A in 3 energy bands. (from Hwang et al. 2004, reproduced by permission of the AAS)	26
FIGURE 1.5. Chandra/ACIS X-ray image of Cas A depicting the ratio of Si XII to magnesium and iron emission. A well-collimated jet structure is clearly seen. (from Hwang et al. 2004, reproduced by permission of the AAS) .	27
FIGURE 1.6. $^{44}\text{Ti}$ yields from Type II supernovae. (from Timmes et al. 1996, reproduced by permission of the AAS) . . . . .	28
FIGURE 1.7. $^{44}\text{Ti}$ yields from Type Ib supernovae. (from Timmes et al. 1996, reproduced by permission of the AAS) . . . . .	29
FIGURE 2.1. Line shifting due to the expansion of the ejecta of four SN models. The fractional line shift due to the expansion of the ejecta is plotted on the left axis, the shift for the 847 keV line is shown on the right. For reference, $^{56}\text{Ni}$ -rich regions of the ejecta are shown in the upper left as thick, horizontal bars. Note $^{56}\text{Ni}$ at the surface of models W7DT and HED6. . . . .	39
FIGURE 2.2. Photon cross sections for the 3 primary opacity sources to $\gamma$ -rays: Photo-electric absorption, Compton Scattering, and Pair production. Y-axis is the fraction of the total cross section made up by each process in log space. Pair production and Photoelectric opacities are taken from the LLNL Evaluated Nuclear Data Library (Plechaty, Cullen & Howerton 1981). Compton cross section values are taken from Equation 2.4 (Raeside 1976). . . . .	47
FIGURE 2.3. A sequence of spectra for the SN Ia model, DD202C. The spectra, at 15 $^d$ , 25 $^d$ , and 50 $^d$ , show the level of agreement between simulations for both the line and continuum emission. Comparisons between the two codes that do not treat line broadening/shifting (The & Kumagai) and the others that do, show the early effects of blue-shifting. . . . .	53

LIST OF FIGURES—*Continued*

- FIGURE 2.4. A sequence of spectra for the SN Ia model, W7. The absence of nickel near the surface of W7 leads to the inhibition of line emission until later times. As with DD202C, the spectra, at  $15^d$ ,  $25^d$ , and  $50^d$ , show a high level of agreement between simulations for both the line and continuum emission. . . . . 54
- FIGURE 2.5. A sequence of spectra for the SN Ia model, HED6. The spectra, at  $15^d$ ,  $25^d$ , and  $50^d$ , show a high level of agreement between simulations, in this case for a low-mass model that features early escape of  $\gamma$ -ray emission. . . . . 55
- FIGURE 2.6. Line profiles of the 1238 keV line for the SN Ia models, DD202C, W7, HED6. Although the simulations show noticeable variations, the differences between the Chandrasekhar-mass models (DD202C & W7) and the sub-Chandrasekhar-mass model (HED6) greatly exceeds the variations between simulations. Differentiating between DD202C & W7 is more difficult, but is not rendered impossible by the variations between simulations if a sequence of spectra were available for comparison. . . . . 57
- FIGURE 2.7. Line profiles of the 812 & 847 keV line complex for the SN Ia models, DD202C, W7, HED6. The interpretation is similar to that of the 1238 keV line: the differences between the Chandrasekhar-mass models (DD202C & W7) and the sub-Chandrasekhar-mass model (HED6) greatly exceeds the variations between simulations, and while differentiating between DD202C & W7 is more difficult, it is not rendered impossible by the variations between simulations if a sequence of spectra were available for comparison. . . . . 58
- FIGURE 2.8. Line fluxes of the 1238 keV line for the SN models, DD202C and W7. The line fluxes extracted from the spectra (Höflich, Maverick, Fastgam, Isern) agree with the line fluxes that result from tagging line photons (The, Boggs, Kumagai). All current simulations predict fainter light curves than shown in previous published results (HWK98 for DD202C & HED6; Kumagai & Nomoto 1997 for W7). Spectral extraction assumed a 1150 - 1300 keV bandwidth. The HWK98 results are shown with and without the scaling for the escape fraction and branching ratios. Although the line definition in HWK98 differs from that used in this work, the light curves are similar when the corrections are applied. . . . . 61
- FIGURE 2.9. Line fluxes of the 1238 keV line as in the previous figure, for model HED6. . . . . 62

LIST OF FIGURES—*Continued*

- FIGURE 2.10. Line fluxes of the 847 keV line for the SN models DD202C and W7. Spectral extraction was more complicated for the 847 keV line than for the 1238 keV line (requiring the assumption that the 847 & 812 escape fractions are equal, and that all emission in the 790 - 900 keV energy band is line emission), but the light curves agree well with the light curves that result from tagging photons. Again, all current simulations suggest less line emission than suggested in HWK98 and Kumagai & Nomoto 1997. Also, the scaling for escape fraction and branching ratios brings the HWK98 light curves into rough agreement with the other light curves. 63
- FIGURE 2.11. Line fluxes of the 847 keV line for the SN models as in the previous figure, for model HED6. . . . . 64
- FIGURE 2.12. Line fluxes of the 812 keV line for the SN models DD202C and W7. As with the 812 keV line emission, the spectral extraction and tagging light curves agree, and are fainter than the HWK98 and Kumagai & Nomoto 1997 light curves. With the scaling for escape fraction and branching ratios, the HWK98 light curves agree fairly well with the other light curves. The HWK98 light curves after 20-30 days fall to zero, faster than the other light curves; this is due to the different definition for the 812 keV line employed in that work. . . . . 65
- FIGURE 2.13. Line fluxes of the 812 keV line as in the previous figure, for model HED6. . . . . 66
- FIGURE 3.1. Velocity distribution of nickel (solid), Oxygen (dotted), Helium (dashed), and Hydrogen (long dashed) in our 3-dimensional simulations. Comparing these distributions to the 2-dimensional simulations in Fig. 1 of Herant & Woosley (1994), we note that the distribution of elements is similar in both the 2- and 3-dimensional simulations. However, the stronger 3-dimensional explosion causes all of the ejecta to be moving slightly faster than that of the 2-dimensional simulation and it is difficult to compare mixing instabilities. . . . . 74
- FIGURE 3.2. Density contour ( $7 \times 10^{-5} \text{ g cm}^{-3}$ ) plot of the early stages of the convection, 4.3 hours after the launch of the explosion. Notice that tendrils mixing out the material have already developed. It is this mixing that places nickel far beyond its initial distribution. . . . . 76
- FIGURE 3.3. 3-dimensional simulation of the symmetric explosion 1 year after the shock launch. The contours represent the cobalt distribution with a number density of  $10^{-5}$ . The colors denote the density distribution. Note that although the explosion is symmetric, Rayleigh-Taylor instabilities mix out the nickel. . . . . 77

LIST OF FIGURES—*Continued*

- FIGURE 3.4. Distribution of the nickel ejecta in mass, comparing jet explosions with a symmetric explosion (top panel) and equatorial explosions with a symmetric explosion (bottom panel). Note that as we increase the degree of asymmetry (Jet4 versus Jet2, Equator4 versus Equator2), the mixing increases dramatically, placing nickel well into the hydrogen envelope of the star. The dashed line (top panel) shows the extent of mixing if all of the nickel/cobalt decay energy is deposited into the nickel ejecta and produces almost as much mixing in a symmetric explosion as the Jet2 model. . . . . 78
- FIGURE 3.5. 3-dimensional simulation of the Jet2 asymmetric explosion 1 year after shock launch. As in Fig. 3, the contours represent the cobalt distribution with a number density of  $10^{-5}$ . The colors denote the density distribution. The nickel is mixed out extensively in the polar direction where the explosion was strongest. However, the density distribution did not gain large asymmetries and remained fairly symmetric. . . . . 80
- FIGURE 3.6. Distribution of the nickel ejecta versus velocity comparing jet explosions with a symmetric explosion (top panel) and equatorial explosions with a symmetric explosion (bottom panel). Note that as we increase the degree of asymmetry (Jet4 versus Jet2, Equator4 versus Equator2), the mixing increases dramatically, producing nickel velocities in excess of 3000 km/s. The dashed line (top panel) shows the velocities achieved if all of the nickel/cobalt decay energy is deposited into the nickel ejecta and produces almost as much mixing in a symmetric explosion as the Jet2 model. . . . . 81
- FIGURE 3.7. Fraction of nickel ejecta mixed out into the star for our set of simulations. Note that for mild asymmetries (Jet2) or if decay energy is included in a symmetric explosion (Symmetric+Decay), nearly 10% of the nickel mass is injected into the hydrogen envelope. If this amount of mixing occurs in weak explosions, an explosion that resulted in a  $4.5 M_{\odot}$  black hole remnant would still eject a moderate amount of nickel. . . . . 82
- FIGURE 3.8. Total hard X- and  $\gamma$ -ray spectrum at 5 different times during the explosion (150,200,250,300,365 days) for symmetric (solid lines) and aspherical (Jet2) explosions (dotted and dashed lines). The flux is determined by assuming the object is 60 kpc from the observer. The dotted lines refer to an aspherical explosion where the jet is directed along the line of sight of the observer. The dashed lines refer to an explosion where the observer line of sight is directed  $90^{\circ}$  off of the jet axis, in the equatorial direction. Regardless of observer viewing angle, the aspherical explosion is brighter than the Symmetric explosion. . . . . 86

LIST OF FIGURES—*Continued*

- FIGURE 3.9. Contour plots in the  $xz$ -plane of the Symmetric and Jet2 explosion models at  $t = 150$  days. Inner contour is for  $^{56}\text{Co}$  number density which traces the surface of the  $\gamma$ -ray emitting region. Outer contour is for the mass density which follows electron density and thus traces the dominant opacity source (Compton scattering). The lines represent lines-of-sight through the ejecta for which the optical depth from emission region to ejecta surface has been calculated. Regardless of viewing angle, the optical depth of the  $^{56}\text{Co}$  ejected along the poles in the Jet2 explosion remains quite low. Hence, it is this material that dominates the observed emission for all viewing angles in the aspherical explosion. . . . . 88
- FIGURE 3.10. Line profiles of the  $^{56}\text{Co}$  1.238 and 0.847 MeV lines for the Symmetric model at 4 different times during the explosion (200, 250, 300, 365 days). 3 different viewing angles are shown: polar view (dotted lines), equatorial view (dashed lines) and an intermediate view angle of  $\sim 45^\circ$  (dash-dot lines). The line profiles do not show significant variation with viewing angle (as would be expected for a symmetric explosion.) . . . . 90
- FIGURE 3.11. Line profiles of the  $^{56}\text{Co}$  1.238 and 0.847 MeV lines for the Jet2 model at 4 different times during the explosion (200, 250, 300, 365 days). 3 different viewing angles are shown: polar view (dotted lines), equatorial view (dashed lines) and an intermediate view angle of  $\sim 45^\circ$  (dash-dot lines). The flux axis is scaled by a factor of 4 over the Symmetric model profiles shown in Figure 11. Significant variations in the line profiles with viewing angle are apparent, and can be explained by considering the velocity distribution (and thus radial distribution in a homologous expansion) of the ejecta responsible for the observed emission. . . . . 91
- FIGURE 4.1. Image of the Guitar Nebula from the Hale Telescope at Palomar Observatory. (Chatterjee & Cordes 2002, reproduced by permission of the AAS) . . . . . 96
- FIGURE 4.2. Pulsar velocity distribution (bold line in top panel) taken from Arzoumanian et al. 2002. (reproduced by permission of the AAS) . . . . 97
- FIGURE 4.3. Plot of radial velocity versus polar angle for the 2D rotating collapse model of Fryer & Heger (2000). Overplotted are a cosine function and top-hat function which represent the two assumed profiles for the artificial velocity asymmetries imposed in this work. Note that the model profile lies somewhere between these two extremes. . . . . 100

LIST OF FIGURES—*Continued*

- FIGURE 4.4. 3-dimensional rendering of the f3th40 explosion model 1 year after the shock launch. The isosurface represents the cobalt distribution with a number density of  $10^{-5}$ . The colors denote the density distribution. The top-hat distribution of the imposed velocity asymmetry allows a significant portion of the cone material to expand without drag from fluid shear forces, resulting in the large splash of material at the outer ejecta. . . . . 102
- FIGURE 4.5. Same as previous figure, but for model f2th20. Again we see the splash of cobalt in the outer ejecta, though not as extreme due to the smaller angle and lower contrast of the velocity asymmetry. . . . . 103
- FIGURE 4.6. Plot of mass in a cone of radius  $9^\circ$  along a direction in polar angle for the f3th40 model. Error bars reflect the cone diameter. Blue line is for the initial time at  $t = 100$  s and red line is for  $t = 450$  days (long after flow has become homologous.) Matter is being funneled into the faster expanding, lower density region in the cone. This results in an enhancement of the mass for polar angles near zero, and a reduction in mass for angles just outside of this. . . . . 106
- FIGURE 4.7. Similar to the previous figure, but for model f2th20 at  $t = 150$  d. The ejecta have already reached the phase of homologous expansion, so can be directly compared with the f3th40 results. . . . . 107
- FIGURE 4.8. Similar to the previous figures, but showing kinetic energy as a function of polar angle for the f3th40 model. Blue line is for the initial time at  $t = 100$  s and red line is for  $t = 450$  days (long after flow has become homologous.) It is clear that the explosion is spherizing (i.e. energy in the enhanced explosion lobe is smearing and being shared with the rest of the ejecta.) Note from the previous figures that the mass in the cone actually increases at later times, suggesting that the velocity structure is even more spherical than the energy distribution shown here. Still, after having the shock pass through the entire star, there does still remain some asymmetry in contrast to the complete spherization of the bipolar explosion models. . . . . 108
- FIGURE 4.9. Similar to the previous figure, but for model f2th20 at  $t = 150$  d. The ejecta have already reached the phase of homologous expansion, so can be directly compared with the f3th40 results. . . . . 109

LIST OF FIGURES—*Continued*

- FIGURE 4.10. Mass of 56-weight elements (e.g. initial  $^{56}\text{Ni}$  mass) versus line of sight velocity for a number of viewing angles at  $t = 365$  days. Central panel on the left shows a contour plot of density (blue) and cobalt number density (red). Due to the homologous nature of the expansion, these distributions represent the line shapes one would expect from nickel, cobalt or iron emission in the absence of significant ionization or opacity effects. 110
- FIGURE 4.11. Same as previous figure, but for model f2th20. . . . . 111
- FIGURE 4.12. Mass of 56-weight elements (e.g. initial  $^{56}\text{Ni}$  mass) as a function of line of sight velocity for the Jet2 (polar view) and Symmetric explosion models of Chapter 3. Note the broader line profile for the Jet2, and even the Symmetric model, as compared to either of the unipolar explosion models. Also note the absence of higher velocity structure as compared to the unipolar models. . . . . 112
- FIGURE 4.13. Logarithmic plot of total hard X- and  $\gamma$ -ray spectrum at  $t = 365$  d for model f3th40. The flux was calculated assuming a distance of 60 kpc. The different colored lines refer to different viewing angles through the ejecta. Theta = 0 viewing angle is looking down the explosion lobe (positive z-axis) and Theta = 90 is perpendicular (looking down the positive x-axis). Theta = 0 direction shows a higher energy turnover indicating a larger abundance of heavy elements mixed to the outer ejecta. . . . . 114
- FIGURE 4.14. Same as previous figure, but for model f2th20. . . . . 115
- FIGURE 4.15. Line profiles of the  $^{56}\text{Co}$  847 keV decay line for model f3th40 at  $t = 365$  days. Central panel on the left shows a contour plot of density (blue) and cobalt number density (red). Surrounding panels represent line profiles for the set of viewing angles depicted by the black vectors overplotted on the density contours. The emission in the line profiles arises predominantly from the cobalt ejected along the enhanced explosion lobe. Due to the homologous nature of the ejecta, the structure in the lines can be understood by summing this extended cobalt material along lines perpendicular to the viewing angle vectors. See text for a more in depth discussion. . . . . 117
- FIGURE 4.16. Same as previous figure, but for model f2th20. . . . . 118



## ABSTRACT

High energy emission from supernovae provide a direct window into the quantity and distribution of radioactive elements produced in these explosions. Combining supernova explosion calculations with 3D Monte Carlo  $\gamma$ -ray transport, I have studied the effect mixing and asymmetries have on the hard X-ray and  $\gamma$ -ray spectra. Two types of asymmetries (bipolar and unipolar) are investigated, the parameters of which are motivated by the most recent findings from multi-dimensional core-collapse supernova simulations. These bipolar and unipolar asymmetries are imposed artificially on 1-dimensional stellar progenitor structures and their evolution is followed using a 3-dimensional smoothed particle hydrodynamics (SPH) code. Global asymmetries in the explosion enhance the outward mixing of heavy elements such as  $^{56}\text{Ni}$ , reducing the observable emergence time for the hard X-ray continuum and  $\gamma$ -ray line emission over that of symmetrically mixed models. The details of the velocity asymmetry lead to very different nickel distributions in the outer envelope. The high energy spectra resulting from these models predict an angular variation for the correspondence between the emergence time of the hard X-ray continuum and the broadening of the  $\gamma$ -line profiles. The unipolar explosion models, in particular, demonstrate that redshifted  $\gamma$ -ray line profiles are attainable at epochs where  $\gamma$ -ray emission arises predominantly from the the outer extent of the nickel distribution. The departure from a symmetric explosion scenario manifests itself most clearly in the extended nickel, making  $\gamma$ -ray line observations an ideal probe of the initial explosion asymmetry.

## Chapter 1

### INTRODUCTION

Core-collapse supernovae (SNe) are among the most energetic explosions in the universe. They mark the catastrophic end of stars more massive than  $8 M_{\odot}$  and leave behind compact remnants such as neutron stars and stellar mass blackholes. The nucleosynthesis in these massive stars, and in their subsequent explosion, is responsible for most of the heavy element enrichment in the modern universe. Naturally, any attempt to address human origins must begin with an understanding of core-collapse supernovae.

Among the heavy nuclei synthesized during explosive burning are a set of unstable isotopes such as  $^{56}\text{Ni}$  and  $^{44}\text{Ti}$  which emit  $\gamma$ -radiation when they decay. Much of this radiation is absorbed within the supernova and reprocessed, to emerge as a supernova's magnificent light show, visible across the universe. The decay of  $^{56}\text{Ni}$  through  $^{56}\text{Co}$  to  $^{56}\text{Fe}$  is the main source of iron.

Although the deposited  $\gamma$ -radiation is important to the optical display, some of the  $\gamma$ -rays penetrate the supernova ejecta to emerge with little or no interaction. Although a small fraction of the total emergent energy, the  $\gamma$ -rays which escape provide the most direct diagnostic of the underlying physics in the explosion itself. Compared with light at other wavelengths, the processes by which MeV  $\gamma$ -radiation is produced and subsequently interacts with the supernova on its way to the surface are relatively simple.

$\gamma$ -ray lines are emitted through the radiative relaxation of excited nuclear states in gas which is far colder than typical nuclear energies. This means that the emission rate is determined simply by the number of nuclei originally produced and the time elapsed since production. Their emission is thus uniquely insensitive to thermody-

namic conditions in the supernova's ejecta (with one possible exception, described below).

The dominant interaction affecting these energetic photons on their way out of a supernova is Compton scattering off electrons. The opacities which characterize the optical, infrared, and X-ray bands are complex and depend sensitively upon the temperature, density, and excitation state of the gas. The Compton opacity varies smoothly and slowly with photon energy, with no resonant features, in a well-known manner. To an MeV photon, the relatively low binding energies of atomic states (less than a few keV for all elements of any abundance) have little effect. This means that the dominant interaction for  $\gamma$ -rays is only weakly dependent on composition; it is affected only by the total number of electrons, bound or free, per unit mass, measured by the electron fraction  $Y_e$ . The  $\gamma$ -rays which emerge from a supernova are thus diminished in intensity simply by the total amount of material along the line of sight, with little effect from the intervening material's density or temperature.

Because each radioactive nucleus emits a distinct spectrum of relatively few strong lines,  $\gamma$ -rays provide abundance information about specific isotopes of an element. The Compton cross section is much smaller than those affecting lower-energy photons, allowing some  $\gamma$ -rays to escape directly from regions deep within the explosion; hard X- and  $\gamma$ -ray spectra from core-collapse events thus present a relatively unprocessed view of the underlying structure of the abundances and dynamics of a supernova's nucleosynthetic yield.

The mean lifetimes of the potentially observable radioactive isotopes span a range of values and thus probe supernova evolution over a variety of timescales. This range can be divided into three categories. The short-lived isotopes ( $^{56}\text{Ni}$ ,  $^{56}\text{Co}$ ) have mean lifetimes of order a year or less. The next range contains isotopes ( $^{44}\text{Ti}$ ) with lifetimes of order 100 years, and the long-lived isotopes ( $^{26}\text{Al}$ ,  $^{60}\text{Fe}$ ) have lifetimes of order  $10^6$  years. The average time between supernova events in our galaxy is  $\sim 50$  years (for a supernova rate of  $\sim 2 \text{ century}^{-1}$ ). This implies that decay emission from

isotopes in the first two categories will be observed on timescales consistent with a single supernova. In contrast, emission from the long-lived isotopes is contributed by thousands of supernova events spanning the million-year lifetime of the isotope. The information conveyed by these observations is a statistical average over an entire population of core-collapse events.

The theoretical work presented here involves numerical simulations of an individual supernova explosion, concentrating on the short- and intermediate-lived radioactive isotopes and the insight they provide for the early explosion and extended remnant phases of supernovae. In particular, I concentrate on interpreting  $\gamma$ -ray observations of SN 1987A, the hallmark example of what can be learned from short-lived radioisotopic observations, and the supernova remnant (SNR) Cassiopeia A, which highlights the power of intermediate-lived isotopes to probe the details of the explosion mechanism even centuries after the explosion itself.

### 1.0.1 Supernova 1987A

Supernova 1987A marked the spectacular death of the massive star Sanduleak -69° 202 (see reviews by Arnett et al. 1989, McCray et al. 1993). The proximity of this supernova (located at  $\sim 60$  kpc distance in the Large Magellanic Cloud) allowed for the first direct detection of nuclear decay lines from a supernova explosion. As early as 1957 (Burbidge, Burbidge, Fowler & Hoyle), it was believed that radioactive decay from unstable elements from explosive nucleosynthesis was primarily responsible for powering the lightcurves of supernovae. By the late sixties, work had zeroed in on the responsible isotope,  $^{56}\text{Ni}$  and its decay products  $^{56}\text{Co}$  and  $^{56}\text{Fe}$  (Colgate & McKee 1969; Clayton, Colgate & Fishman 1969). The detection of the  $^{56}\text{Co}$  847 and 1238 keV decay lines from SN 1987A was the first and dramatic validation of that prediction. (Matz et al. 1988, Cook et al. 1988, Mahoney et al. 1988, Rester et al. 1989, Teegarden et al. 1989, Tueller et al. 1990, Kazaryan et al. 1990, Ait-Ouamer et al.

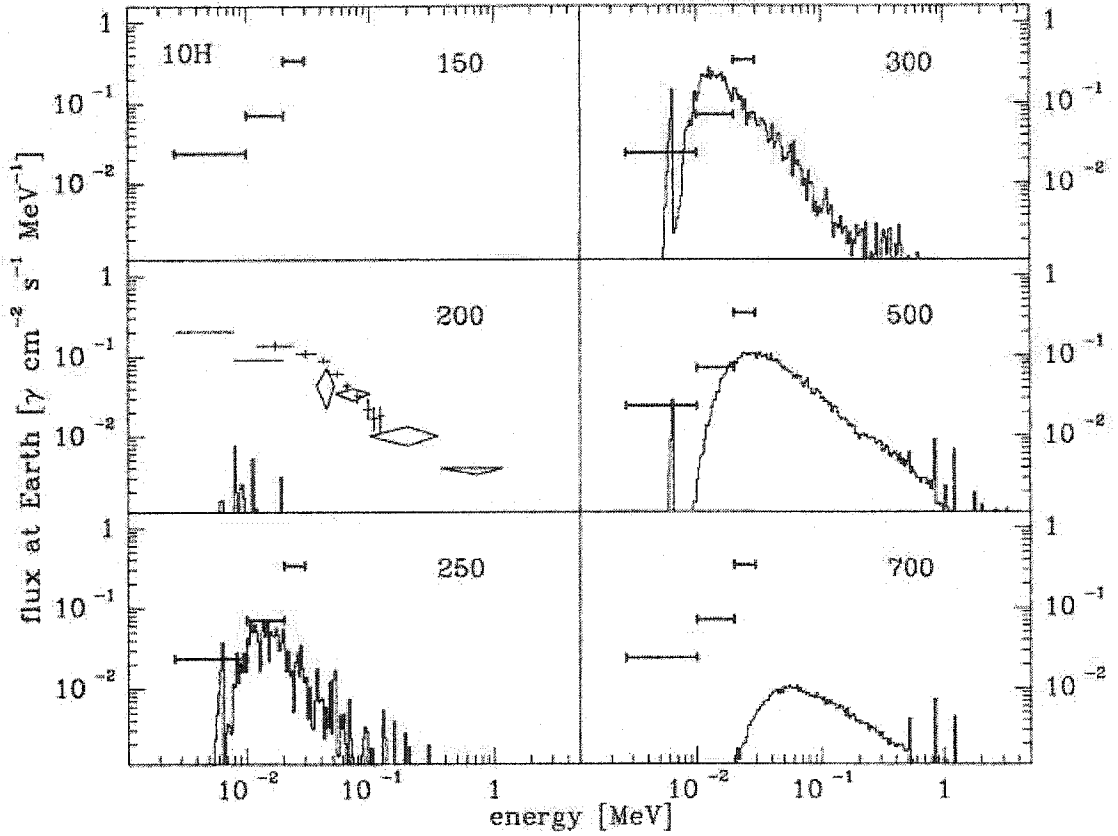


FIGURE 1.1. High energy spectrum from FASTGAM simulation using progenitor model 10H. (from Pinto & Woosley 1988a, reproduced by permission of the AAS)

1990)

The detection of hard X-ray and  $\gamma$ -line emission from SN 1987A came in nearly 6 months earlier than theorists had predicted, however. (McCray, Shull & Sutherland 1987; Gehrels, MacCallum & Leventhall 1987; Itoh et al. 1987; Grebenev & Sunyaev 1987); Woosley, Pinto & Ensman 1988; Xu et al. 1988). These predictions were based on simulations using then-current spherically symmetric explosion models. Figure 1.1 (Pinto & Woosley 1988a) shows an example of the simulated high energy spectra at different times expected from explosion model 10H from Woosley (1988).

One should note three key features of this result (solid lines). Lines from  $^{56}\text{Ni}$  and  $^{56}\text{Co}$  decay can be seen as the forest of lines around 1 MeV. These are the photons

which directly escape the supernova, i.e. without interaction in the ejecta. Below them in energy, there is a power-law continuum. This arises from photons which have scattered a few times on their way to escape. An MeV photon loses roughly half its energy per scattering; the precise amount depends upon the initial photon energy and the angle through which the photon is scattered. Thus, near 500 keV the spectrum is dominated by once-scattered photons, near 250 keV it is dominated by twice-scattered photons, and so on. There is less continuum flux at higher energies simply because there is less chance of a photon traveling the distance to the surface in a smaller number of scatterings (leaving the photon at a higher energy) than in a larger number (reducing the photon's energy to a greater extent).

The third feature is the abrupt fall-off of flux at energies around 20 keV. Once the  $\gamma$ -rays have down-scattered to this energy, the photoelectric opacity becomes greater than the Compton opacity, and the photons are absorbed, to emerge as thermalized radiation, primarily in the optical and infrared.<sup>1</sup>

Also pictured in Figure 1.1 are the hard X-ray observations from the HEXE (crosses) and PULSAR X-1 (diamonds) instruments on board the MIR spacecraft (Sunyaev et al. 1987). It is clear from the figure that theoretical predictions of the hard X-ray flux for model 10H (a favored progenitor model from early light curve constraints alone), fell significantly short of the actual hard X-ray observations (Dotani et al. 1987, Sunyaev et al 1987). This was a puzzle. As the supernova shock proceeds outward through the star, the shock energy is distributed over an increasingly larger volume, and the temperature of the post-shock gas decreases. Radioactive nickel is produced in explosive burning only at very high temperatures, and these tempera-

---

<sup>1</sup>The turnover in the Comptonized power-law spectrum could also, in principle, be attributed to insufficient Comptonization (i.e. the optical depth to high energy photons is sufficiently low that photons do not scatter enough times to populate the lower energy portion of the spectrum.) A spectral turnover arising from this effect should move to higher and higher energies as the optical depth decreases with supernova expansion. The turnover for SN 1987A's hard X-ray spectrum was relatively constant with time, providing evidence that photoelectric absorption was the process responsible for its turnover.

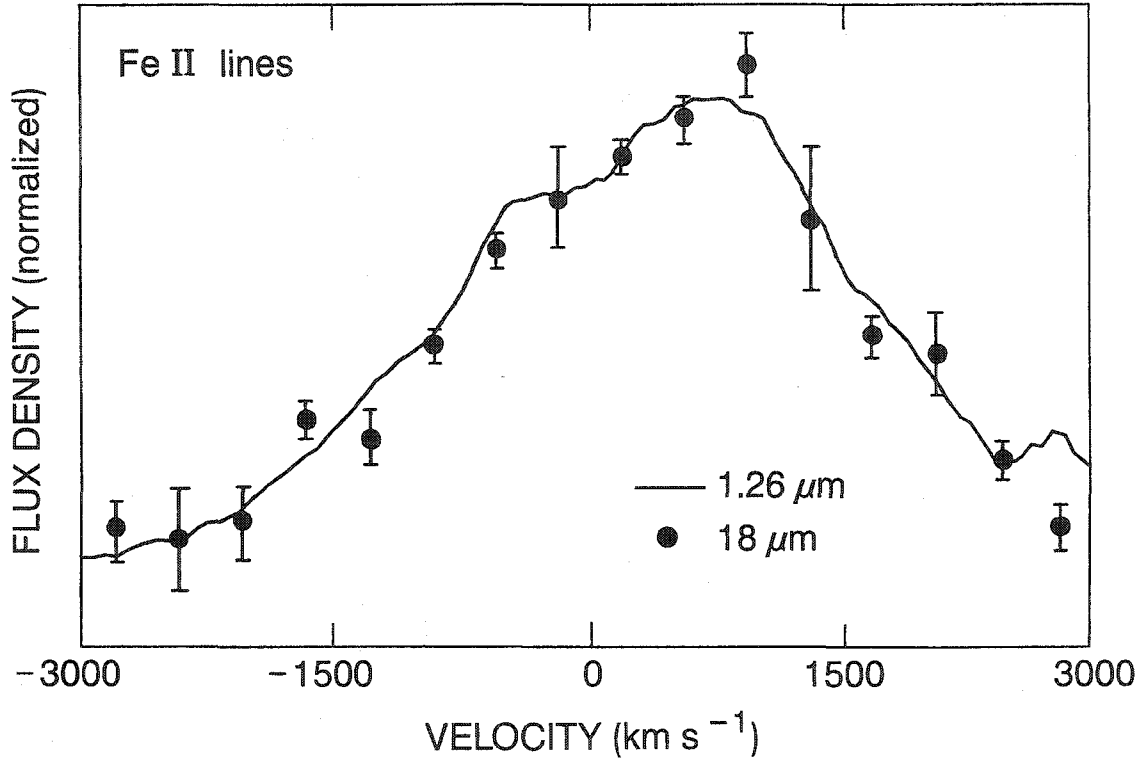


FIGURE 1.2. Line profile for [FeII] 18  $\mu\text{m}$  and 1.26  $\mu\text{m}$  lines from SN 1987A. Both lines exhibit a redshift of roughly 500 km/s relative to the systemic velocity of the LMC (280 km/s). (from Spyromilio, Meikle & Allen 1990)

tures could only be produced at small radii, deep within the ejecta. Optical depths to these deep regions would remain large enough to prevent escape for more than a year. The most straightforward explanation for this discrepancy was that radioactive nickel was somehow brought closer to the surface after it was produced; the stratification caused by the steady decrease in the peak temperature attained by material at larger radii had been mixed up. (Ebisuzaki & Shibazaki 1988; Leising 1988; Kumagai et al. 1988; Pinto & Woosley 1988a, Pinto & Woosley 1988b; The, Burrows & Bussard 1990; Sunyaev et al. 1990). With this assumption, the optical depth to the surface from at least some radioactive material was reduced, the  $\gamma$ -rays could escape more freely, and better fits to the high energy observations were obtained.

The early emergence of hard X- and  $\gamma$ -rays was not the only indication that a break

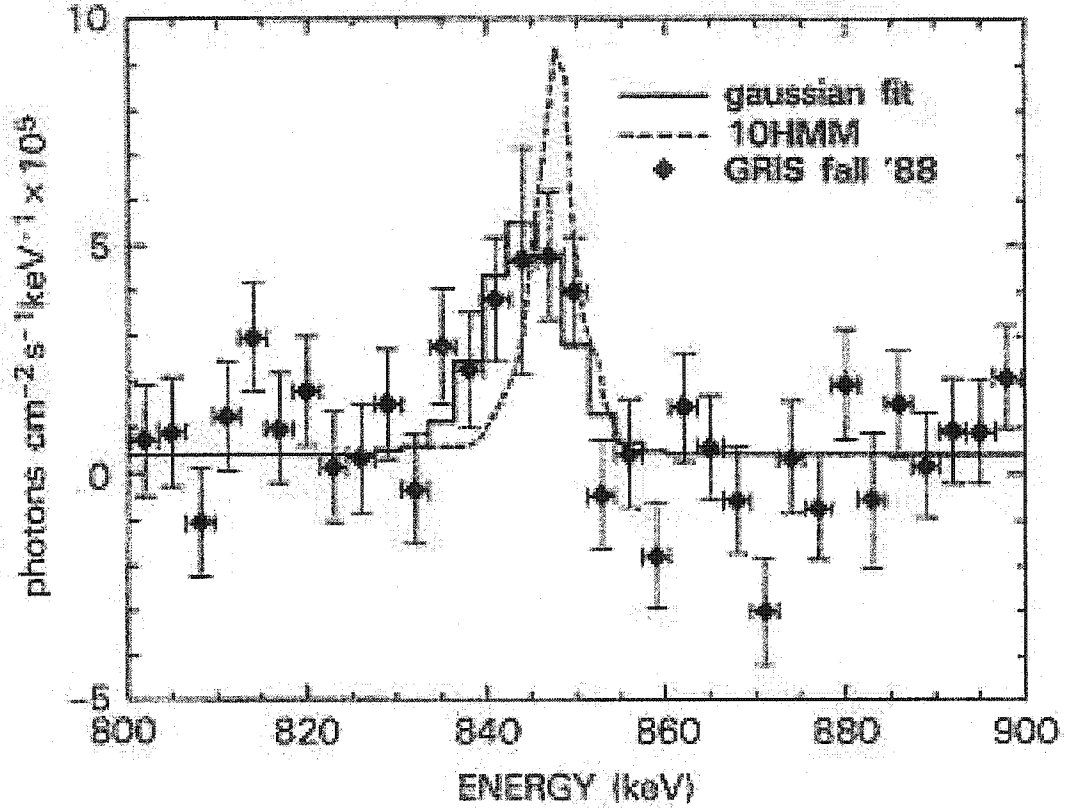


FIGURE 1.3. Line profile for the  $^{56}\text{Co}$  847 keV line from SN 1987A. Like the IR lines, this too exhibits a redshift of roughly 500 km/s relative to the systemic velocity of the LMC (280 km/s). (from Tueller et al. 1990, reproduced by permission of the AAS)

in spherical symmetry was needed for the explosion phase. The lightcurves predicted from unmixed models showed an abrupt brightening when radioactive energy first diffused to the surface. The energy left behind by the shock's passage through the supernova accounts for the early lightcurve. After some time, energy from  $^{56}\text{Ni}$  decay diffuses to the surface and adds its energy to the lightcurve. Because all of the nickel was concentrated at the center of the explosion, at nearly the same distance from the surface, this energy arrived all at once. By mixing the ejecta, the range in diffusion time could be extended and the transition from shock power to radioactivity power could be smoothed out, better matching the observations (Arnett et al. 1989).



Furthermore, H- $\alpha$  and He I (1.083  $\mu\text{m}$ ) observations showed a bump of emission at a high redshifted velocity (the so-called “Bochum event”), which was most readily explained by the presence of a clump of  $^{56}\text{Ni}$  located near the edge on the far side of the supernova ejecta (Chugai 1991; Utrobin et al. 1995), providing further evidence of asymmetry.

While lightcurve timing and optical line profiles might be considered somewhat indirect evidence,  $\gamma$ -ray line profiles from  $^{56}\text{Co}$  decay emission, as well as infrared (IR) [Fe II], [Co II] and [Ar II] line emission, were broadened to velocities of order 3500 km/s (Spyromilio, Meikle & Allen 1990, Haas 1990, Witteborn et al. 1989). This provided a more direct implication that heavy elements such as cobalt and iron, both daughter products of  $^{56}\text{Ni}$  decay, had managed to mix all the way into the hydrogen envelope of the supernova ejecta.

Finally, as seen in Figures 1.2 and 1.3, both the  $\gamma$ -ray lines and [FeII] IR lines showed a redshift of order 500 km/s with respect to lines arising in the progenitor’s stellar wind. As first studied by Grant & Dean (1993), this argues for the presence of a global asymmetry with the center of mass of the  $^{56}\text{Ni}$  located predominantly in an off-center distribution. Observations of SN 1987A at other wavelengths also seemed to require some degree of global asymmetry, so the question arises: is SN 1987A unusual in this respect? No other recent SN event exists with the kind of observational detail against which to compare SN 1987A, so we must turn to observations of older nearby explosions, supernova remnants (SNR) in our attempt to answer this question.

### 1.1 The Cassiopeia A Supernova Remnant

It is widely accepted that Cassiopeia A (Cas A) is the expanding remnant of a core-collapse supernova, possibly observed by J. Flamsteed in 1680 A.D (Ashworth 1980). With an age of roughly 325 years and a distance of  $\sim 3.4$  kpc (Reed et al. 1995), it is the youngest and one of the nearest supernova remnants in the galaxy. This has made

it a primary target for remnant studies at a variety of wavelengths, including X- and  $\gamma$ -rays. Indeed, the first-light target chosen for the Chandra X-ray Observatory was a 5000 s observation towards Cas A. The resulting image provides us with the answer we seek by revealing further evidence for a break with the spherically-symmetric paradigm of stellar explosions, just as the  $\gamma$ -ray observations of SN 1987A had required. Figure 1.4 shows the false color composite image of Cas A from the recent mega-second Chandra/ACIS observations (Hwang et al. 2004). In it, images in energy bands have been combined; the flux in each band is dominated by line emission from a different set of elements. Of particular importance in this image is the spatial distribution of blue regions (dominated by line emission from Fe-rich material) relative to red regions (Si-rich material). Presumably the progenitor star synthesized the Fe-rich material in its deepest layers, below the Si-rich ashes of explosive burning in the progenitor's oxygen shell. As Figure 1.4 demonstrates, the blue, Fe-rich material is located *outside* the Si-rich material, suggesting the same sort of mixing overturn in the layered structure that was invoked to explain the high energy emission from SN 1987A. In figure 1.5 we see the ratio of Si XII emission to nearby iron emission. A well-collimated jet of silicon is clearly seen, and the high-velocity iron is again seen as dark areas outside the silicon, especially around the jet.

As with SN 1987A, Cas A was a first for  $\gamma$ -ray observations, providing the first detection of decay emission from the  $^{44}\text{Ti}$  decay chain ( $^{44}\text{Ti} \rightarrow ^{44}\text{Sc} \rightarrow ^{44}\text{Ca}$ ). Both the 1.158 MeV line of  $^{44}\text{Ca}$  (Iyudin et al. 1994, 1997) and, more recently, the 67.9 keV and 78.4 keV lines of  $^{44}\text{Sc}$  (Vink et al. 2001) have been measured towards Cas A, and agree with each other to within their quoted errors. These  $\gamma$  observations were received with some surprise by the theoretical community. The mass of  $^{44}\text{Ti}$  implied by the COMPTEL and BeppoSAX observations ( $\sim 2.5 \times 10^{-4} M_{\odot}$ ) exceeds theoretical predictions for  $^{44}\text{Ti}$  yields from typical Type Ib and Type II supernovae (see Figures 1.6 and 1.7; Timmes et al. 1996). Spectral studies of the different velocity components in the Cas A remnant have led to the belief that it is the result of a Type Ib supernova,

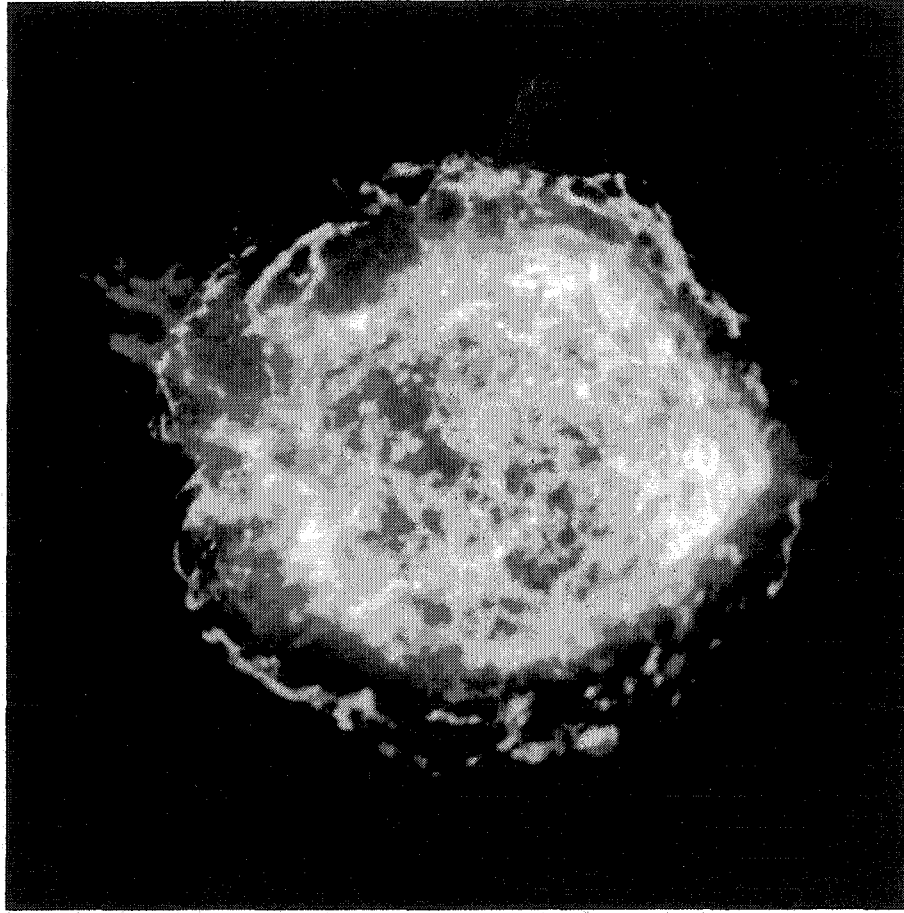


FIGURE 1.4. Million-second Chandra/ACIS X-ray image of Cas A in 3 energy bands. (from Hwang et al. 2004, reproduced by permission of the AAS)

likely a nitrogen-rich Wolf-Rayet star of greater than  $15 M_{\odot}$  (see Fesen, Becker & Blair 1987 for a more in depth discussion).

Regardless of progenitor explosion type (Ib or II), the spherically symmetric model progenitors of Woosley & Weaver (1995) produce relatively similar abundance ratio values for the  $^{44}\text{Ti}/^{56}\text{Ni}$  abundance. Hoffman et al. (1995) argue that the ejection of more  $^{44}\text{Ti}$  from their models would be accompanied by an enhanced ejection of  $^{56}\text{Ni}$  as well. The fact that  $^{44}\text{Ti}$  and  $^{56}\text{Ni}$  go hand in hand supports the constancy of the  $^{44}\text{Ti}/^{56}\text{Ni}$  abundance ratio. For the  $^{44}\text{Ti}$  masses implied by the observations, and assuming that spherically symmetric progenitor explosions hold, the expected

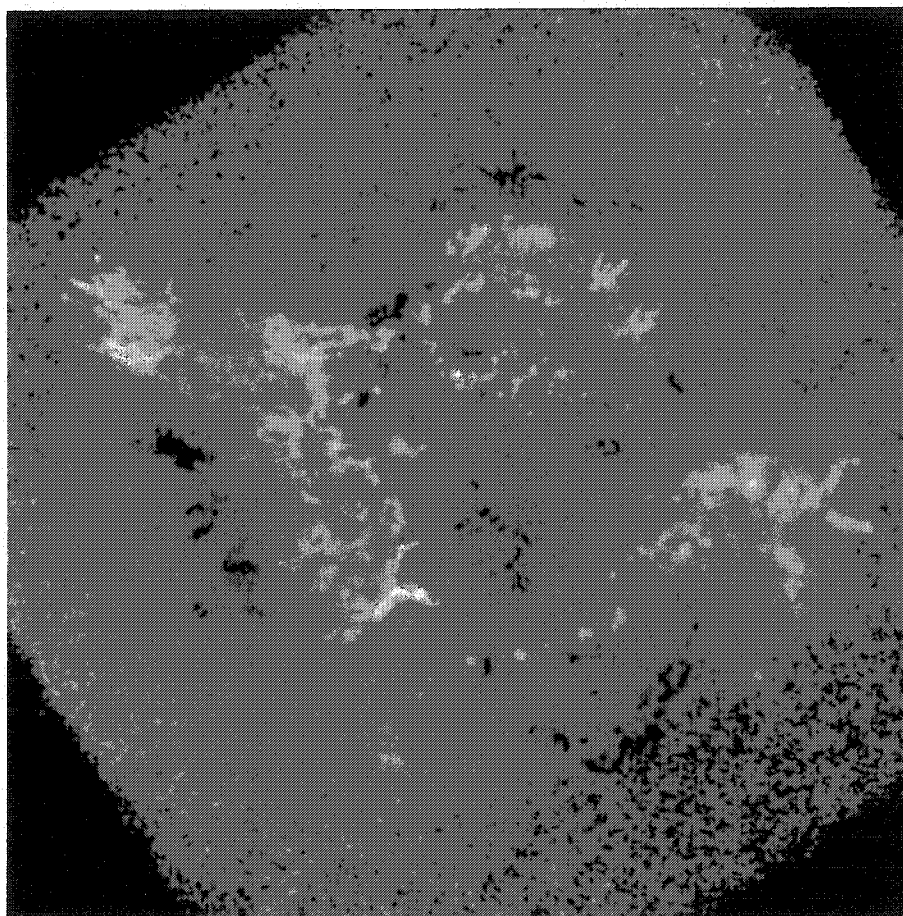


FIGURE 1.5. Chandra/ACIS X-ray image of Cas A depicting the ratio of Si XII to magnesium and iron emission. A well-collimated jet structure is clearly seen. (from Hwang et al. 2004, reproduced by permission of the AAS)

$^{56}\text{Ni}$  yield should have made Cas A a very bright supernova indeed, roughly -4 magnitudes on the sky. It is unlikely that such a bright event would not have made its way into historical accounts of the time, though no such record has been found. In fact, as mentioned above, there is wide acceptance that this supernova was observed in 1680 A.D. by J. Flamsteed at roughly 6th magnitude. Although 10 magnitudes of visual extinction cannot be ruled out, more recent theories suggesting further refinement in our understanding of the explosion and remnant evolution may provide insight on these discrepancies.

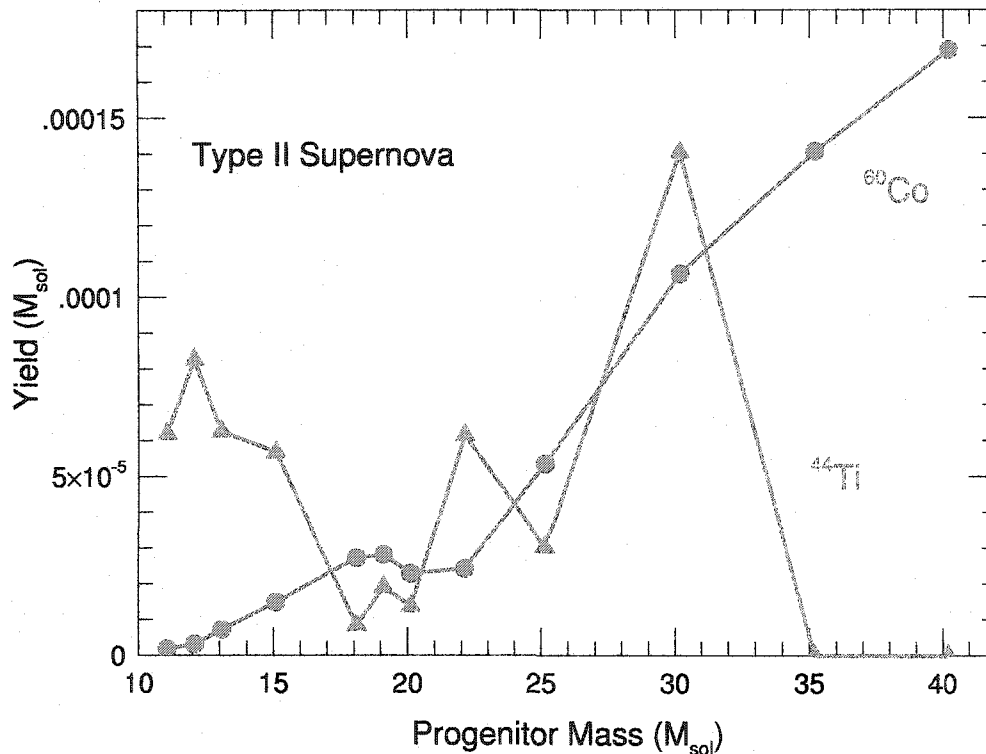


FIGURE 1.6.  $^{44}\text{Ti}$  yields from Type II supernovae. (from Timmes et al. 1996, reproduced by permission of the AAS)

The primary decay channel for the  $^{44}\text{Ti} \rightarrow ^{44}\text{Sc} \rightarrow ^{44}\text{Ca}$  decay chain proceeds via electron capture onto  $^{44}\text{Ti}$  for roughly 99% of the decays, thus creating  $^{44}\text{Sc}$ . Mochizuki et al. (1999) have proposed that material encountered by the reverse shock during the remnant evolution will reach sufficient temperatures to leave the  $^{44}\text{Ti}$  in a highly ionized state for some portion of the evolution. Since the decay via electron capture occurs primarily through the capture of inner shell electrons, sufficient ionization of the isotope blocks its decay, effectively altering its half life. This is the exception to the insensitivity of nuclear decay emissivity to thermodynamic conditions mentioned above. It is significant only for very high temperatures which are experienced by the supernova only in its first day and then again many decades later as a remnant. Because of this effect, the mass of  $^{44}\text{Ti}$  inferred from line flux observations and a laboratory-determined decay lifetime will not correctly

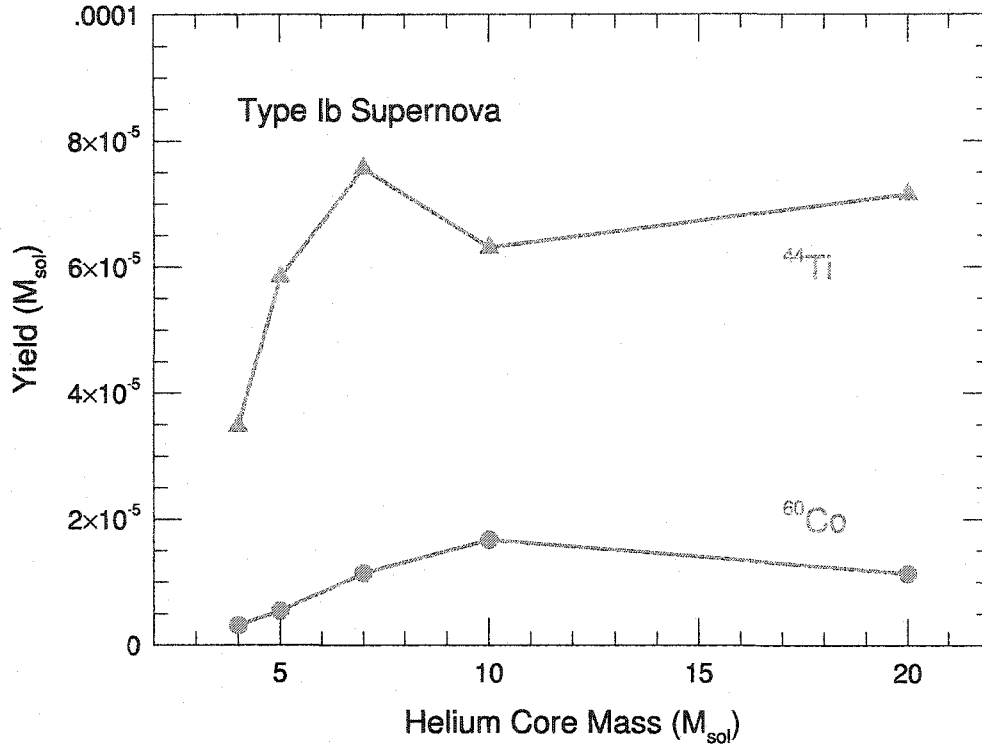


FIGURE 1.7.  $^{44}\text{Ti}$  yields from Type Ib supernovae. (from Timmes et al. 1996, reproduced by permission of the AAS)

reflect the mass of initially-synthesized  $^{44}\text{Ti}$ . Indeed, for the remnant age of Cas A, Mochizuki et al. (1999) show that taking this ionization effect into account brings the observationally-inferred masses into closer agreement with theoretical predictions. In order to achieve the best agreement between theory and observations, the assumption of inhomogeneous clumping of titanium associated with iron-group enriched material was required, though as we have discussed, there is significant evidence for the existence of such inhomogeneity.

An alternative for boosting the  $^{44}\text{Ti}$  emission has been proposed by Nagataki et al. (1998b) and addresses the conditions under which the  $^{44}\text{Ti}$  is synthesized. The primary formation scenario for this isotope is through  $\alpha$ -rich freezeout, which occurs when material in nuclear statistical equilibrium (NSE) at low densities cools so rapidly that the free  $\alpha$  particles present in the NSE ensemble do not have time to merge back

into the iron group via the inefficient triple- $\alpha$  reaction (Timmes et al. 1996). This leaves the heavy nuclei to cool in the presence of a large abundance of  $\alpha$  particles (Woosley, Arnett & Clayton 1973), the capture of which synthesizes heavier nuclei like  $^{44}\text{Ti}$ . The abundance of  $\alpha$  particles is particularly sensitive to the entropy of the gas, with high entropy leading to a larger abundance of  $\alpha$ 's. In this way, higher entropy supernova explosions can enhance the  $^{44}\text{Ti}/^{56}\text{Ni}$  abundance ratio. Nagataki et al. (1998b) have demonstrated this effect using 2D hydrodynamical explosion models with asymmetric initial explosion velocities. The velocity asymmetry (ranging from axis ratios of 2:1 to 8:1 pole versus equator) creates a supernova shock with higher entropy along the polar direction. For the particular case of a Cas A model, they find enhancements by a factor of 3-8 for their range of explosion asymmetries.

For the particular case of Cas A, both the ionization effect (Mochizuki et al. 1999) and the asymmetry effects (Nagataki et al. 1998b) serve to enhance the  $^{44}\text{Ti}$  emission, in agreement with observations. While there are no direct measurements of the  $^{44}\text{Ti}$  decay emission towards SN 1987A, its late-time bolometric lightcurve was (is) observed to be much brighter than could be explained by  $^{56}\text{Ni}$  radioactivity alone.

A compelling explanation for the over-luminous tail of SN 1987A's lightcurve is suggested by Fransson & Kozma (1993). At late times, the recombination time in the supernova becomes longer than the elapsed time and the ionization state of the supernova rises above its steady-state value. Thus, energy which ionized the gas at earlier times is not released until later, boosting the late-time lightcurve of SN 1987A by the observed amount.

An alternative explanation for the late-time lightcurve would be emission from an overabundance of  $^{44}\text{Ti}$  (Timmes et al. 1996). For the current age of the SN 1987A remnant, however, the ionization effect proposed by Mochizuki et al. (1999) would not occur (the ejecta are still far too cold). This would argue more strongly that global asymmetries are playing a role in the supernova explosion. Indeed, attempts to model the mixing implied by the  $\gamma$ -ray observations of SN 1987A, have failed

to produce sufficient mixing to explain the broad [FeII] IR lines. Global explosion asymmetries were suggested early on (Herant et al. 1992) as a possible fix for this lack.

While role of  $^{44}\text{Ti}$  in powering the lightcurve of SN 1987A remains uncertain, it is clear that both Cas A and SN 1987A argue for a closer inspection of the role a global asymmetry may play in the explosion mechanism. At the very least, an angle-dependent explosion asymmetry could significantly change the nucleosynthetic yields during the explosive burning in the supernova. In addition, mixing into the outer envelope will alter the compositional structure of the remnant. Core-collapse supernovae are responsible for most of the heavy element enrichment in the modern universe, yet our current state-of-the-art in theoretical understanding of galactic chemical evolution relies on spherically symmetric explosion models. The evidence for the existence of explosion asymmetry goes well beyond that offered by the  $\gamma$ -ray emission, and suggests that global explosion asymmetries be fairly ubiquitous among core-collapse events. The effects of asymmetry must be taken into account, and for the first time, computing resources seem capable of handling this important problem.

Recent attempts to determine the structure of explosion asymmetries have come from first-principle physics calculations (i.e. core-collapse simulations investigating asymmetries that arise from physical processes like rotation, which are known to play some role in the explosion mechanism.) Observations of  $\gamma$ -ray emission from these objects were among the first to suggest such asymmetries, though from a theoretical perspective, the full diagnostic potential of  $\gamma$ -rays to probe such asymmetries has yet to be studied. This thesis will undertake a theoretical investigation of how underlying explosion asymmetry will manifest itself in  $\gamma$ -ray line diagnostics.

The first step in this process is developing the multidimensional transport code to translate the results of explosion models into  $\gamma$ -ray observables. As all of the results which follow depend upon the correctness of this translation, it is important to establish that the code's results are correct. Fortunately, this can be tested, at



least in 1D, against the work of others. The second chapter of this thesis will thus digress somewhat into the details of numerical simulations of  $\gamma$ -ray transport with the intended goal of verifying the numerical techniques employed.

The third chapter will return to exploring the diagnostic potential of  $\gamma$ -line emission of asymmetries in supernova explosions. Theoretical core-collapse simulations suggest that stellar rotation imparts a bipolar structure on SN explosions (Fryer & Heger 2000). This chapter will investigate the  $\gamma$ -ray signatures of such explosions, and assess whether they can account for all of the features observed in SN 1987A and Cas A. Simulations by Scheck et al. (2004) and by Blondin et al. (2003) show that, neglecting significant rotation, neutrino driven convection and accretion shock instabilities drive explosions through low mode ( $l=1$ ) flows, as was first suggested by Herant (1995). This leads to different, more uni-directional, sorts of asymmetries, and their  $\gamma$ -ray signatures are presented in the final chapter.

## Chapter 2

### CODE DEVELOPMENT AND VERIFICATION

#### 2.1 Monte Carlo Transport Technique

As a first step towards investigating  $\gamma$ -ray emission from asymmetric supernova explosions, we undertake a numerical study of the explosion phase of supernovae ( $t > 100$  seconds post-bounce). For the epochs of interest to  $\gamma$ -ray emission (times beyond 10 days for SNe Ia and 100 days for SNe II) we make the base assumption that the timescale for  $\gamma$ -ray transport out of the SN ejecta (i.e. the typical escape time for a photon) is short compared to the hydrodynamical timescales (i.e. time for significant change in ejecta density)<sup>1</sup>. This allows us to simulate the SN explosion using a purely hydrodynamic code and then use the ejecta properties at various timeslices as a background through which the  $\gamma$ -rays transport (i.e. a time-independent treatment). For this thesis, the asymmetric SN ejecta calculations were run with a pre-existing 3D smoothed particle hydrodynamics code SNSPH (Fryer & Warren 2002). The  $\gamma$ -ray transport in 3D was calculated using a Monte Carlo transport code (Maverick) developed specifically for this thesis research and was designed to simulate the high energy spectrum of supernova explosions from roughly 30 keV to 4 MeV. (See Appendix 1 for further details on Maverick code properties.)

The emphasis of this thesis is on diagnostic signatures of asymmetry in the  $\gamma$ -ray line profiles from core-collapse supernovae. However, a number of earlier studies of

---

<sup>1</sup>Rough calculations of these timescales confirm that such a choice is appropriate. For a given number of scatterings  $N$ , the escape time for the photon is given by its random walk path length divided by the speed of light:  $\frac{\sqrt{N}R}{c}$  where  $R$  is the radius of the ejecta and  $c$  is the speed of light. Assuming that each Compton scattering reduces the photon energy by half, roughly 5 - 10 scatterings occur before the photon escapes at the hard X-ray peak. For  $R = 3 \times 10^{15}$  cm, corresponding to one of our SN II explosions at  $t = 365$  d, the escape time is roughly 3 days. For a homologous expansion, density varies as:  $\frac{\rho}{\rho_0} = \left(\frac{t_0}{t}\right)^3$  which gives a density variation over 3 days (at  $t \sim 365$  d) of:  $\frac{\rho}{\rho_0} = \left(\frac{365}{369}\right)^3 \sim 0.97$ .

$\gamma$ -ray line emission from thermonuclear supernovae have been carried out in spherical symmetry. While the nature of the explosion differs between these two classes of supernovae, the transport physics required to follow  $\gamma$ -ray emission is identical. These existing research codes provide an obvious testbed for verifying my  $\gamma$ -ray transport code Maverick. Using a set of spherically symmetric SN Ia input models, Maverick and 6 other  $\gamma$ -ray transport code efforts from around the world participated in a code comparison project. (Codes employed in the comparison, and referred to by author name, include: Höflich (Höflich, Wheeler & Khokhlov 1998; hereafter HWK98), Pinto (Pinto, Eastman & Rogers 2001), Hungerford et al. (2003), Isern (Isern, Gomez-Gomar, Bravo & Jean 1996), Kumagai (Kumagai et al. 1988), The (The, Burrows & Bussard 1990) and Boggs (ApJ submitted).)

An introduction to the numerical techniques used in these various transport codes is best begun with a brief overview of the general picture of a supernova. For the epochs of interest to high energy observations of supernovae (10 to 150 days for SN Ia and 100 to 400 days for SN II), the supernova expansion is highly supersonic and the density of decay energy remaining is small compared with the kinetic energy density in the ejecta; homologous (coasting) expansion is an appropriate assumption. The ejecta composition includes radioactive species such as  $^{56}\text{Ni}$  and  $^{56}\text{Co}$ , the decay of which provides the  $\gamma$ -ray line emissivity and, through scattering interactions, continuous  $\gamma$ -ray spectrum. The basic interaction processes involving these photons are pair production (PP), photo-electric (PE) absorption, and Compton scattering off free and bound electrons. Figure 2.2 shows a plot of cross sections for these interactions as a function of energy, which shows that the absorptive opacities, PE and PP, are only dominant at low ( $< 150$  keV) and high ( $> 10$  MeV) energies, respectively. The majority of the energy range discussed is dominated by Compton scattering interactions.

As discussed in detail by Ambwani & Sutherland (1988), the picture described above is well-suited for Monte Carlo transport methods. Indeed, six of the seven

codes in this comparison use this stochastic transport technique (namely Höflich, Hungerford, Isern, Kumagai, Pinto and The). The fundamental advantage of Monte Carlo is its ability to accommodate very complicated physical processes in the transport. This is accomplished by simulating the *micro*-physics of the photon's propagation through the supernova ejecta. The principle is very straightforward: the mass of nickel atoms in the input model implies a certain amount of radioactive decay luminosity. Monte Carlo packets (which represent some quantum of photon luminosity) are then launched in proportion to the decay rate and the mass distribution of nickel atoms. Each packet's energy is chosen in proportion to the branching ratios of the possible decay lines and its initial direction is picked at random, thus assuming isotropic emission. The emitted packet is then allowed to propagate through the ejecta, interacting with the material through scattering and absorption. This is a microscopic treatment of the transport in the sense that each individual packet of photons is tracked through each individual interaction.

The likelihood of a photon experiencing an interaction during its flight is dictated by the total cross section for interaction ( $\sigma_{tot}$ ). When an interaction occurs, the type of interaction, scattering or absorption, is chosen randomly in proportion to the ratio of  $\sigma_{scat}/\sigma_{tot}$  or  $\sigma_{abs}/\sigma_{tot}$ . The well-described micro-physics of the PP and PE absorption and the Compton scattering process are explicitly taken into account for each packet interaction, and are thus treated with no approximation. When a packet's path brings it to the surface of the ejecta, it is tallied into the escaping SN spectrum. Likewise, if the path ends in an absorption, the packet's energy is deposited into the ejecta. In this way, the Monte Carlo transport technique allows for straightforward calculation of the emergent hard X- and  $\gamma$ -ray spectrum, as well as energy deposition into the ejecta via photon interactions.

If the emerging line profile of the  $\gamma$ -ray decay lines is the only quantity of interest, semi-analytic techniques alone, as employed by Boggs in this comparison, can be effectively used as well. The Compton equation describes the energy shift a photon

experiences upon suffering a Compton scatter. For the decay lines we are interested in ( $E \sim 1$  MeV), a single Compton scatter shifts the photon's energy out of the decay line profile roughly 97% of the time<sup>2</sup>. This means that the line profiles in the emergent spectrum arise primarily from photons that escape the ejecta without any interaction, with only a few percent contribution from forward-scattered Compton photons. The line profiles can thus be calculated analytically by multiplying the emitted luminosity, as determined from the mass distribution of radioactive species in the ejecta, by the factor  $e^{-\tau}$ , where  $\tau$  is the total optical depth from the emission point to the surface of the ejecta. Analytical techniques such as this provide an invaluable test of the more computationally intensive Monte Carlo technique described above.

Regardless of the transport technique used, bringing the physical properties of the supernova material to a numerical representation requires a series of computational decisions. In the following sub-sections we will review the physics pertinent to these computational choices, which fall into three primary categories: §2.1.1 Description of the Ejecta (Differential Velocity, Density Evolution), §2.1.2 Photon Source Parameters (Lifetimes and Branching Ratios, Positron Annihilation, Ejecta Effects, Weighting), and §2.1.3 Opacities for Photon Interactions (Compton Scattering, Photo-Electric Absorption, Pair Production and Bremsstrahlung Emission. Table 2.1 lists the various codes and provides information regarding the numerical implementations of the physics discussed below.

### 2.1.1 Ejecta

For the different explosion models, the properties of the ejecta are determined by mapping the model into spherical Lagrangian mass zones and expanding this ejecta homologously outward with time. Taking snapshots in time of this ejecta, each  $\gamma$ -ray

---

<sup>2</sup>This assumes a 20 keV line width at  $E = 1$  MeV. The photons which are scattered but remain within the line energy are forward-scattered, meaning they leave the scattering event in roughly the same direction as they entered.

Simulation Creator or Name	Monte Carlo [y/n]	Tag or Spec. <sup>a</sup> [T/S]	Bin Width @ 847 keV [keV]	Line Broad <sup>b</sup> [y/n]	Density Evolve <sup>c</sup> [y/n]	Positr. Fraction f(Ps)	Time Dilation <sup>d</sup> [y/n]	Source Evolve <sup>e</sup> [y/n]	Interactions Treated <sup>f</sup> [CS, PE, PP]
Boggs <sup>1</sup>	N	T	2.8	Y	Y	—	Y	Y	CS, PE
Pinto <sup>2</sup>	Y	S	2.4	Y	Y	0.0	N	N	CS, PE, PP
Höflich <sup>3</sup>	Y	S	2.4	Y	N	1.0	Y	N	CS, PE, PP
Isern <sup>4</sup>	Y	S	2.1	Y	Y	1.0	Y	N	CS, PE, PP
Kumagai <sup>5</sup>	Y	T	50	N	N	0.0	N	N	CS, PE, PP
Hungerford <sup>6</sup>	Y	T	0.5	Y	N	0.0	N	N	CS, PE, PP
The <sup>7</sup>	Y	T	40	N	N	1.0	N	N	CS, PE, PP

<sup>a</sup> Is the line flux derived from determining the escape fraction of “tagged” line photons, or extracted from the spectrum and subject to line blending and continuum contamination?

<sup>b</sup> Are the photons emitted with Doppler broadening due to the differential expansion of the ejecta?

<sup>c</sup> Does the code evolve the ejecta density after the photon emission to account for non-zero crossing times?

<sup>d</sup> Are the relativistic effects of time dilation on the decay rate included?

<sup>e</sup> Does the code account for the effect of requiring simultaneous photon arrival from the near/far side of the ejecta?

<sup>f</sup> The interactions treated are CS = Compton Scattering, PE = Photoelectric Absorption, PP = Pair Production.

REFERENCES: <sup>1</sup>Boggs (ApJ submitted); <sup>2</sup>Pinto, Eastman & Rogers 2001; <sup>3</sup>Höflich, Wheeler & Khokhlov 1998; <sup>4</sup>Isern, Gomez-Gomar, Bravo & Jean 1996; <sup>5</sup>Kumagai et al. 1988; <sup>6</sup>Hungerford et al. 2003; <sup>7</sup>The, Burrows & Burssard 1990.

TABLE 2.1. Characteristics of Transport Codes in Comparison

calculation uses the density, radius, velocity and composition of the ejecta for these mass zones<sup>3</sup>. Some codes simply take the position of the  $^{56}\text{Ni}$  and  $^{56}\text{Co}$ , but others include the motion of the ejecta at varying levels of sophistication. The two major velocity effects are the differential motion and the density reduction due to expansion during the time of flight to escape.

*Differential Velocity* Since the radioisotope is distributed in velocity space and the opacity depends on the relative velocities, the ejecta velocity will affect the propagation of the photon packets. The packets are created with a decay line energy in the co-moving frame of the surrounding ejecta, but are tallied in the rest frame of the observer. The Doppler shift between these two frames is the dominant source of broadening in the line profiles. In Figure 2.1, we show the amount of line broadening possible for four SN Ia models. In addition, as the packet propagates through the ejecta, its energy, as measured in the local co-moving ejecta frame, is constantly changing. Since interaction cross sections are energy-dependent, the opacity through the ejecta for the packet will be different from the case where ejecta velocity is neglected. For our scenario, this is a small effect, as our dominant opacity (Compton scattering) is a slowly varying function of energy.

The Boggs, Höflich, Hungerford, Isern and Pinto algorithms included the ejecta velocity effects, allowing them to calculate detailed line profiles (Table 2.1).

*Density Evolution* Assuming the decision was made to account for ejecta velocity effects, one must then choose whether to allow this motion to feed back on the densities throughout the ejecta. The photon packet does not traverse its path infinitely quickly. Indeed, there is some flight time associated with each packet trajectory, and during this flight time, the ejecta undergoes expansion. This results in lower densities, and

---

<sup>3</sup>The 3-dimensional codes must first map the ejecta onto a 3-dimensional grid. The number and type of nuclei treated in each code varies slightly and abundances were interpolated to match each code separately.

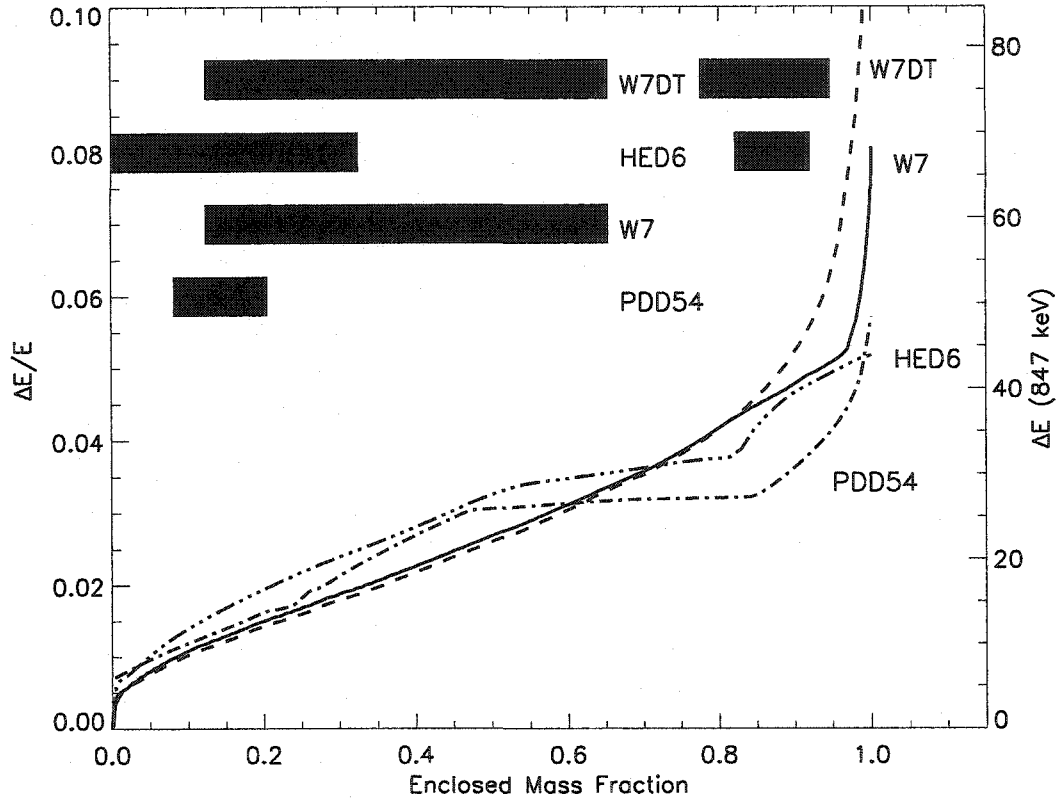


FIGURE 2.1. Line shifting due to the expansion of the ejecta of four SN models. The fractional line shift due to the expansion of the ejecta is plotted on the left axis, the shift for the 847 keV line is shown on the right. For reference,  $^{56}\text{Ni}$ -rich regions of the ejecta are shown in the upper left as thick, horizontal bars. Note  $^{56}\text{Ni}$  at the surface of models W7DT and HED6.

thus lower opacities, as the packet propagates through the star. The alternative to treating this expansion is to assume the transport takes place within a differential time slice  $dt$ , over which the hydrodynamic quantities do not evolve at all. For a homologously expanding ejecta, the density falls off simply as  $t^{-3}$ , making this feedback effect easy to implement. However, accounting for it is only a partial step toward a time-dependent treatment of the problem. The source of the photon packets must also be treated in a time-dependent fashion in order to be self-consistent. Unfortunately, the implementation of the source's time-dependence is not trivial in a Monte Carlo treatment.



Pinto allowed for the ejecta expansion to feedback on the densities. The semi-analytic technique employed by Boggs accounted for both the expansion feedback and the time dependence of the photon source (i.e. photons from the far side of the ejecta take longer to arrive at the detector and must be launched at an earlier time during the explosion<sup>4</sup>. See next section.)

### 2.1.2 Photon Source

Differences in the  $\gamma$ -ray sources include not only  $^{56}\text{Ni}$  and  $^{56}\text{Co}$  decay times and branching ratios, but the emission from positron annihilation. The photon emission rate can be altered in the observer frame by the ejecta velocity structure. Finally, the method of weighting Monte Carlo packets can also pose a problem when normalizing the escaped packet counts into physical flux units.

*Decay Times and Branching Ratios* The source of photons for these high energy calculations is exclusively  $\gamma$ -ray line emission from the decay of various radio-isotopes present in the supernova ejecta. The most important decay chain is that of the radio-isotope  $^{56}\text{Ni}$ . The SN explosion synthesizes  $^{56}\text{Ni}$ , which promptly decays via electron capture to  $^{56}\text{Co}$  with an e-folding time of  $\sim 8.8$  days. The  $^{56}\text{Co}$  produced in this decay is also unstable, though with a longer decay time ( $\sim 111.4$  days). We show in Table 2.2 halflives from the Nuclear Data Sheets (Junde 1999) and branching ratios from the 8th edition of the Table of Isotopes (Firestone 1996). It is apparent from the lower portion of the table that earlier versions of these tables (and others such as “Table of Radioactive Isotopes”, Browne & Firestone 1986) contained mean lifetimes that were as long as 113.7 days for the half-life of  $^{56}\text{Co}$  and as short as 8.5 days for the  $^{56}\text{Ni}$ . This has lead to confusion in the literature as to the correct values. However, we expect the errors caused by the decay times to be less than  $\sim 5\%$ .

---

<sup>4</sup>The effect of the near/far side travel time is most important for the supernova remnant phase; Chan & Lingenfelter 1991.

$^{56}\text{Ni}$ Decay		$^{56}\text{Co}$ Decay	
Energy [keV]	Intensity [phot/100 decays]	Energy [keV]	Intensity [phot/100 decays]
158	98.8	<b>847</b>	<b>100</b>
270	36.5	1038	14
480	36.5	<b>1238</b>	<b>67</b>
750	49.5	1772	15.5
<b>812</b>	<b>86.0</b>	2599	16.7
1562	14.0	3240 <sup>a</sup>	12.5

<sup>a</sup>This line is the sum of a three-line complex.

Source of Half-lives	Reference and Year	$\tau(^{56}\text{Ni})$ [d]	$\tau(^{56}\text{Co})$ [d]
Nuc. Data Sheets	Junde 1999	6.075	77.233
Table of Isotopes(8th)	Firestone 1996	5.9	77.27
Table of Rad. Isotopes	Browne & Firestone 1986	6.10	77.7
Table of Isotopes(7th)	Browne, Dairiki & Doebler 1978	6.10	78.8
Table of Isotopes(6th)	Lederer, Hollander & Perlman 1967	6.1	77

TABLE 2.2. Important Gamma-ray Lines for  $^{56}\text{Ni}$  and  $^{56}\text{Co}$  Decays. Lines studied in this work are listed in bold font. All ratios are from the 8th Table of Isotopes (1996).

Whereas the  $^{56}\text{Ni}$  decay always proceeds via electron capture, the  $^{56}\text{Co}$  decay proceeds either through electron capture (about 81% of decays) or positron production (roughly 19% of decays). It has been suggested (Mochizuki et al. 1999) that the ionization state of the gas can affect the electron-capture decay rates in supernova remnants, since these decays ( $^{56}\text{Ni}$ ,  $^{56}\text{Co}$ ,  $^{44}\text{Ti}$ ) proceed mainly by capturing inner-shell electrons. This effect cannot be important in the pre-remnant phase, as reverse shocks, arising from interactions with circumstellar material, have yet to heat the gas to millions of degrees. The gas temperature in the supernova at times considered in this work is always lower than that needed to create significant vacancy probability for the inner shell electrons. Further, the timescale over which atoms with an inner shell vacancy, due to non-thermal ionization, relax to that vacated shell is far smaller

than the mean time between ionizations. The decay rates are thus essentially the zero-ionization (laboratory) values, and these are the values we have employed.

Shown in Table 2.2 are the relative abundances of the dominant lines from the  $^{56}\text{Ni}$  and  $^{56}\text{Co}$  decays. Note that these values refer to the number of photons emitted per 100 decays of the respective isotope (i.e. this includes the effects of the 19% positron production branching ratio). Clearly, the dominant branches, both for studies of  $\gamma$ -ray line emission and for studies of the energy deposition are the 158, 812, 847 and 1238 keV lines. The exact values for branching ratios and lifetimes of these radioactive decays are subject to revision from further laboratory measurements, as one might expect. As a result, the suite of values used in a  $\gamma$ -ray transport code are chosen from a range of possibilities available in the refereed literature.

For the most part, the values adopted from different references have no noticeable affect on the calculated spectra. The only significant variations in adopted branching ratios from earlier works to the current simulations was with the Höflich code. In previous works, the Höflich code adopted 0.74 for the 812 keV line of  $^{56}\text{Ni}$  decay rather than the 0.86 employed by the other groups. Also, in previous simulations with the Höflich code, it was assumed that the positron production branch left the  $^{56}\text{Fe}$  daughter nucleus always in its ground state (Müller, Höflich, Khokhlov 1991). This led to branching ratios for the  $\gamma$ -ray lines from excited  $^{56}\text{Fe}$  being reduced from the published values by the 19% positron production branching ratio.

*Positron Decay* Absent from Table 2.2 are the 511 keV line and positronium continuum which result from the positron production branch of the  $^{56}\text{Co}$  decay. These positrons are created with a Fermi-Kurie spectrum with a typical energy near  $\sim 600$  keV. Any energy in excess of 511 keV must be transferred to the ejecta before the positron can annihilate with electrons in the ejecta. It is usually assumed that during the epoch of interest for  $\gamma$ -ray line studies of SN Ia ( $\leq 150$  days), positrons thermalize quickly and thus have negligible lifetimes, annihilating in situ. Detailed positron

transport simulations (Milne, The & Leising 1999) have shown that this is not a wholly correct assumption at 150 days; however, only a small error is introduced by making this assumption. Although it is reasonable to assume that the positrons annihilate promptly, in situ, the nature of the resulting emission is not clear. Depending upon the composition and ionization state of the annihilation medium, the positron can annihilate directly with an electron (and produce two oppositely-directed 511 keV line photons in the rest frame of the annihilation), or it can form positronium first. If positronium is formed (and the densities are low enough to not disrupt the positronium atom), 25% of the annihilations occur from the singlet state. Singlet annihilation gives rise to two 511 keV line photons, as with direct annihilation. However, 75% of annihilations occur from the triplet state, which gives rise to three photons. As the three photons share the 1022 keV of annihilation energy, a continuum is produced. This continuum increases in intensity up to 511 keV and abruptly falls to zero.

The resulting spectrum can thus be characterized by the positronium fraction,  $f(\text{Ps})$ , a numerical representation of the fraction of annihilations that form positronium (e.g. Brown & Leventhal 1987):

$$f(Ps) = \frac{2.0}{1.5 + 2.25(A_{511}/A_{posit})}, \quad (2.1)$$

where  $A_{511}$  and  $A_{posit}$  are the observed 511 keV line and the positronium three-photon continuum intensities, respectively. Positronium fractions range between 0 - 1, with most researchers assuming that SN annihilations have a similar positronium fraction as the Galaxy.<sup>5</sup> Utilizing wide-field observations of galactic positron annihilation from the Transient Gamma-Ray Spectrometer (TGRS) on the WIND mission, Harris et al. (1998) estimated the positronium fraction to be  $0.94 \pm 0.04$ . Similarly, utilizing CGRO/OSSE observations of the inner Galaxy, Kinzer et al. (2001) estimated the

---

<sup>5</sup>Note that the positronium fraction function cannot accept continuum fluxes of exactly zero. If  $A_{posit} = 0.0$ , then  $f(\text{Ps}) = 0.0$ , independent of the equation.

positronium fraction to be  $0.93 \pm 0.04$ , both values in agreement with theoretical estimates of interstellar medium (ISM) positron annihilation. However, the composition of SN Ia ejecta is far different than the ISM, being dominated by intermediate and heavy elements rather than hydrogen and helium. The expectation is that charge exchange with the bound electrons of these intermediate and heavy elements would lead to SN ejecta having a positronium fraction of at least 0.95. Thus, ISM annihilation is completely different than SN ejecta annihilation. Likewise, the galactic annihilation radiation measured by OSSE is a diffuse emission, and is also distinct from the in situ annihilations that occur in SN Ia ejecta within 200 days of the SN explosion. In light of these differences, a zero positronium fraction for annihilations that occur in SN ejecta cannot be ruled out.

For our purposes here, it suffices to say that the expected spectrum from positron annihilation is uncertain, and the different codes have adopted positronium fractions of either 0 (Hungerford, Kumagai, and Pinto) or 1 (Höflich, Isern, and The); see Table 2.1 for a summary. The three groups employing positronium fractions of 1 adopted the energy distribution of the positronium continuum treatment in Ore & Powell (1949).

*Ejecta Effects on Decay* The motion of the ejecta can also change the decay rate. The rate equations for  $^{56}\text{Ni}$  and  $^{56}\text{Co}$  decays are:

$$\frac{1}{\text{Ni}_o} \left( \frac{d\text{Ni}}{dt} \right) = -\frac{1}{\tau_{\text{Ni}}} \exp \left( \frac{-t}{\tau_{\text{Ni}}} \right), \quad (2.2)$$

$$\frac{1}{\text{Ni}_o} \left( \frac{d\text{Co}}{dt} \right) = \frac{-1}{\tau_{\text{Co}} - \tau_{\text{Ni}}} \left[ \exp \left( \frac{-t}{\tau_{\text{Co}}} \right) - \exp \left( \frac{-t}{\tau_{\text{Ni}}} \right) \right], \quad (2.3)$$

where,  $\tau_{\text{Ni}}$  and  $\tau_{\text{Co}}$  are the mean lifetimes of the isotopes,  $\text{Ni}_o$  is the  $^{56}\text{Ni}$  produced in the SN explosion, and  $t$  is the time since explosion. For a given model time ( $t = t_m$ ),

these equations can be solved for the number of Nickel and Cobalt atoms that will decay during an infinitesimal time slice  $dt$ . These equations still hold integrated over a finite time step  $\Delta t$ , assuming  $\Delta t$  is much less than the lifetime  $\tau$ . Strictly speaking, the lifetimes ( $\tau_{Ni}$  and  $\tau_{Co}$ ) in the above equations are in the frame of the isotope, which is moving relative to an external observer. Since the velocity of the ejecta can be upwards of  $10,000 \text{ km s}^{-1}$ , an exact treatment of the decay rate must include a conversion to the frame of the external observer. This relativistic effect is proportional to  $\gamma = (1 - v^2/c^2)^{-1/2}$  and is only a 0.1-0.2% effect overall. Aside from Boggs, none of the codes include this effect.

More important is the flight time of the photons through the ejecta. In the context of Equations (2) and (3) it is straightforward to point out where to accomplish this. Emission from the near side of the ejecta should be calculated from the above equations using a retarded time relative to the far side. In this way, photons from the front and back of the ejecta arrive simultaneously at the detector. The flight time of the photons introduces less than a 10% error. Again, Boggs' code is the only one that incorporates these effects. Keep in mind, however, that the high energy observations of these objects are difficult and generally require several weeks integration time to make a detection at all. These ejecta effects contribute some error in the context of detailed spectral comparisons between simulated spectra, but are washed out by the long time integrations required by current observations.

*Weighting* The last uncertainty is purely numerical in nature and arises from the weighting (and subsequent normalization) of the photon packets. Combining the decay rate with the branching ratios, which provide a measure of the average number of photons per decay, Equations (2) and (3) yield a total photon luminosity ( $\mathcal{L}_{phot}$ ) of the ejecta (in phot/s). Given the number of photon packets to be tracked in the simulation ( $\mathcal{N}_{packet}$ ), the weight of each packet is

$$W_{packet} = \frac{\mathcal{L}_{phot}}{\mathcal{N}_{packet}}.$$

More complicated weighting algorithms are possible, and provide reduced variance when specialized information is desired. For example, detailed studies of the spectral characteristics for weaker decay lines benefit from emitting a large number of packets at the decay energies of interest. In this way, the signal-to-noise of the spectrum at those weak lines is enhanced beyond what the uniform weighting technique could provide. In any case, the normalization applied via this weight factor can be taken into account from within the transport code itself, or as a post-process step on the photon packet counts, which result from the base Monte Carlo transport routine. The validity of the normalization is easily tested through the analysis of the integrated line flux lightcurves for the various decay lines. These lightcurves can be directly compared with the semi-analytic technique discussed above for decay lines with energies greater than about 1 MeV (i.e. where the continuum has a negligible contribution to the spectrum.) For our study, all the Monte Carlo algorithms were run using constant weight packets to reduce the complexity of the comparison, but as we shall see, it is the weighting and the subsequent normalization of the flux that caused many of the discrepancies in past simulations (see §2.2.3).

### 2.1.3 Photon Interaction Processes

Once the decay photons have been created, their propagation through the ejecta is dictated by the three interaction processes mentioned at the start of this section: Pair-Production, Photo-Electric absorption and Compton scattering. The major features of the spectrum, with the exception of actual line fluxes, can be understood primarily through the PE absorption and Compton scattering interactions.

*Compton Scattering* For the majority of the energy range we are interested in, Compton scattering interactions off electrons dominate. This interaction depends only on

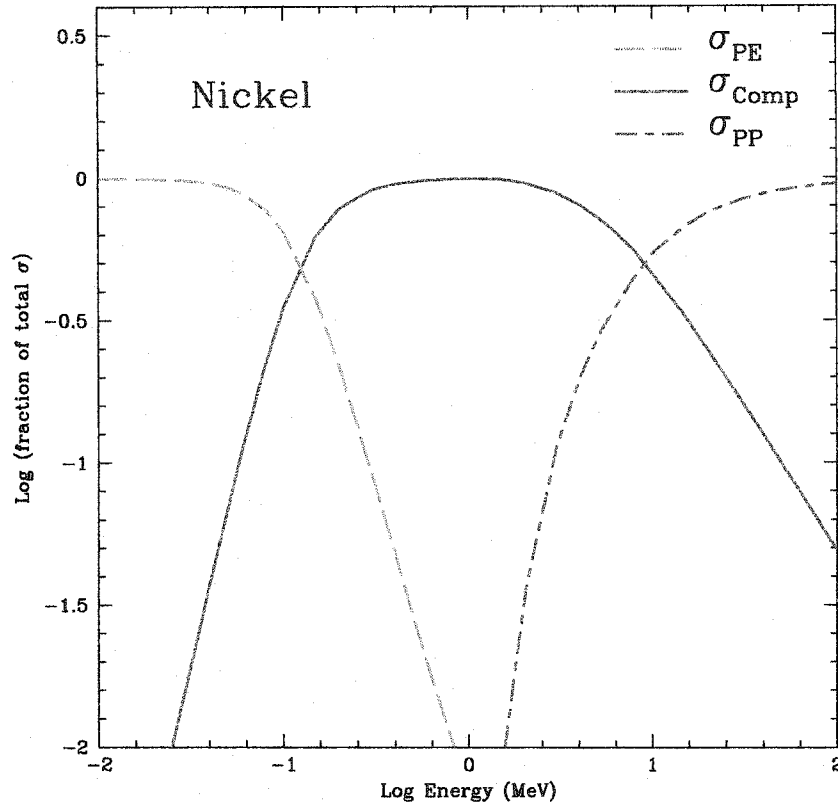


FIGURE 2.2. Photon cross sections for the 3 primary opacity sources to  $\gamma$ -rays: Photoelectric absorption, Compton Scattering, and Pair production. Y-axis is the fraction of the total cross section made up by each process in log space. Pair production and Photoelectric opacities are taken from the LLNL Evaluated Nuclear Data Library (Plechaty, Cullen & Howerton 1981). Compton cross section values are taken from Equation 2.4 (Raeside 1976).

the energy of the incident photon and the *total* electron density in the ejecta, as the roughly 10 keV binding energy of K-shell electrons is small in comparison to the 1 MeV photon energy. Since almost all SN Ia ejecta has an electron fraction  $Y_e \sim 0.5$ , this interaction is only weakly dependent upon the composition.

Figure 2.2 (data taken from Plechaty, Cullen & Howerton 1981 and Raeside 1976) shows the energy dependence of the cross-section for Compton scattering as employed by the various groups. This cross-section is a smoothly varying function of energy:



$$\sigma_{\text{Compton}} = \frac{3\sigma_{Th}}{8\epsilon} \left[ \left[ 1 - \frac{2(\epsilon + 1)}{\epsilon^2} \right] \ln(2\epsilon + 1) + \frac{1}{2} + \frac{4}{\epsilon} - \frac{1}{2(2\epsilon + 1)^2} \right], \quad (2.4)$$

where  $\sigma_{Th}$  is the Thomson scattering cross-section, and  $\epsilon$  is the ratio of the photon energy to the electron rest mass.

While photo-electric absorption and pair-production interactions consume the photon, the scattering process produces a lower energy photon traveling in a new direction. The down-conversion of the photon's energy is the dominant process for populating the hard X-ray continuum, and the exact energy distribution of the outgoing photons is described by the Klein-Nishina (KN) differential scattering cross-section. The KN formula is given by (Raeside, 1976)

$$\frac{d\sigma}{d\epsilon'} = -\frac{3\sigma_{Th}}{8} \left( \frac{1}{\epsilon} \right)^2 \left[ \frac{\epsilon}{\epsilon'} + \frac{\epsilon'}{\epsilon} - 1 + \left( 1 - \frac{1}{\epsilon'} + \frac{1}{\epsilon} \right)^2 \right], \quad (2.5)$$

where  $\epsilon$  is the photon's incoming energy and  $\epsilon'$  is the photon's outgoing energy. Given  $\epsilon$ , many techniques exist for sampling an outgoing energy from this relation. In particular, Maverick uses a combined inversion-rejection sampling technique by Kahn (1954). Combining the outgoing energy with the Compton formula, given by

$$\cos(\theta) = \left( 1 - \frac{1}{\epsilon'} + \frac{1}{\epsilon} \right), \quad (2.6)$$

an outgoing photon direction is then determined. From this equation it is easy to see that forward-scattered photons (with  $\theta = 0^\circ$ ) result in unaltered outgoing energies.

Detailed comparisons of the individual sampling techniques used by the various groups have not been done. However, for the six groups that track the scattered photons, the continuum in their simulations is produced predominantly through the scattering interaction. Fortunately, the shape of this Comptonized continuum (200 keV - 800 keV) is a direct and sensitive test that the physics of photon-electron scattering has been implemented appropriately.

*Pair-Production and Photo-Electric Absorption Opacities* For the epochs we are interested in, the optical depth for Compton scattering does not drop to the point that insufficient Comptonization is a concern. However, at low energies (less than  $\sim 200$  keV), the smooth, nearly power-law continuum created from Compton scattering does suffer a turn over due to photoelectric absorption effects. Just as in the adoption of values for branching ratios and decay lifetimes, the literature offers more than one reference for choosing absorptive opacities. The PE and PP opacities employed by the various groups in our collaboration can be found from three primary references (Viegle 1973, Hubbell 1969, and Plechaty, Cullen, & Howerton 1981), which provide these cross sections in tabular form (by energy and proton number.) Techniques for interpolating cross sections from the provided energy table values varied among the different groups. The number of nuclei species (different proton numbers), which were considered as contributors to these absorptive opacities, were also treated differently in the various codes. These types of variations in the numerical implementation ought to manifest themselves as slight changes in the location of the low energy spectral cut off.

In addition, both of these absorptive interactions allow for the possibility of high energy photon daughter products: annihilation photons for the case of pair production, and X-ray fluorescence photons for the case of photo-electric absorption. The decision to include these processes and the technique for implementing them varied among groups. The X-ray fluorescence photons are below the low energy cutoff and, thus, contribute predominantly to the calculated deposition energy. In this paper we concentrate only on the emergent spectrum, and thus do not probe the differences caused by the inclusion of the X-ray fluorescence.

*Bremsstrahlung Emission* Another important photon emission process from the ejecta is the bremsstrahlung process of the energetic Compton-recoil electrons ( $E \leq 3$  MeV; recoiling from Compton scattering events with the primary radioactivity  $\gamma$ -rays). This

bremsstrahlung process takes place in all supernovae that are powered by radioactive decay. The large abundance of these electrons gives rise to the dominance of bremsstrahlung photons as the hard X-ray source; i.e., below 30 keV and 60 keV at  $20^d$  and  $80^d$ , respectively in both models W7 and DD4 (Clayton & The 1991; Pinto, Eastman, & Rogers 2001). The shape of the bremsstrahlung spectrum emerging from the surface is sensitive to the photoelectric opacity and with the flux,  $F(E) \propto E^\alpha$  where  $\alpha$  is  $\sim 1.1$  and  $\sim 1.8$  at  $20^d$  and  $80^d$ , respectively for model W7 (Fig. 13 of Clayton & The 1991); the spectral luminosity increases slowly between 1 and 60 keV. The sudden change in the hard X-ray slopes between 10 keV and 100 keV (from the bremsstrahlung spectrum at lower energies to the Compton scattering spectrum at higher energies) can be used as the signature of this process. None of the simulations in this comparison project included this process.

## 2.2 Code Comparisons

All the codes included in this study, with the exception of Maverick, have produced published simulations of SN Ia models, though until now, not of the exact same model. Indirect comparisons between those published works suggest that different codes produce different quantitative (and even qualitative) results. Notably, HWK98 and Kumagai & Nomoto (1997) both predict larger line fluxes than Pinto, Eastman & Rogers (2001), Milne, Kroeger, Kurfess & The (2002) or Boggs (*ApJ* submitted), though as we will discuss below, the Kumagai fluxes are high by a constant factor in time, while the Höflich fluxes are enhanced by an epoch-dependent factor. However, determining the cause of such spectral variations has been difficult since, as mentioned before, no single input Ia model has been simulated by all groups. While it is generally agreed that SNe Ia are caused by the thermonuclear explosion of an accreting WD, there remains considerable controversy as to the exact nature of the progenitor and the physics behind the development of the burning front: deflagration vs. detonation,

Model Name	Mode of Explosion	Ref.	$M_*$ ( $M_\odot$ )	$M_{Ni}$ ( $M_\odot$ )	$E_{kin}$ ( $10^{51}$ ergs $s^{-1}$ )
Algorithm Comparison					
DD202C	Delayed det.	(1)	1.40	0.72	1.33
HED6	He-det.	(2)	0.77	0.26	0.74
W7	Deflagration	(3)	1.37	0.58	1.24
Spanning Explosions					
PDD54	Pul.del.det.	(4)	1.40	0.14	0.35
W7DT	Late det.	(5)	1.37	0.76	1.61
HED8	He-det.	(2)	0.96	0.51	1.00
HECD	He-det.	(6)	1.07	0.72	1.35
DET2	Merger det.	(2)	1.20	0.62	1.55
DET2ENV2	Merger det.	(2)	1.40	0.62	x.xx
DET2ENV6	Merger det.	(2)	1.80	0.62	1.33

TABLE 2.3. Characteristics of SN Ia Explosion Models

number of ignition sites (e.g. Livio 2000). These differences have produced a set of SN Ia explosion models in terms of a handful of parameters that form the basis for comparisons with SN observations. This project provides the much needed direct comparisons by running all seven  $\gamma$ -ray transport codes on the same set of SN Ia explosion model inputs. The set of three models that were selected for comparisons are DD202C (a Chandrasekhar-mass delayed detonation, Höflich, Wheeler & Thielemann 1998), HED6 (a sub-luminous, sub-Chandrasekhar mass Helium detonation, Höflich & Khokhlov 1996) and W7 (a Chandrasekhar-mass deflagration, Nomoto, Thielemann & Yokoi 1984). In Table 2.3, we show the relevant characteristics of the models. Errors were introduced by imperfections in the conversion of each model into the varied formats required by each code. Typically these errors were 2-3% of the mass or kinetic energy and were found to have a negligible effect upon the Compton-scattering dominated portion of the spectra.

For these comparisons, we focus on three aspects of the  $\gamma$ -ray calculations: the

overall spectra, the line profiles and the most important observed quantity for future  $\gamma$ -ray missions, the line flux.

### 2.2.1 Overall Spectra

Figures 2.3 - 2.5 show a sequence of spectra from simulations of DD202C, W7, and HED6, respectively. These spectral results arise from current versions of the 6 Monte Carlo codes employed in this comparison and agree to within the statistical noise except in a few cases. The remaining differences in the spectral simulations can be isolated in terms of the physical processes outlined in §2.1. For example, in Figures 2.3 and 2.4 at the earliest epoch, it is clear that the Höflich spectra exhibit a different continuum slope across the rough energy range of 200 keV - 800 keV. The shape of the continuum in this portion of the spectrum is dictated primarily by the Klein-Nishina differential scattering cross section, although physical effects such as Doppler corrections for the ejecta velocities may also change the overall spectral slope. Closer inspection of the Compton scatter and Doppler boost routines between Höflich and other codes did not reveal an obvious cause for this difference, which has a maximum magnitude of order 30% but is much smaller across most of the energy range.

As discussed in §2.1.2, spectral variations due to differences in the assumed positronium fractions should appear in the 400 - 550 keV energy range (Figures 2.3 - 2.5). At late times, one would expect the codes that include the positronium continuum to have slightly higher continuum spectra and weaker lines. There is very little difference between the codes that include a positronium continuum component (Höflich, Isern, and The) and those that do not (Hungerford, Kumagai, and Pinto), but the expected trends seem to hold. As these spectra likely bracket the range of possible annihilation spectral features, the treatment of the positronium fraction primarily affects the strength of the 511 keV line, and it does not dominate the appearance of the continuous spectrum.

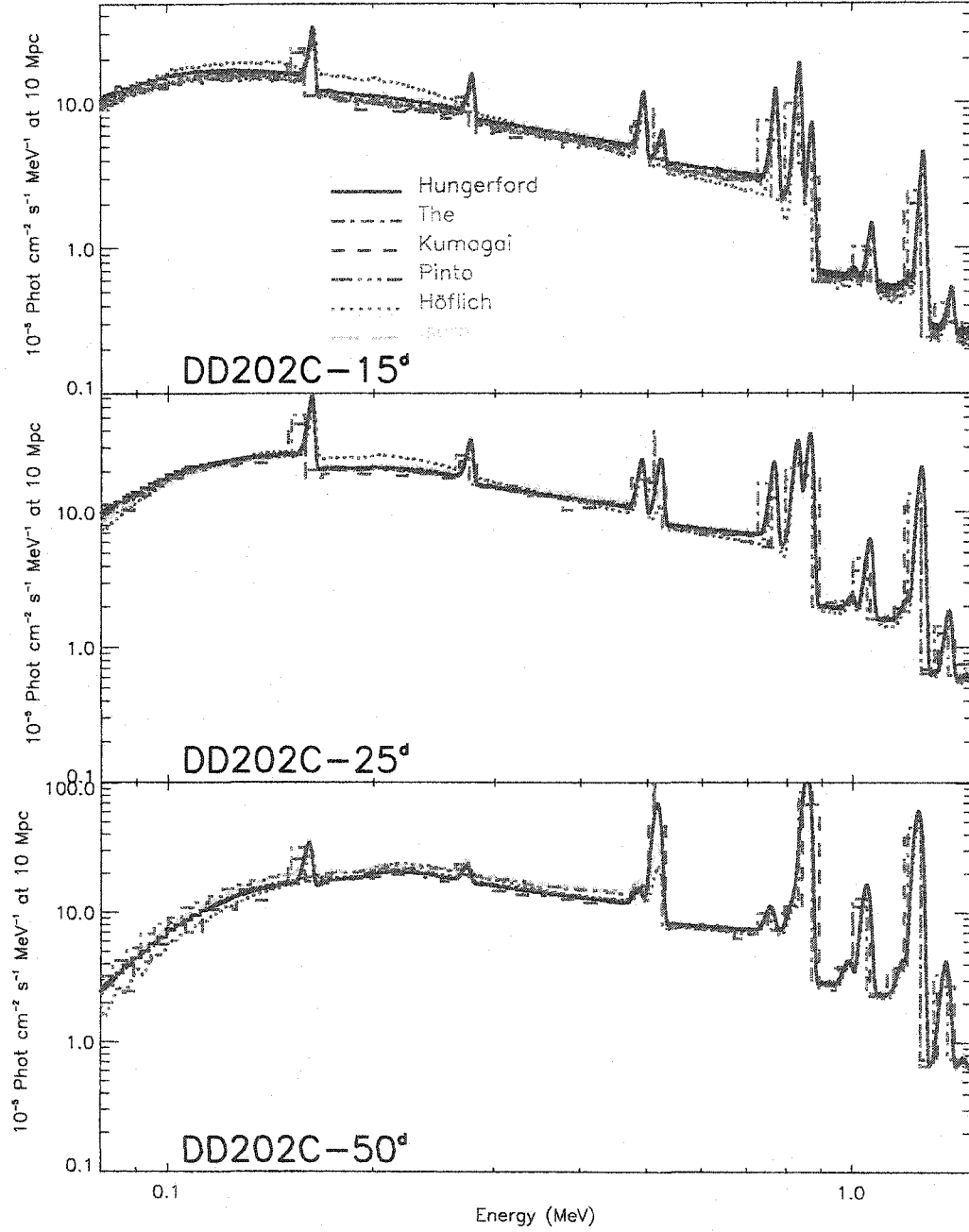


FIGURE 2.3. A sequence of spectra for the SN Ia model, DD202C. The spectra, at  $15^d$ ,  $25^d$ , and  $50^d$ , show the level of agreement between simulations for both the line and continuum emission. Comparisons between the two codes that do not treat line broadening/shifting (The & Kumagai) and the others that do, show the early effects of blue-shifting.

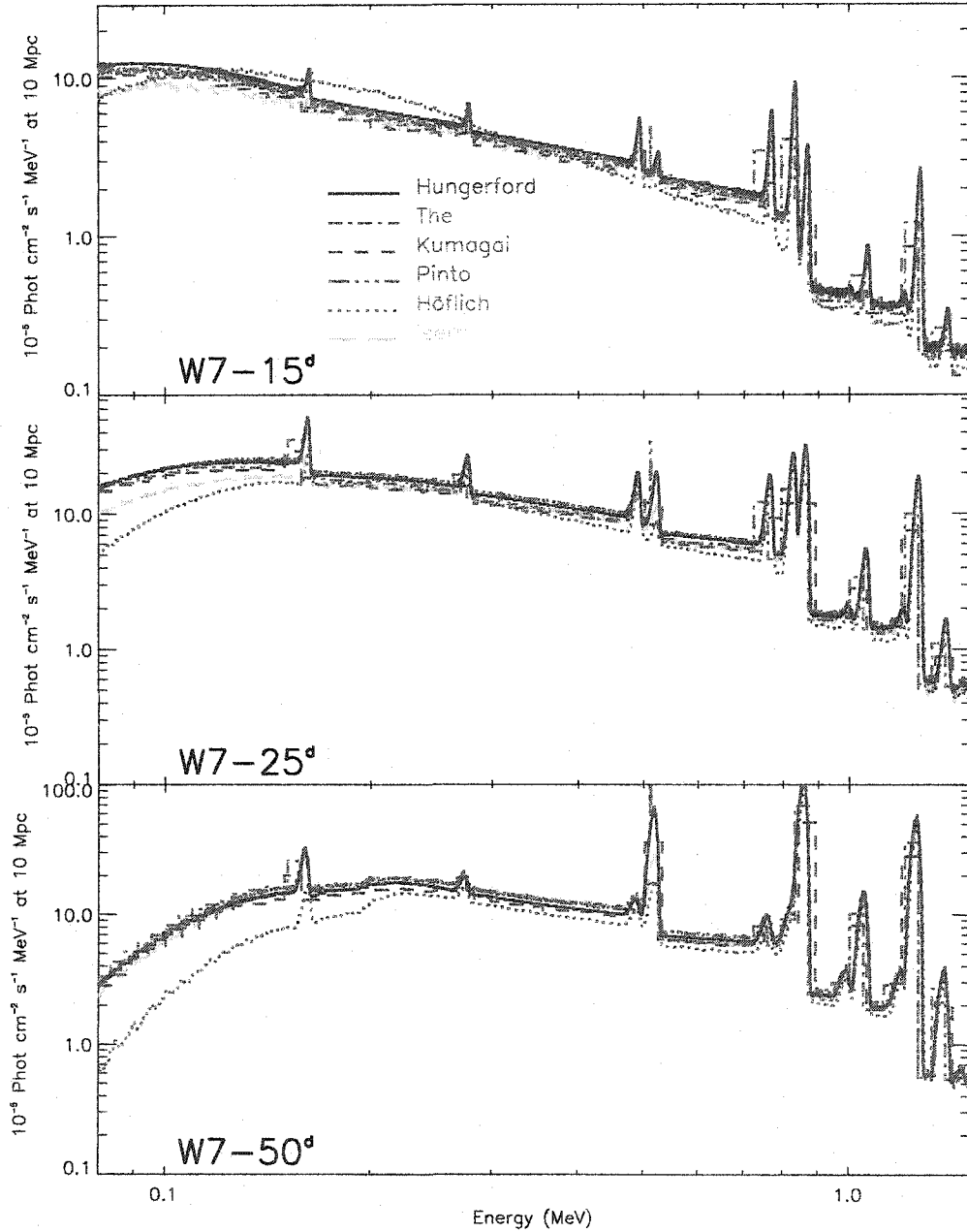


FIGURE 2.4. A sequence of spectra for the SN Ia model, W7. The absence of nickel near the surface of W7 leads to the inhibition of line emission until later times. As with DD202C, the spectra, at  $15^d$ ,  $25^d$ , and  $50^d$ , show a high level of agreement between simulations for both the line and continuum emission.

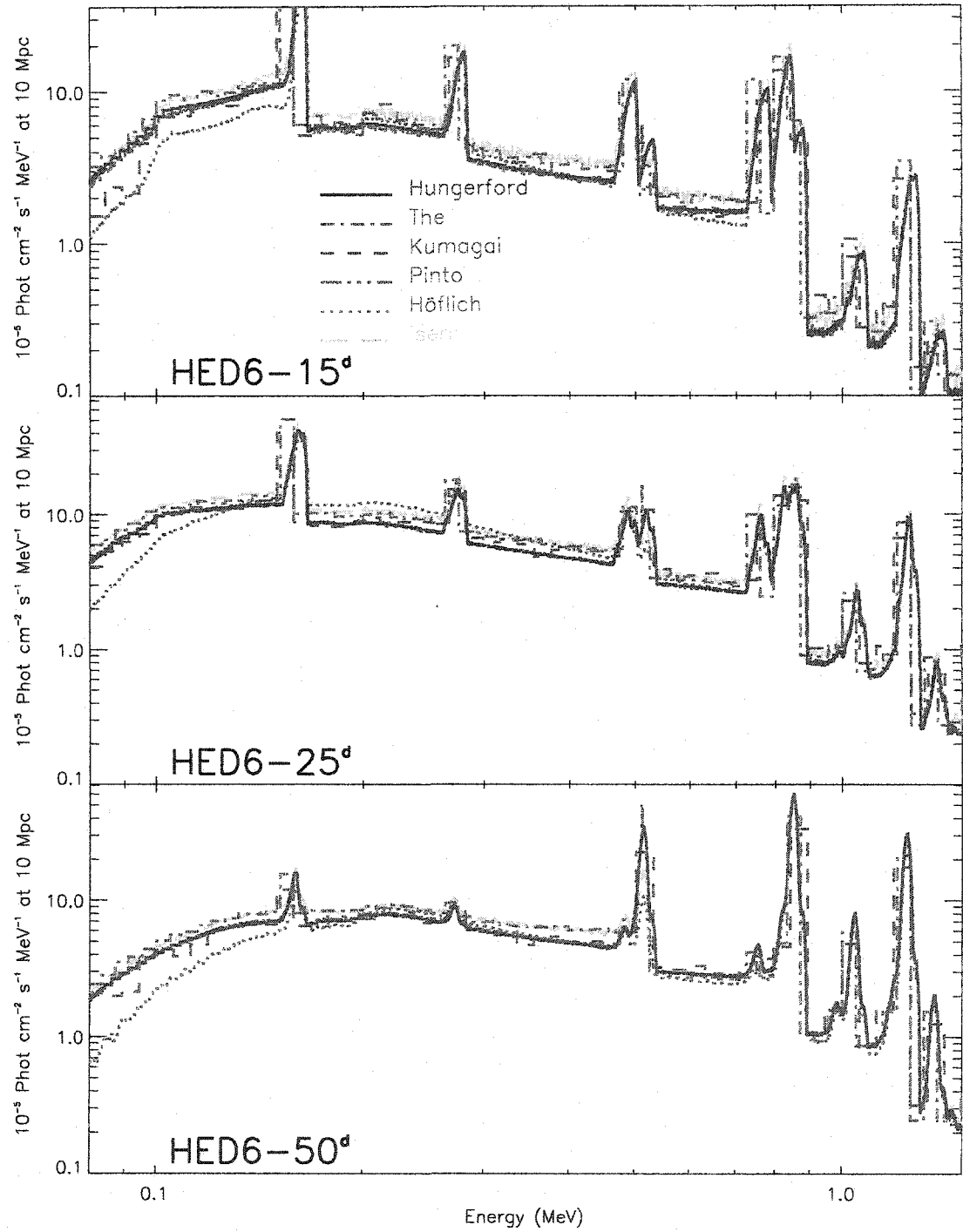


FIGURE 2.5. A sequence of spectra for the SN Ia model, HED6. The spectra, at  $15^d$ ,  $25^d$ , and  $50^d$ , show a high level of agreement between simulations, in this case for a low-mass model that features early escape of  $\gamma$ -ray emission.



There also remain differences in the  $\leq 100$  keV spectra that exceed statistical fluctuations. These differences likely arise from differences in the implementation of photoelectric absorption opacities. Differing interpolation techniques for the tabular opacities, to account for the difference in number of nuclear species treated, may be responsible for these discrepancies. As the emphasis of this comparison is on the higher energy  $\gamma$ -ray portion of the spectrum, we did not attempt to resolve these opacity differences.

### 2.2.2 Line Profiles

In Figures 2.6 and 2.7 we show line profiles of the 1238 keV line and the 812 & 847 keV line complex. The Boggs simulations are specifically of line profiles, and thus they contribute only to these two figures and not the previous three. The Kumagai and The codes did not produce line profiles and are thus not included in these figures. We note that Burrows & The (1990) did simulate line profiles by adopting the technique of Bussard et al. (1989) and similar to that of Chan & Lingenfelter (1987).

The Boggs line profiles, shown in Figures 2.6 and 2.7, do not include the Compton scattered photons from higher-energy nuclear lines. The close agreement of the Boggs line profiles with the lines from other codes suggests that the continuum photons generated by the Compton downscattered photons have only a small effect on the line emission profile. The continuum photons would only become important if an instrument's energy resolution is poor enough that it samples beyond the energy ranges shown in these figures.

Although detailed line profile observations require instrument sensitivities beyond those currently available (for all but the nearest supernovae), their diagnostic potential for distinguishing between Ia explosion models is very strong. Because the line photons arise primarily from non-interacting  $\gamma$ -rays, the line shape is a direct probe of the spatial distribution of  $^{56}\text{Ni}$  synthesized in the supernova explosion. For a more

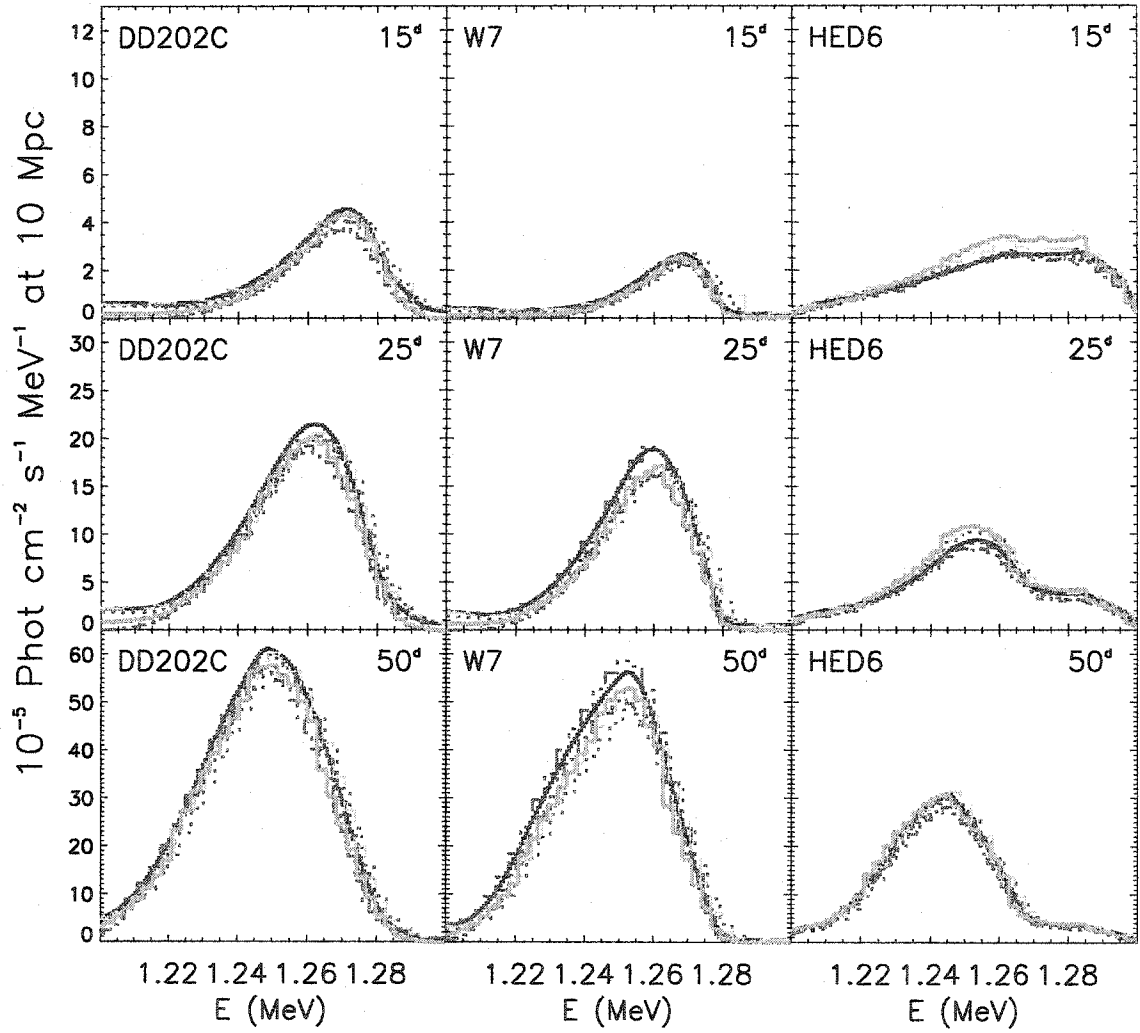


FIGURE 2.6. Line profiles of the 1238 keV line for the SN Ia models, DD202C, W7, HED6. Although the simulations show noticeable variations, the differences between the Chandrasekhar-mass models (DD202C & W7) and the sub-Chandrasekhar-mass model (HED6) greatly exceeds the variations between simulations. Differentiating between DD202C & W7 is more difficult, but is not rendered impossible by the variations between simulations if a sequence of spectra were available for comparison.

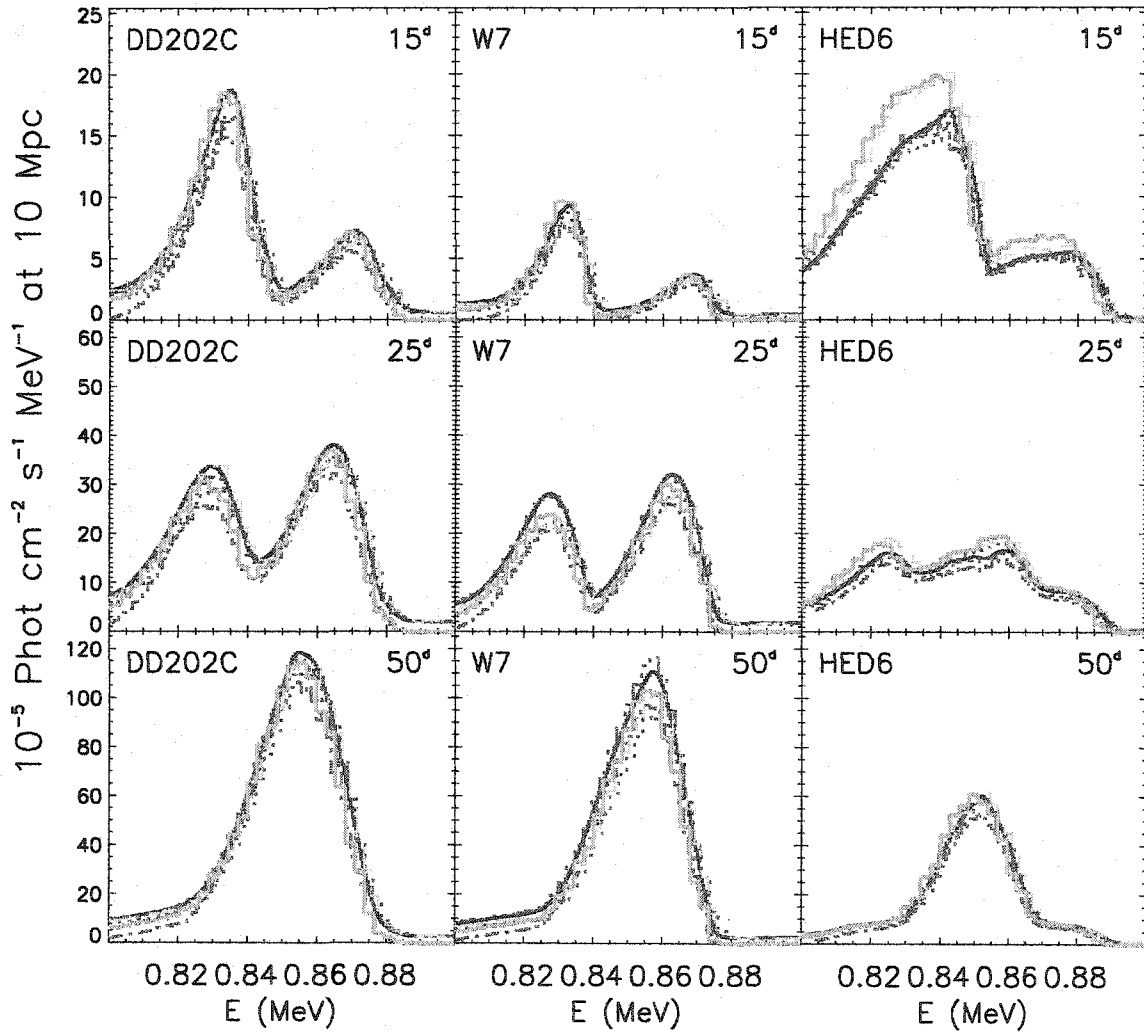


FIGURE 2.7. Line profiles of the 812 & 847 keV line complex for the SN Ia models, DD202C, W7, HED6. The interpretation is similar to that of the 1238 keV line: the differences between the Chandrasekhar-mass models (DD202C & W7) and the sub-Chandrasekhar-mass model (HED6) greatly exceeds the variations between simulations, and while differentiating between DD202C & W7 is more difficult, it is not rendered impossible by the variations between simulations if a sequence of spectra were available for comparison.

detailed discussion of the potential for such observations with current and planned missions, see HWK98.

### 2.2.3 Line Fluxes

A far easier observation to make, and the quantity more frequently published from theoretical simulations, is the time evolution of integrated line fluxes ( $\gamma$ -ray light curves). Since the Kumagai and The codes do not include ejecta velocity effects, they compare line emission with the other codes only through integrated flux values, obtained by tallying “tagged” line photons (i.e. a photon created at the  $\gamma$ -line energy is tagged as such and contributes to the integrated flux if it escapes with no interaction).

Such comparisons of the lightcurves from previously published results in HWK98 (for DD202c and HED6) revealed significant differences in the magnitude and shape of the 812, 847 and 1238 keV lightcurves from the results presented here. Further inspection of the overall spectra from HWK98 confirmed that the spectra were similar in shape, but tended to be brighter by an epoch-dependent factor. Closer study of the Höflich code determined that a post-process step, required for correct weight normalization of the Monte Carlo packets, was performed incorrectly in the HWK98 spectra. (For details, see the erratum for Höflich, Wheeler & Khokhlov 1998; Höflich & Wheeler 2004) When corrected for the appropriate weight factor, which was equal to the total escape fraction for each epoch, the HWK98 spectra roughly agree with the spectral results in this work.

Lightcurve results from Kumagai & Nomoto (1997) for model W7 also demonstrated an enhanced flux level, although the lightcurve shape was similar to the results found here. Comparisons with previously published W7 spectra (Kumagai & Nomoto 1997; Kumagai, Iwabuchi & Nomoto 1999; Iwabuchi & Kumagai 2001) reveal consistent results with the overall spectra presented in §2.2.1. This points to an offset problem in the generation of the integrated flux data, possibly related to

setting the SN at a given distance and/or scalings in the  $^{56}\text{Ni}$  mass of the explosion model.

*1238 keV Line Flux* The 1238 keV  $^{56}\text{Co}$  decay line is the most straightforward line flux to study. This line is isolated from other lines and there is little continuum emission to contaminate line flux estimates. We define the 1238 keV line to be all photons with energies between 1150 - 1300 keV. Shown in Figures 2.8 and 2.2.3 are the 1238 keV light curves for DD202C, W7 and HED6. For comparison, we include earlier light curves from HWK98 and Kumagai & Nomoto (1997), although those works did not use the same line definitions used in this work.

The HWK98 light curves (DD202c and HED6) are enhanced at early times and slightly fainter than the current simulations at late times, demonstrating the trends from the missing weight normalization (discussed above) and the lowered  $^{56}\text{Co}$  decay branching ratios (see §2.1.2). The Kumagai & Nomoto (1997) light curve for W7 appears too bright at all epochs, consistent with some offset introduced during the calculation of integrated line fluxes.

The three codes that derive line fluxes from tagged photons (The, Kumagai & Boggs) yielded similar light curves to the other four codes, which obtained line fluxes from spectral extraction techniques. This suggests that the extraction of the line flux from the spectra can be performed in a manner that does not introduce appreciable systematic errors in the light curves. It is worth reiterating that ultimately spectra must be compared with observations in order to infer the nickel production from an actual supernova, so the fact that the line fluxes were adequately extracted from the spectra is encouraging for the astrophysical use of these simulations.

*812 keV and 847 keV Line Fluxes* The two brightest  $\gamma$ -ray lines occur at 812 keV and 847 keV. The former is produced by  $^{56}\text{Ni} \rightarrow ^{56}\text{Co}$  decays, while the latter is produced by  $^{56}\text{Co} \rightarrow ^{56}\text{Fe}$  decays. The high-velocity expansion of the ejecta creates Doppler broadening that blends the two lines. Ultimately, when observed with an

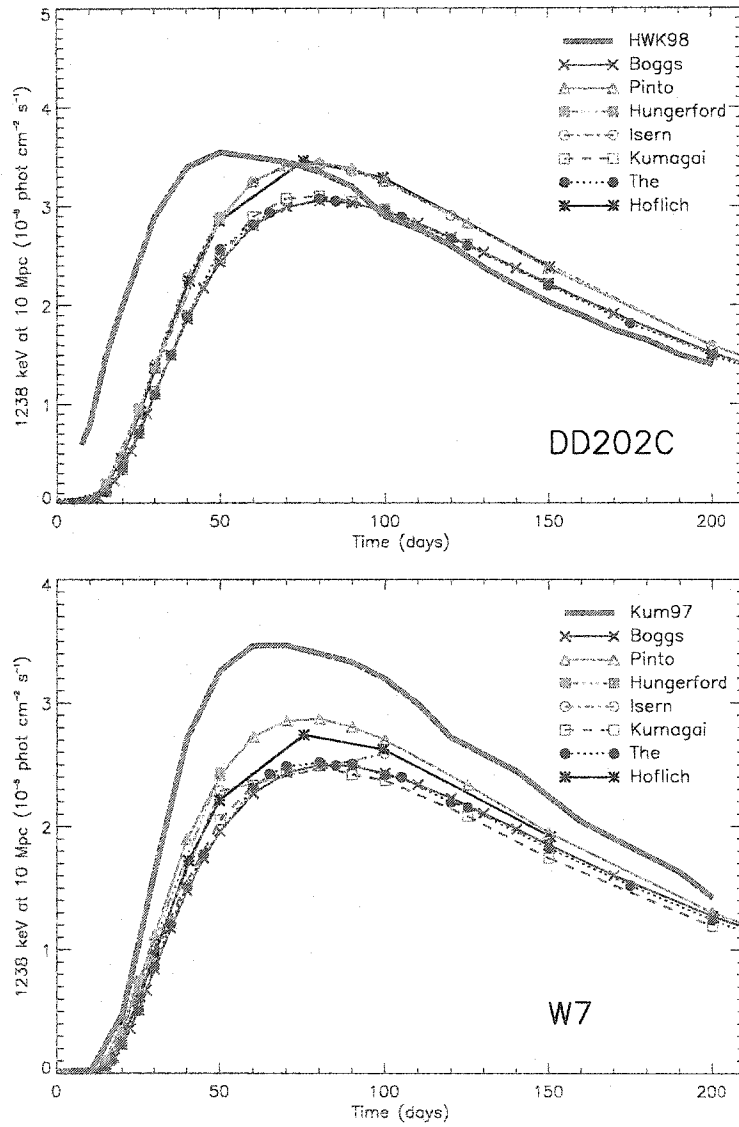


FIGURE 2.8. Line fluxes of the 1238 keV line for the SN models, DD202C and W7. The line fluxes extracted from the spectra (Höflich, Maverick, Fastgam, Isern) agree with the line fluxes that result from tagging line photons (The, Boggs, Kumagai). All current simulations predict fainter light curves than shown in previous published results (HWK98 for DD202C & HED6; Kumagai & Nomoto 1997 for W7). Spectral extraction assumed a 1150 - 1300 keV bandwidth. The HWK98 results are shown with and without the scaling for the escape fraction and branching ratios. Although the line definition in HWK98 differs from that used in this work, the light curves are similar when the corrections are applied.

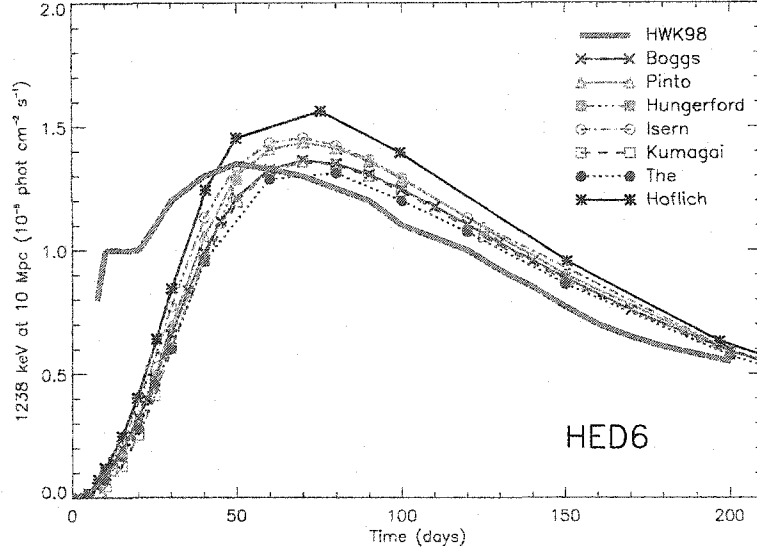


FIGURE 2.9. Line fluxes of the 1238 keV line as in the previous figure, for model HED6.

instrument that can resolve the spectra, these line profiles will provide a wonderful diagnostic of the nickel distribution. However, the line blending makes quantitative line flux comparisons between codes more difficult. Rather than try to isolate the individual contributions from each line based on the line profile, we have chosen to combine the two lines. Explicitly, we have defined the total flux to be all photons with energies between 810 - 885 keV (ignoring the fact that we include contamination from continuum emission). We assume equal escape fractions (a reasonable assumption for two lines very near in energy), and assign the individual line fluxes by the relative decay rates for each line (which are known at each epoch). For example, at 20 days the decay rate of  $^{56}\text{Ni} \rightarrow ^{56}\text{Co}$  decays is 1.83 times the decay rate of  $^{56}\text{Co} \rightarrow ^{56}\text{Fe}$  decays. Thus, we assign 65% of the total flux to the 812 keV line and 35% to the 847 keV line.

In Figures 2.10 through 2.2.3, we show the 847 keV and 812 keV line fluxes for the three models as simulated by all seven codes. Again for comparison, we include earlier light curves from HWK98 and Kumagai & Nomoto (1997). The deviation at

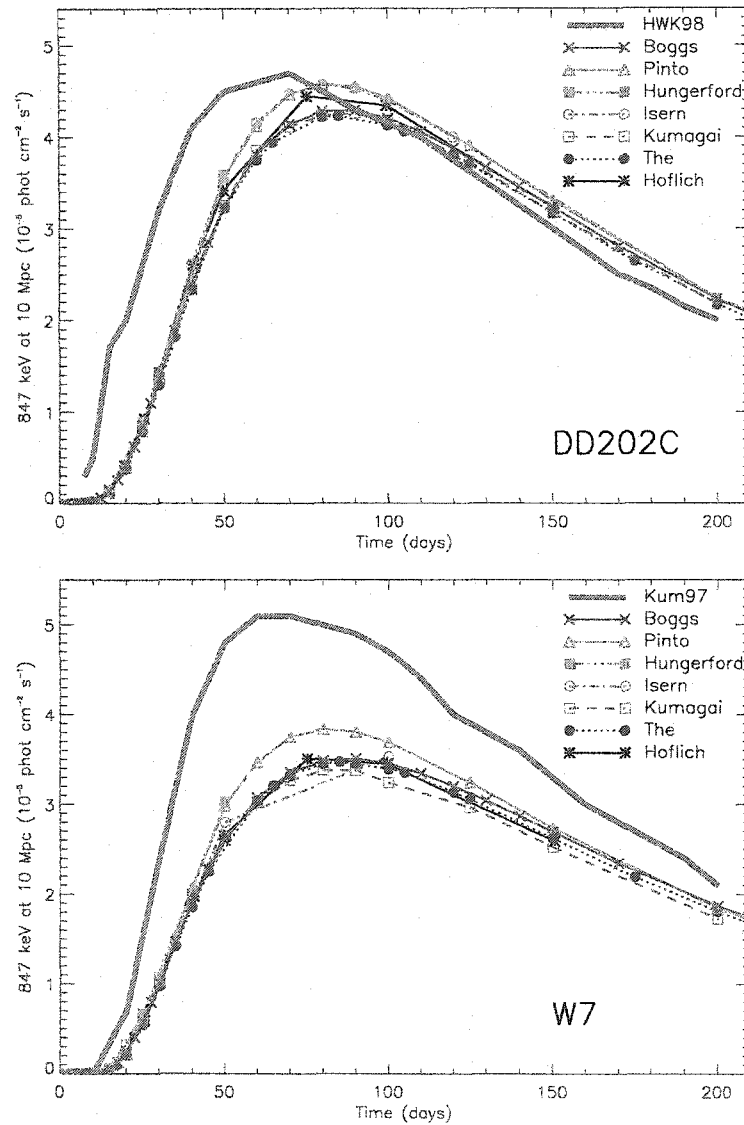


FIGURE 2.10. Line fluxes of the 847 keV line for the SN models DD202C and W7. Spectral extraction was more complicated for the 847 keV line than for the 1238 keV line (requiring the assumption that the 847 & 812 escape fractions are equal, and that all emission in the 790 - 900 keV energy band is line emission), but the light curves agree well with the light curves that result from tagging photons. Again, all current simulations suggest less line emission than suggested in HWK98 and Kumagai & Nomoto 1997. Also, the scaling for escape fraction and branching ratios brings the HWK98 light curves into rough agreement with the other light curves.



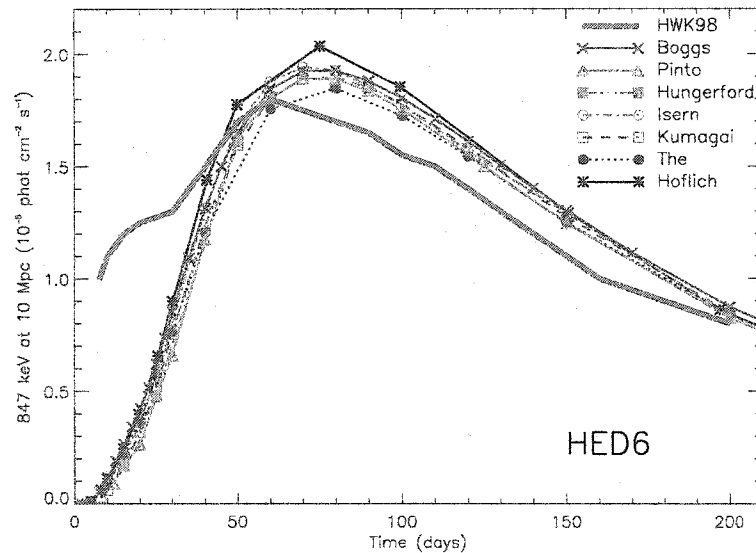


FIGURE 2.11. Line fluxes of the 847 keV line for the SN models as in the previous figure, for model HED6.

late times ( $> 25$  days) for the HWK98 812 keV light curve is consistent with the lower adopted branching ratio used in that code (see §2.1.2). As with the 1238 keV light curves, we find the same good agreement between the current code results.

#### 2.2.4 Summary of Comparisons

In light of the previous differences in simulated SN Ia  $\gamma$ -ray spectra, the agreement demonstrated in this comparison is strongly encouraging. The differences between the individual simulations are generally at the 10-20% level, much less than the differences that result from a range of input explosion models. This is particularly apparent in the nine panels of Figures 2.6 and 2.7. There would be no ambiguity as to which is the correct scenario if these three models were compared with actual observations of sufficient sensitivity. While this convergence is very reassuring for future theoretical work in this field, the disparity in previous versions of these codes have implications for past analysis work.

The most glaring code corrections were those needed to bring the over-luminous

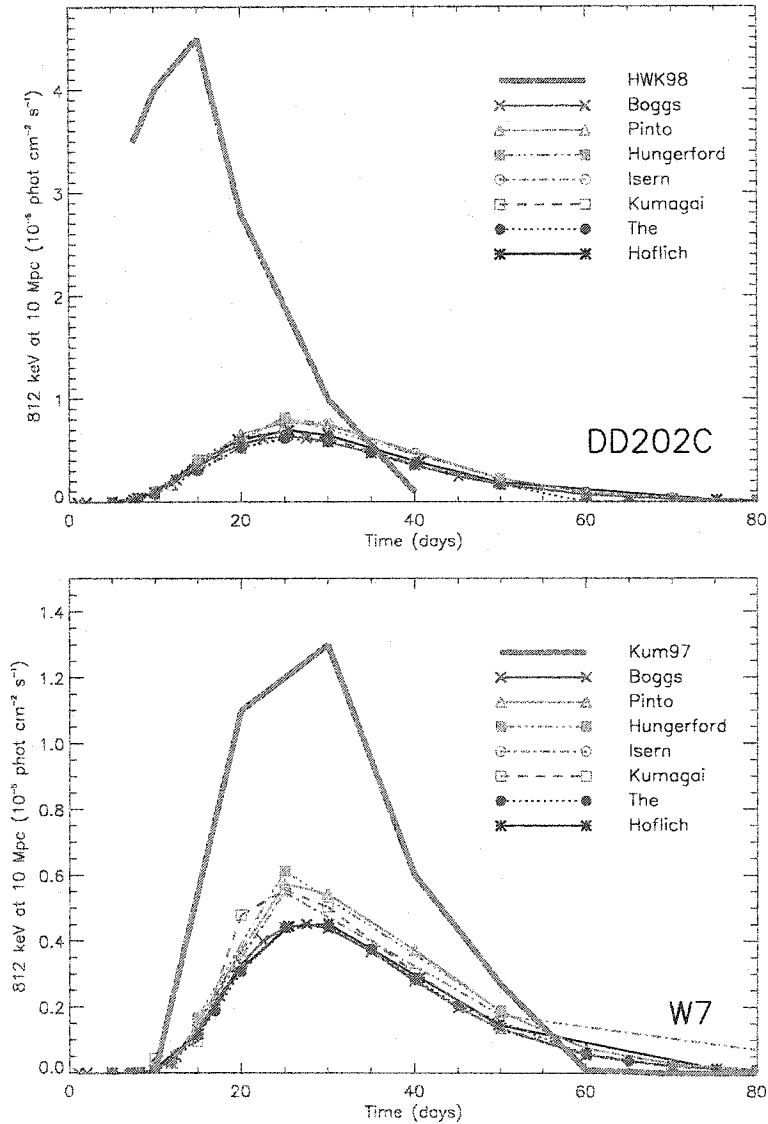


FIGURE 2.12. Line fluxes of the 812 keV line for the SN models DD202C and W7. As with the 812 keV line emission, the spectral extraction and tagging light curves agree, and are fainter than the HWK98 and Kumagai & Nomoto 1997 light curves. With the scaling for escape fraction and branching ratios, the HWK98 light curves agree fairly well with the other light curves. The HWK98 light curves after 20-30 days fall to zero, faster than the other light curves; this is due to the different definition for the 812 keV line employed in that work.

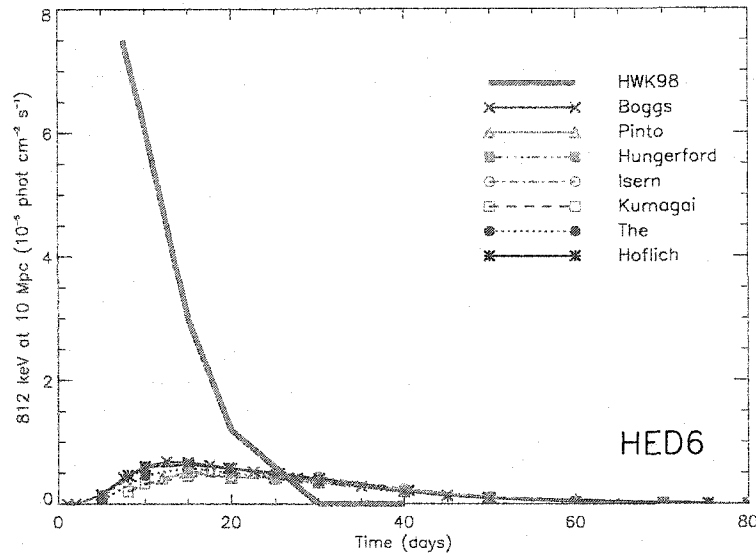


FIGURE 2.13. Line fluxes of the 812 keV line as in the previous figure, for model HED6.

line fluxes of Höflich and Kumagai into agreement with the more moderate values published by other groups. The high values published from the Kumagai code have been used to interpret the Compton Gamma-Ray Observatory COMPTEL observations of SN 1998bu, a “normally luminous” SN Ia, as determined from its optical lightcurve observations. The resulting analysis reached the conclusion that the set of “normally luminous” SN Ia progenitor models presented in Kumagai & Nomoto (1997) are all too bright at  $\gamma$ -ray line energies to explain the faint detection by the COMPTEL instrument. The work presented here verified that the published spectra from the Kumagai code agree well with the results in this comparison. However, their published lightcurves, on which the comparison with SN 1998bu was based, were derived from the spectra incorrectly and introduced an enhancement in the  $\gamma$ -ray line flux, driving them to inconsistently high fluxes as compared to the observations.

The emergent  $\gamma$ -ray emission from past publications using the Höflich code, to our knowledge, has not been used directly for the interpretation of any high energy SN Ia observations. In addition, the results of the HWK98 paper are unchanged by

the epoch dependent normalization error, as the emphasis of the paper was on the diagnostic potential of line profile shapes, rather than absolute line fluxes. However, the real concern, regarding the errors in the the Höflich code, arises not from the  $\gamma$ -rays that escape the ejecta, but rather the  $\gamma$ -rays that are absorbed, depositing their energy as heat in the ejecta. The energy deposition profiles resulting from such a calculation are used directly by lightcurve calculations (Höflich et al. 1992; Höflich et al. 1995, Höflich & Khokhlov 1996), which have, in turn, been used during the scientific planning phases of proposed space missions like the Supernova Acceleration Probe (SNAP; Perlmutter et al. 1999). These missions rely on theoretical estimates for the time evolution of the SN Ia lightcurves (assuming a wide range of progenitor and environment properties) in order to determine their required detection sensitivity. While a time dependent flux normalization would be most devastating to these predictions, the erratum for HWK98 (Höflich & Wheeler 2004) argues that this discrepancy was only present in HWK98 and affects none of their other published works. Still, the  $^{56}\text{Co}$  branching ratio error, and the yet unresolved difference in the efficiency of Compton down-scattering in energy will likely have repercussions for the lightcurve predictions of earlier works.

However, for the purposes of this thesis, the most important result is that Maverick has been verified against other implementations of the transport physics, and can be confidently applied to the investigation of core-collapse explosion asymmetries. A cautionary lesson to take away from this research is the necessity for cross-code comparisons. The  $\gamma$ -ray transport codes investigated here, while representing a truly multi-physics problem (nuclear decay processes, atomic absorption, angle- and energy-dependent electron scattering and special-relativistic material motion), they are significantly less complicated than the time-dependent radiation-hydrodynamics problems at the forefront of supernova simulations. Yet, the disparity between published works from these simulations not only exist, but have persisted for nearly a decade and gone unchecked until now. This should be unacceptable to the astro-

physics community at large.

### Chapter 3

#### GAMMA-RAY LINE EMISSION FROM BIPOLAR SUPERNOVAE

Having digressed into the details of numerical  $\gamma$ -ray transport, I recap briefly the motivation for the study of asymmetric supernovae. High energy observations of the two supernovae discussed in the introduction (SN 1987A and Cas A) argue for a closer inspection of the role a global asymmetry may play in the explosion mechanism. But the evidence for asymmetries in core-collapse supernovae goes well beyond that offered by the X- and  $\gamma$ -rays alone. Large optical polarization has been observed toward several core-collapse supernovae over the past decade (Leonard & Filippenko 2001; Wang et al. 2001). These observations show increasing polarization with time, suggesting that the explosion driving these supernovae is inherently asymmetric (Höfllich 1991). An equally compelling argument for global asymmetry arises from attempts to understand the high space velocities of neutron stars. The high observed velocities of pulsars and the formation scenarios of neutron star binaries both suggest that neutron stars are given strong kicks at birth. These kicks are most easily explained by some asymmetry in the supernova explosion (see Fryer, Burrows, & Benz 1998 for a review).

In fact, the most likely explanation for the polarization and neutron star kicks is that the explosion mechanism is intrinsically asymmetric. For instance, even if the collapsing star is initially spherically symmetric, some asymmetry can be produced due to convection taking place in, and above, the proto-neutron star (Herant et al. 1994; Burrows, Hayes, & Fryxell 1995; Janka & Müller 1996). To date, these asymmetries are not extreme enough in the theoretical models to explain observational evidence of compositional mixing. Larger asymmetries may occur if the collapsing star is asymmetric due to nuclear burning (Burrows & Hayes 1996; Lai 2000; Bazan & Arnett

1998), however, sufficiently large departures from spherical symmetry have only been produced in models by assuming extremely asymmetric collapsing cores (Burrows & Hayes 1996). Alternatively, rotation can produce significant asymmetries in the supernova explosion (Mönchmeyer & Müller 1989; Janka & Mönchmeyer 1989; Fryer & Heger 2000, Khokhlov et al. 1999). The nature of these asymmetries depends upon the angular momentum profile of the collapsing star and, although most calculations predict jet-like explosions along the rotation axis, some calculations imply that an equatorial explosion could occur (Mönchmeyer & Müller 1989).

In contrast to the jet driven asymmetric explosions proposed by Khokhlov et al. (1999), the explosion asymmetries which result from rotation are relatively mild (velocity axis ratio of order 2:1 at roughly 2 seconds after bounce; Fryer & Heger 2000). In this section, we discuss results from 3-dimensional supernova simulations (Hungerford et al. 2003) investigating explosions with the mild asymmetries implied by rotating core-collapse models.

### 3.1 Explosion Simulations

In the hydrodynamic simulations described below, we employed the  $15 M_{\odot}$  progenitor (s15s7b2) by Weaver & Woosley (1993). This star was evolved with a piston-driven explosion to 100 s after bounce, producing  $0.24 M_{\odot}$  of  $^{56}\text{Ni}$ . The total energy of this model was roughly  $1.5 \times 10^{51}$  erg with roughly  $1.0 \times 10^{51}$  erg in kinetic energy. As the explosion moves through the progenitor star, the shock passes through composition boundaries where strong entropy gradients exist. When the shock hits these boundaries, Rayleigh-Taylor (or Richtmyer-Meshkov) instabilities develop, causing the star to mix (Chevalier & Klein 1978; Weaver & Woosley 1980). Pre-existing structure at these boundaries, due for example to explosive oxygen and silicon flashes (Bazan & Arnett 1998), could serve to enhance this mixing. Our simulations have modeled this mixing and concentrated on the effects that asymmetries have on it. However, the

computational hydrodynamic technique employed (smooth particle hydrodynamics) possesses perturbations which compare closely to seed structures in the oxygen and silicon shells.

### 3.1.1 Numerical Schemes

The simulations presented here (Table 3.1.1) have been calculated using a three-dimensional smooth particle hydrodynamics code (see Warren et al. 2004, in preparation, for details) based on the parallel oct-tree algorithm developed by Warren & Salmon (1993). This lagrangian code tracks the composition exactly. For 2 of our simulations, we included the energy injection from  $^{56}\text{Ni}$  and  $^{56}\text{Co}$  decay (and hence also trace the abundances of  $^{56}\text{Co}$  and  $^{56}\text{Fe}$ ). For these 2 models, we assume that all of the decay energy is injected into the gas. At late times, this will overestimate the total energy deposited, as a fraction of this energy will escape, but since we would like an upper limit on the effects of  $^{56}\text{Ni}$  decay, and because the injection of energy is less important to the explosion dynamics at late times, this assumption is adequate. For decay energy, we assume that the total energy from decay is  $9.3 \times 10^{16} \text{ erg g}^{-1}$  with 33% being released from  $^{56}\text{Ni}$  decay with a 6.1 d half-life and the other 67% being released from  $^{56}\text{Co}$  decay with a 77 d half-life (Colgate, Petschek, & Kriese 1980). This is similar to what Herant & Benz (1992) and Herant & Woosley (1994) used for their models. For an equation of state, we use the same “low-density” equation of state developed by Blinnikov, Dunina-Barkovskaya, & Nadyozhin (1996) that is used in our progenitor model.

We mapped the Weaver & Woosley (1993) model with its 100 s long, spherically symmetric explosion into our 3D SPH code with 2.2 million variably-massed particles. The mapping at 100 s is done for two primary reasons. The first is computational expediency: for the purposes of understanding the effect asymmetry has on the hydrodynamic mixing structures, we need not model the complicated (and time consuming)



Model	$\frac{V_{\text{pole}}}{V_{\text{eq}}}$	$\alpha, \beta$	K.E. <i>Initial</i> ( $10^{51}$ ergs)	T.E. <i>Initial</i> ( $10^{51}$ ergs)	K.E. <i>final</i> ( $10^{51}$ ergs)	Mixing ( $M_{\odot}$ )
Sym	1.0	1,0	1.0	0.51	1.3	4.6
Sym D	1.0	1,0	1.0	0.51	1.3	5.5
Jet2	2.0	$\sqrt{3/7}, \sqrt{3/7}$	1.0	0.51	1.3	5.6
Jet2 D	2.0	$\sqrt{3/7}, \sqrt{3/7}$	1.0	0.51	1.3	5.7
Jet4	4.0	$\sqrt{1/7}, \sqrt{9/7}$	1.0	0.51	1.3	8.0
Eq2	0.5	4/3, 2/3	1.0	0.51	1.3	5.0
Eq4	0.25	8/5, 6/5	1.2	0.51	1.6	11.3

TABLE 3.1. Explosion simulation parameters.

phase of core-collapse and bounce. The second reason is that the SPH code we use does not yet include a nuclear burning network with which to compute the explosive nucleosynthetic yields. Thus, we take the model at 100s after explosive nuclear reactions have frozen out, and then follow the 3-dimensional spatial evolution of the 1-dimensionally determined nuclear yields. We model the entire sphere, so there are no axis boundaries in this simulation and the neutron star mass at the center is added through an external gravitational force. Asymmetries are added artificially to the velocities only and, for most of the explosions, are added in such a way to insure that the total kinetic energy of the explosion is conserved. The two asymmetries we model are jet explosions:

$$v_{\text{radial}} = (\alpha + \beta \times |z|/r) v_{\text{radial}}^{\text{sym}} \quad (3.1)$$

and equatorial explosions:

$$v_{\text{radial}} = (\alpha - \beta \times |x|/r) v_{\text{radial}}^{\text{sym}} \quad (3.2)$$

where  $v_{\text{radial}}^{\text{sym}}$  is the velocity from the one dimensional calculation,  $v_{\text{radial}}$  is the radial velocity for the asymmetric setup, and  $x, z, r$  are the x-position, z-position, and radius of the particle. The values of  $\alpha$  and  $\beta$  for each model are given in Table 3.1.1, along with the initial kinetic energy of each model. The magnitude of the

asymmetries are guided by the results of Fryer & Heger (2000), who found that their rotating core-collapse simulations in 2-dimensions had velocities that were a factor of 2 higher in the pole than in the equator 1.5s after bounce. We do not use the extreme asymmetric explosions of Khokhlov et al. (1999) which concentrate the explosion energy into a narrow jet. As we shall show (and as Nagataki 2000 argued), such extreme asymmetries are not required to explain outward mixing of nickel in supernovae. Although at the end of the Fryer & Heger simulation, the asymmetry in polar vs. equatorial velocities is growing, the trend as the shock moves outward will be to spherize the shock. So at this point, it is not clear whether the shock at 100s will be more or less asymmetric than what Fryer & Heger (2000) found at the end of their simulation.

After mapping these models into our 3-dimensional SPH code, we then run the explosion out to 1 year. When the shock reaches the edge of the star, we assume it is moving through a vacuum. In reality, such a star will have a stellar wind atmosphere surrounding it, but the density of a  $15 M_{\odot}$  wind is so low, that for the purposes of our simulation, zero density material is appropriate. In addition, photon transport is not modeled in our calculations. However, prior to shock breakout, the photons are essentially trapped in the shock. By the time the shock breaks out, most of the internal energy has already been converted to kinetic energy, so although including photon transport will change the ionization state of the exploding stellar material, it does not affect the kinematics significantly.

The smoothed particle hydrodynamics technique automatically adds a level of perturbation in the code. With our initial conditions, these perturbations are random with a maximum  $1 \sigma$  deviation in a shell of 5-7%. Such large deviations only occur at composition boundaries, specifically the silicon and oxygen shells, and match well the deviations arising from explosive oxygen and silicon flashes prior to collapse (e.g. Bazan & Arnett 1998).

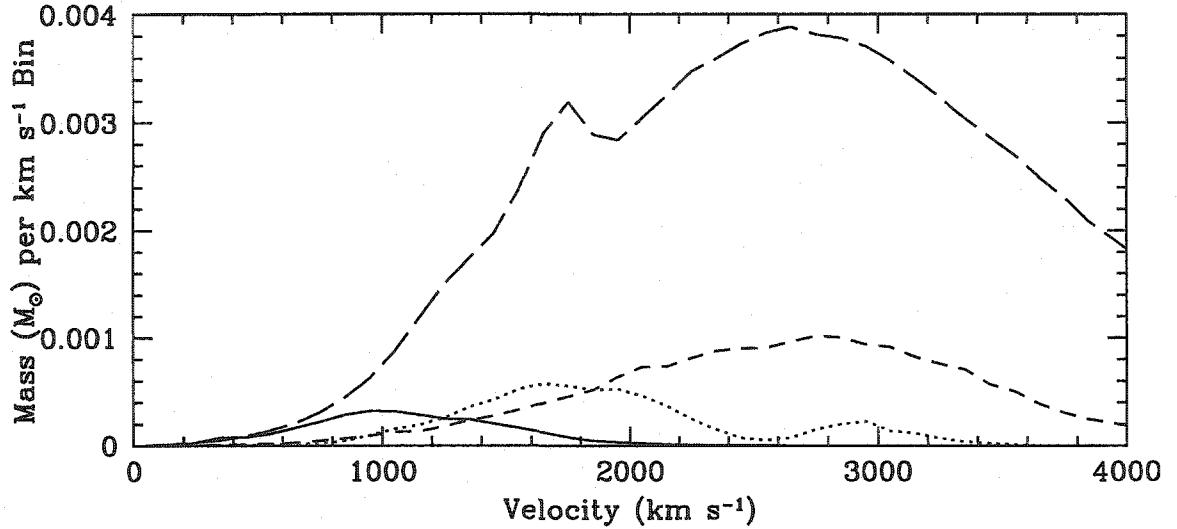


FIGURE 3.1. Velocity distribution of nickel (solid), Oxygen (dotted), Helium (dashed), and Hydrogen (long dashed) in our 3-dimensional simulations. Comparing these distributions to the 2-dimensional simulations in Fig. 1 of Herant & Woosley (1994), we note that the distribution of elements is similar in both the 2- and 3-dimensional simulations. However, the stronger 3-dimensional explosion causes all of the ejecta to be moving slightly faster than that of the 2-dimensional simulation and it is difficult to compare mixing instabilities.

### 3.1.2 Explosion and Nickel Distribution

Although we use the same  $15 M_{\odot}$  progenitor that was used by Herant & Woosley (1994), it has a higher explosion energy and we map this model onto our 3-dimensional grid 200s earlier than Herant & Woosley (1994) mapped their spherically-symmetric explosion simulation onto a 2-dimensional grid. Therefore, although their study has the closest similarities with our work, it is difficult to make direct comparisons to their simulations. Nevertheless, it is interesting to compare the velocity distribution of each chemical element from our 3-dimensional simulations with the 2-dimensional simulations of Herant & Woosley (1994) at 90 days (compare the lower right panel in Figure 1 of Herant & Woosley 1994 with Figure 3.1 in this paper). In Figure 3.1, the material labeled “hydrogen” includes all material in the hydrogen envelope (as did Herant & Woosley 1994). Similarly, by “nickel” we refer to both the distribution of

nickel as well as its decay products (most notably  $^{56}\text{Co}$ ). Although the distribution of elements is similar in both the 2 and 3 dimensional simulations, the stronger 3-dimensional explosion causes all of the ejecta to be moving slightly faster than that of the 2-dimensional simulation and it is difficult to compare mixing instabilities.

Comparing the structure of the convective instabilities themselves is also difficult. In 3-dimensions, the “mushroom”-like structures formed by Rayleigh-Taylor instabilities are not so well defined, and don’t lie along any one plane. However, 4.3 hours into the explosion, it is clear that instabilities have developed (Figure 3.2) and these instabilities ultimately mix nickel knots far out into the star (Figure 3.3). At the start of the explosion,  $^{56}\text{Ni}$  is found only in the inner  $1.6 M_{\odot}$  of the star ( $1.3 M_{\odot}$  becomes the neutron star, so the nickel is limited to the inner  $0.3 M_{\odot}$  of ejecta). By the end of the simulation,  $^{56}\text{Ni}$  has mixed out nearly to  $5 M_{\odot}$ , beyond the  $\sim 4.5 M_{\odot}$  boundary that marked the edge of the helium layer (Figure 3.4). Unfortunately, this mixing is, if anything, less than the amount of mixing found in the 2-dimensional simulations of Herant & Woosley (1994). The fact that the mixing is less in 3-dimensions vs. 2-dimensions could be due to the lower effective resolution, which cannot include the smallest spatial scales (we only have 2.2 million particles in 3-dimensions vs. 25,000 particles in the 2-dimensional simulations)<sup>1</sup>. One should note, however, that turbulence behaves differently in 2 and 3 dimensions. In two dimensions, an inverse cascade drives energy from small to large scales, while in three dimensions energy is transported from large to small scales and dissipated. It is likely that these differences cause the 2-dimensional simulations to produce more extensive mixing. In any event, it appears that neither our spherical 3-dimensional simulations nor the 2-dimensional simulations seem to give enough mixing to explain the observations of supernovae like SN 1987A.

---

<sup>1</sup>Note that the 2-dimensional simulations of Herant & Woosley (1994) have poor mass resolution and low resolution could be a problem in the 2-dimensional simulations as well as the 3-dimensional simulations

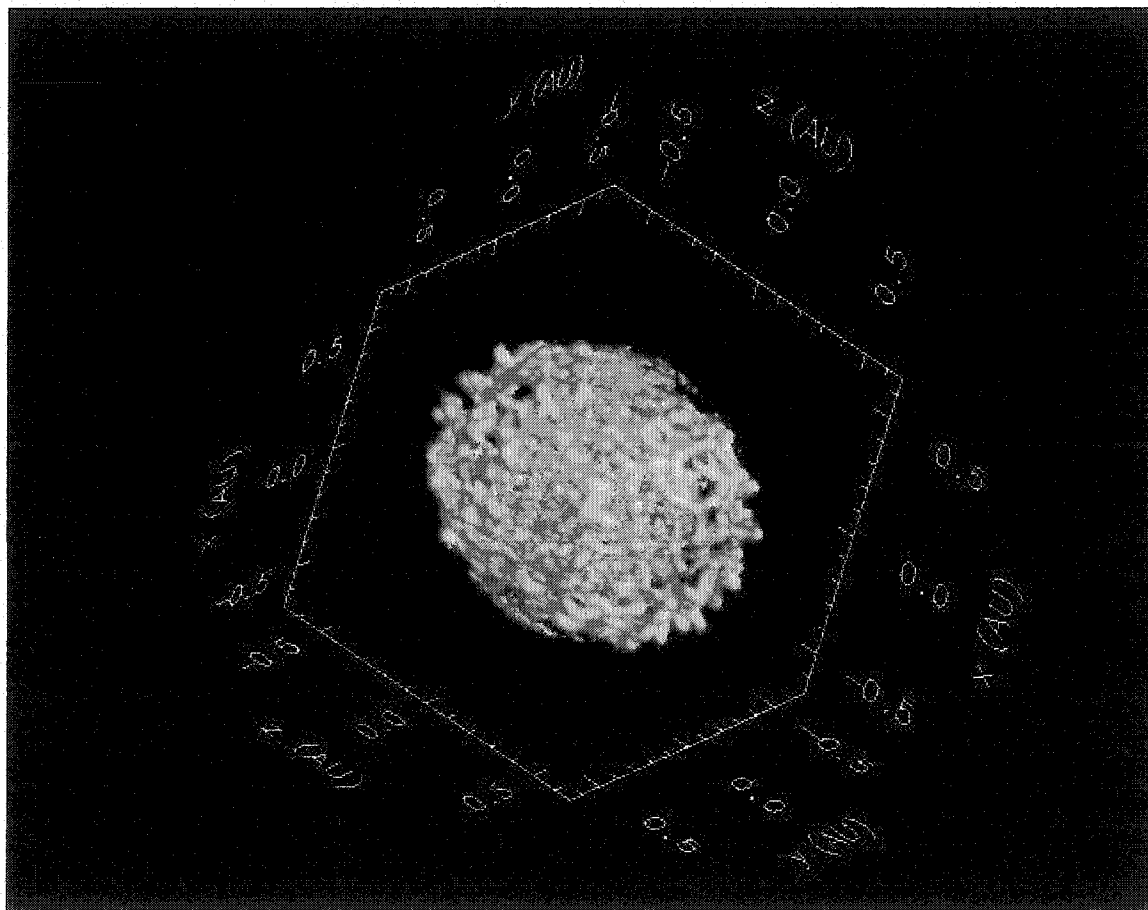


FIGURE 3.2. Density contour ( $7 \times 10^{-5} \text{ g cm}^{-3}$ ) plot of the early stages of the convection, 4.3 hours after the launch of the explosion. Notice that tendrils mixing out the material have already developed. It is this mixing that places nickel far beyond its initial distribution.

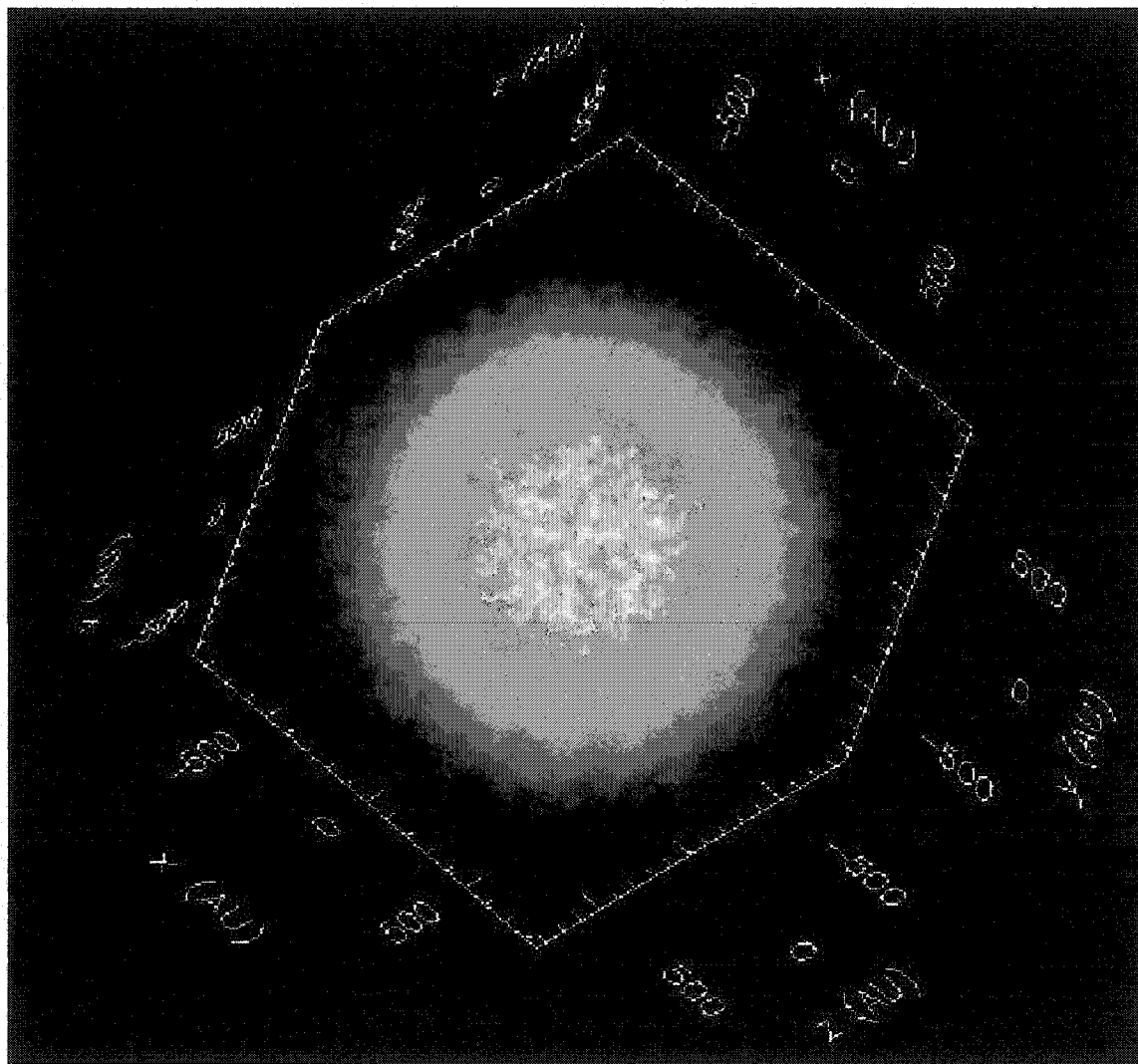


FIGURE 3.3. 3-dimensional simulation of the symmetric explosion 1 year after the shock launch. The contours represent the cobalt distribution with a number density of  $10^{-5}$ . The colors denote the density distribution. Note that although the explosion is symmetric, Rayleigh-Taylor instabilities mix out the nickel.

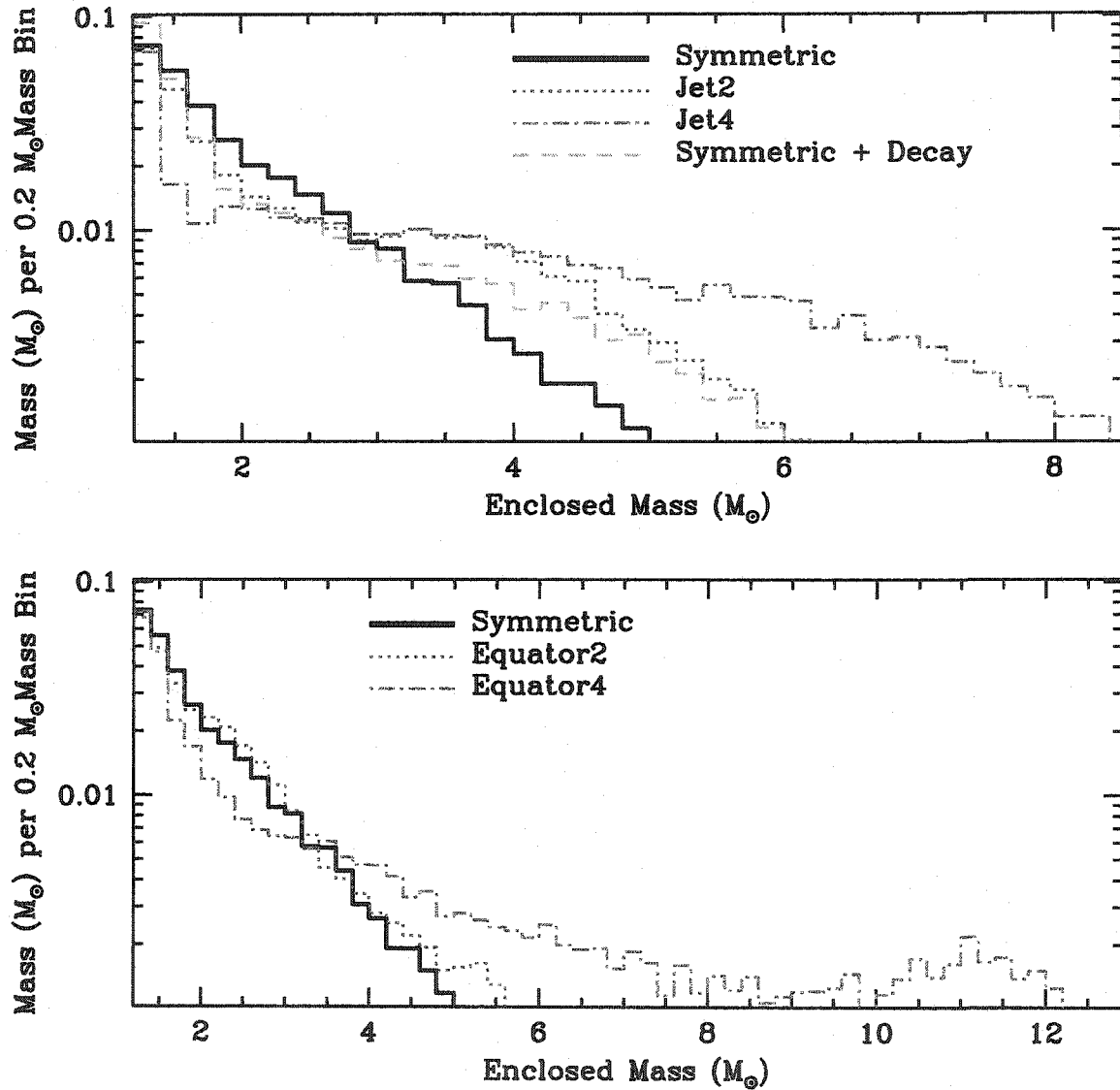


FIGURE 3.4. Distribution of the nickel ejecta in mass, comparing jet explosions with a symmetric explosion (top panel) and equatorial explosions with a symmetric explosion (bottom panel). Note that as we increase the degree of asymmetry (Jet4 versus Jet2, Equator4 versus Equator2), the mixing increases dramatically, placing nickel well into the hydrogen envelope of the star. The dashed line (top panel) shows the extent of mixing if all of the nickel/cobalt decay energy is deposited into the nickel ejecta and produces almost as much mixing in a symmetric explosion as the Jet2 model.

Nagataki et al. (1998a) and Nagataki (2000) found that they required mild asymmetries ( $v_{\text{Pole}}/v_{\text{Equator}} = 2$ ) to explain SN 1987A. Since we model a  $15 M_{\odot}$  star, not a SN 1987A progenitor, it is difficult to both compare with this past work as well as constrain our results with observations of SN 1987A. But we can discuss the basic trends caused by asymmetries. Figure 3.5 shows model Jet2 1 year after explosion. Note that although the density distribution has spherized as the shock propagates through the shallow density gradients of the red supergiant envelope (Chevalier & Soker 1989), the distribution of  $^{56}\text{Co}$  (the decay product of  $^{56}\text{Ni}$ ) retains a large asymmetry. We discuss the effects of these asymmetries on the  $\gamma$ -ray emission in §3.2.

Like Nagataki et al. (1998a) and Nagataki (2000), we find that the asymmetries broaden the velocity profile of  $^{56}\text{Ni}$  (Figure 3.6). However, in our simulations, mild asymmetries ( $v_{\text{Pole}}/v_{\text{Equator}} = 2$ ) led to only a small increase in the maximum nickel velocity from  $2500 \text{ km s}^{-1}$  to  $2900 \text{ km s}^{-1}$ . For Nagataki et al. (1998a), such mild asymmetries increase the maximum nickel velocity from  $2200 \text{ km/s}$  to  $3200 \text{ km/s}$ ! This difference could be progenitor dependent, an effect of 3-dimensional vs. 2-dimensional convection, or the lack of resolution in our 3-dimensional models. Extracting the true cause of this difference awaits future calculations with similar initial conditions.

However, increasing the amount of asymmetry by another factor of 2 (Models Jet4, Eq4) causes some nickel to be ejected at very high velocities. The amount of mixing in these cases reaches extremes with the nickel well into the hydrogen envelope. Such mixing has decided signatures in both the emergence of the  $\gamma$ -ray line flux and the shape of the  $\gamma$ -ray lines (§3.2). Note that the energy released from the decay of nickel also helps to mix out the nickel (on par with the effects of mild asymmetries). Clearly, the energy released from the decay of nickel cannot be neglected in any accurate mixing calculation.

This mixing also has important repercussions for nucleosynthetic yields and the mass-cut for the remnant mass. Most black holes are formed in stars which produce supernova explosions that are too weak to throw off all of the stellar envelope and the



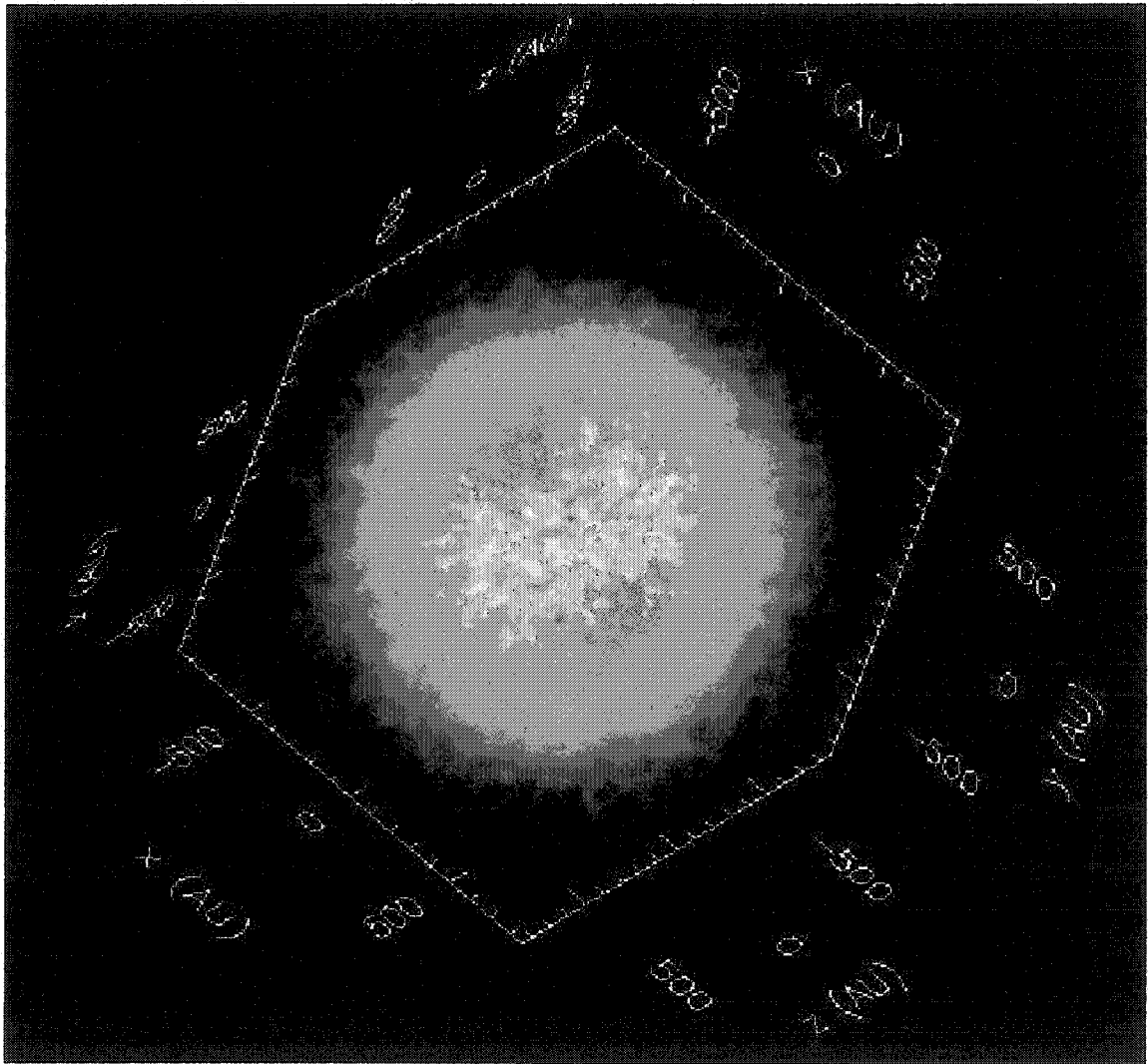


FIGURE 3.5. 3-dimensional simulation of the Jet2 asymmetric explosion 1 year after shock launch. As in Fig. 3, the contours represent the cobalt distribution with a number density of  $10^{-5}$ . The colors denote the density distribution. The nickel is mixed out extensively in the polar direction where the explosion was strongest. However, the density distribution did not gain large asymmetries and remained fairly symmetric.

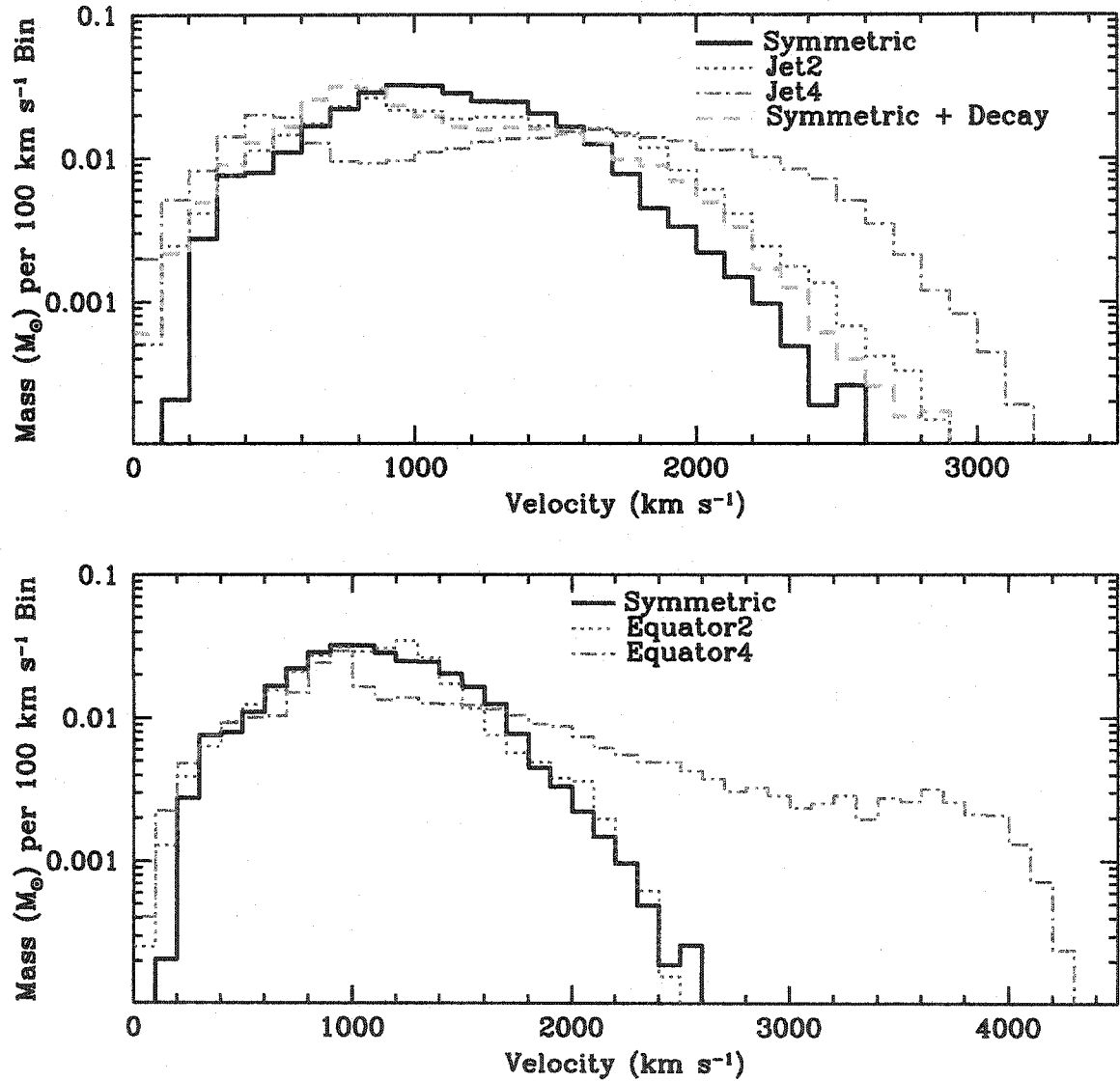


FIGURE 3.6. Distribution of the nickel ejecta versus velocity comparing jet explosions with a symmetric explosion (top panel) and equatorial explosions with a symmetric explosion (bottom panel). Note that as we increase the degree of asymmetry (Jet4 versus Jet2, Equator4 versus Equator2), the mixing increases dramatically, producing nickel velocities in excess of 3000 km/s. The dashed line (top panel) shows the velocities achieved if all of the nickel/cobalt decay energy is deposited into the nickel ejecta and produces almost as much mixing in a symmetric explosion as the Jet2 model.

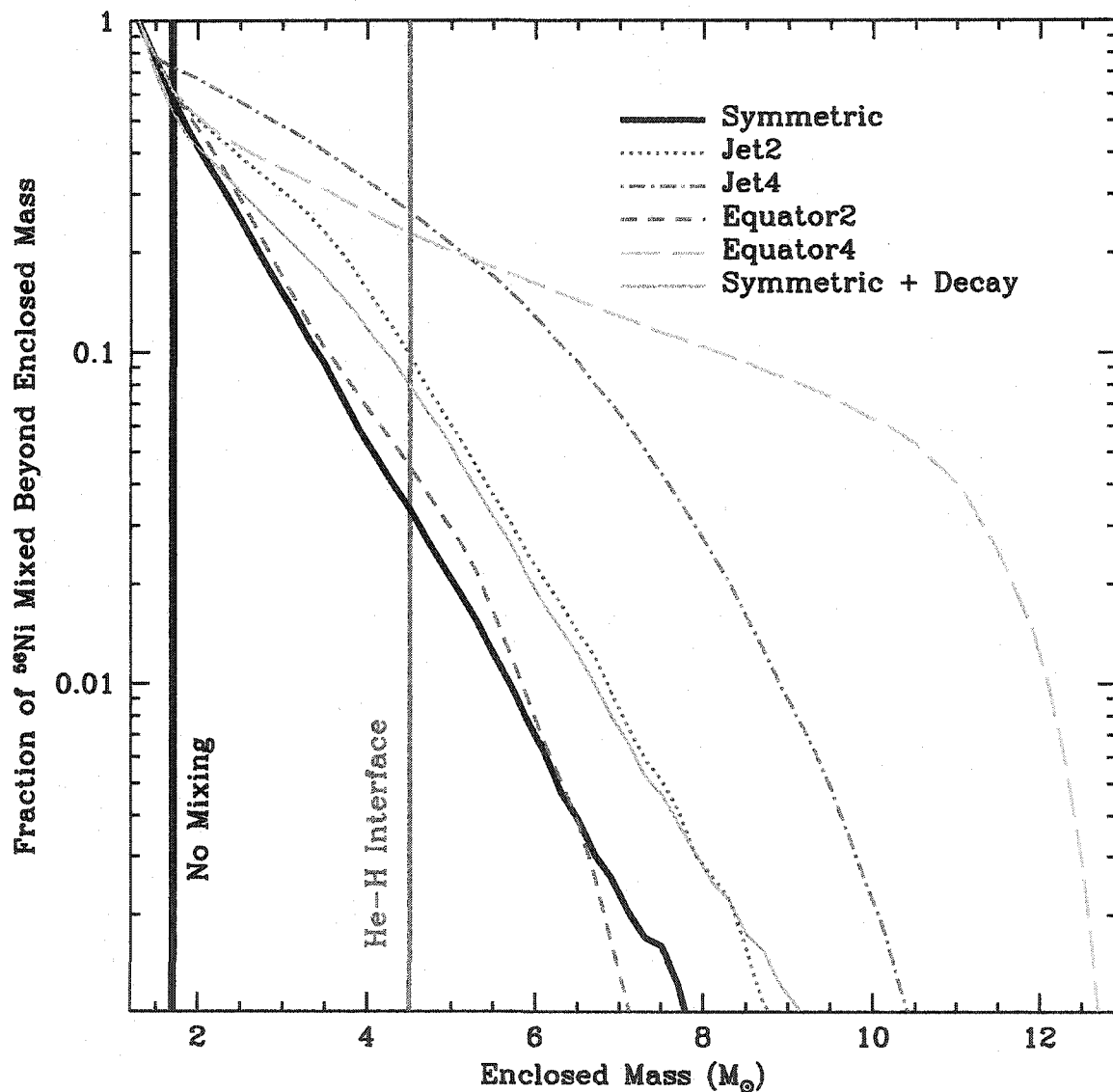


FIGURE 3.7. Fraction of nickel ejecta mixed out into the star for our set of simulations. Note that for mild asymmetries (Jet2) or if decay energy is included in a symmetric explosion (Symmetric+Decay), nearly 10% of the nickel mass is injected into the hydrogen envelope. If this amount of mixing occurs in weak explosions, an explosion that resulted in a  $4.5 M_{\odot}$  black hole remnant would still eject a moderate amount of nickel.

subsequent fallback produces a black hole (Fryer & Kalogera 2001). In our models (Jet2, Sym+Decay, etc.), more than 10% of the nickel produced is ejected well beyond the helium core (Figure 3.7). If this trend holds for more massive stars such as the progenitor of SN 1997D (Turatto et al. 1998), then the entire helium core of such a star ( $>8 M_{\odot}$ ) could fall back and still enough nickel would escape to power the observed light curve! Bear in mind, however, that weaker explosions may well produce less mixing, so adapting the results of our simulations to supernovae like 1997D must be taken with some caution.

### 3.2 High Energy Spectral Calculations

For the spectral calculations, we have used data from the 3-dimensional explosion simulation discussed in the above section. We input ejecta material properties from five different snapshots in time at 150, 200, 250, 300 and 365 days after explosion. Spectral calculations were carried out for both the Jet2 and Symmetric explosion models. Our analysis of these model spectra concentrates on the differences in total luminosity and line profile shape with the introduction of realistic explosion asymmetries. Since the progenitor star used as input to our simulations was a  $15 M_{\odot}$  red supergiant, we are unable to directly compare our calculated spectra with the observations of SN 1987A mentioned in the introduction. However, we discuss how our models compare to various spectral trends observed from SN 1987A.

#### 3.2.1 Numerical Schemes

The general framework for a Monte Carlo transport code was already discussed in the previous chapter, so I will only briefly describe the specific assumptions made for this project in the context of that framework.

Our input models of the supernova ejecta (element abundances, density and velocities) were taken from the Jet2 and Symmetric SPH explosion simulations described

above and mapped onto a  $140 \times 140 \times 140$  Cartesian grid. Escaping photons were tallied into 250 coarse energy bins, with finer binning at the decay line energies to provide line profile information. The emergent photons were also tallied into 11 angular bins ( $\Delta\theta = 10^\circ$ ) along the polar axis (the models investigated in this work are axisymmetric, alleviating the need to tally in azimuthal angle as well).

The decay of the radioactive species (predominantly  $^{56}\text{Ni}$  and its decay product  $^{56}\text{Co}$ ) in the supernova ejecta gives rise to the  $\gamma$ -ray line emission. Decay probabilities were taken from Browne, Dairiki, & Doebler (1978) for the various radioactive species ( $^{56}\text{Ni}$ ,  $^{56}\text{Co}$ ,  $^{57}\text{Co}$ ,  $^{44}\text{Ti}$ ,  $^{44}\text{Sc}$ , and  $^{22}\text{Na}$ ). We include a total of 56 decay lines from these species, but for the explosion times considered, the packets fall predominantly into 15 decay lines. Roughly  $10^9$  Monte Carlo photon bundles were generated for each input model, in proportion to the mass of radioactive material distributed throughout the ejecta. The material properties of the ejecta were not evolved with photon flight time. However, we found that 99% of the photons contributing to the observed model spectra have escape times of less than 2 days. This is sufficiently shorter than the timescales for change in the hydrodynamic models that our assumption of a fixed material background should be valid for the time slices considered here. The opacities seen by the packet were calculated in the comoving frame of the fluid, but all photon properties were boosted to the observer's frame before being tallied into spectral observables.

In all models, photoelectric and pair production opacities were calculated for the elements H, He, C, N, O, Ne, Mg, Si, S, Ar, Ca, Ti, Cr, Fe, Co, and Ni, which correspond to the elements used in the nucleosynthesis calculations for the progenitor star from Weaver & Woosley (1993). The cross section data for these elements were taken from the LLNL Evaluated Nuclear Data Library (Plechaty, Cullen, & Howerton 1981). The angle- and energy-dependent Compton scattering opacities were calculated assuming that all electrons, bound and free, contribute to the total cross section. Daughter products from the absorption processes were not followed (e.g.,

positron annihilation photons from pair production and K-shell fluorescence photons from photoelectric absorption). In order to test the validity of this last approximation, we compared the results from Maverick with the one-dimensional code FASTGAM (Pinto & Woosley 1988a). Good agreement was found between the model spectra whether the daughter products of absorption were included in FASTGAM or not. This justified the decision to disregard the fluorescence and annihilation photons in Maverick.

### 3.2.2 Hard X-ray and Gamma-ray Spectrum

Figure 3.8 is a logarithmic plot of photon flux in units of photons/second/MeV/cm<sup>2</sup> across the energy range investigated with these simulations (0.3 keV - 4 MeV). We have placed this object at the distance of the Large Magellanic Cloud (60 kpc) for easy comparison with flux data from SN 1987A observations. The 5 panels are spectra from the different time slices; in each panel, we plot the spectrum for the Symmetric model, along with polar and equatorial views of the Jet2 model. The effects of mixing are present in both these simulations, though at differing levels due to the differences in explosion asymmetry. It can be seen immediately that the hard X-rays emerge earlier from the ejecta with a global explosion asymmetry (Jet2 model). This holds regardless of viewing angle (pole versus equator) towards the explosion.

The fact that the hard X-ray flux in the aspherical explosion model is larger than the symmetric explosion, regardless of line of sight, can be understood in principle from optical depth arguments. In Figure 3.9, we show a contour plot of density (outer contour) and <sup>56</sup>Co number density (inner contour) for the Jet2 and Symmetric models at  $t = 150$  days. Decay of <sup>56</sup>Co is the major source of  $\gamma$ -ray photons, so the inner contour essentially traces the surface of the emission region. The horizontal and vertical lines in Figure 3.9 represent lines of sight from the ejecta surface to the emission source and are labeled with the optical depth along that line of sight. The

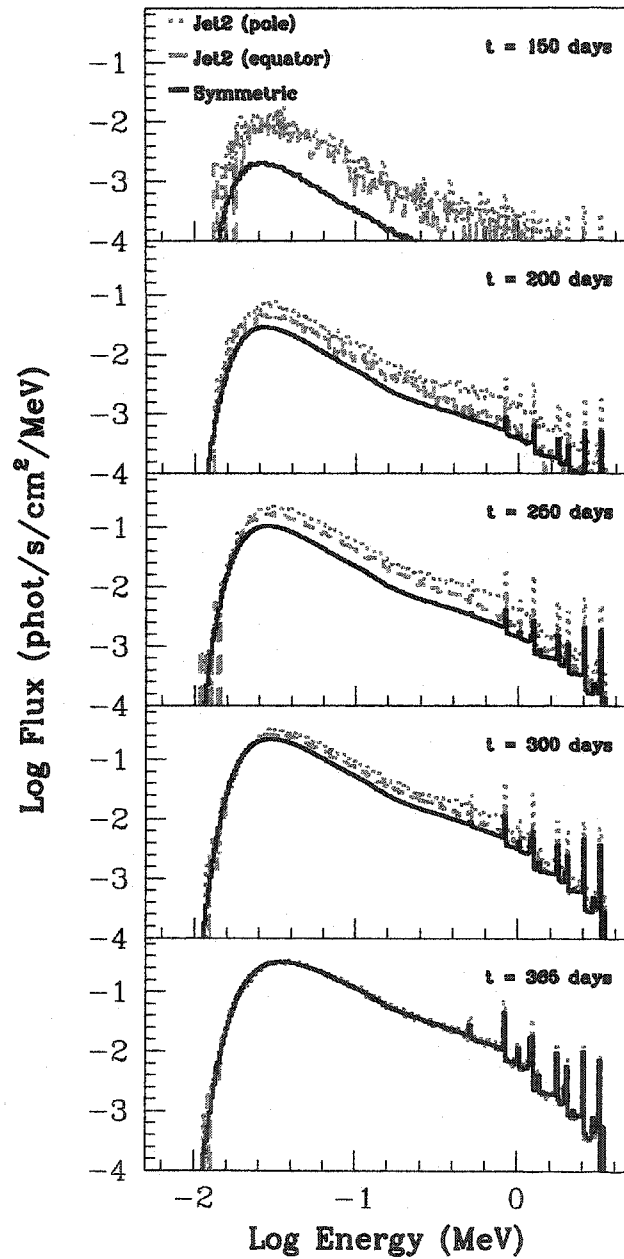


FIGURE 3.8. Total hard X- and  $\gamma$ -ray spectrum at 5 different times during the explosion (150,200,250,300,365 days) for symmetric (solid lines) and aspherical (Jet2) explosions (dotted and dashed lines). The flux is determined by assuming the object is 60 kpc from the observer. The dotted lines refer to an aspherical explosion where the jet is directed along the line of sight of the observer. The dashed lines refer to an explosion where the observer line of sight is directed  $90^\circ$  off of the jet axis, in the equatorial direction. Regardless of observer viewing angle, the aspherical explosion is brighter than the Symmetric explosion.

dominant opacity for the hard X- and  $\gamma$ -rays is Compton scattering off electrons and, since the density contours remain roughly spherical in both models, the optical depth from a given point to the ejecta surface is roughly constant. In the Jet2 model, the  $^{56}\text{Ni}$  was mixed out to larger radii in the polar direction, so it makes perfect sense that we see enhanced emission over the Symmetric model spectrum for that viewing angle (the optical depth that the high energy photons must pass through is 10 in the symmetric model versus  $\sim 6 - 7$  along the polar line of sight in the Jet2 model).

At a first glance, one might expect that, in the Jet2 explosion along the equatorial line of sight, the total flux should also be low (the optical depth from the nickel in the equator is also roughly 10). However, this material does not dominate the high energy emission seen along the equatorial line of sight. The material ejected along the poles has been mixed far enough out in the ejecta that the optical depth these high energy photons must travel through, even along the equatorial line of sight, is quite low ( $\sim 7$ ). It is this nickel which dominates the hard X-ray emission at all viewing angles. In fact, the optical depth from the “ends” of the  $^{56}\text{Co}$  distribution does not differ very much between the polar view and the equator view ( $\tau = 6$  &  $7$  respectively), which explains why the overall hard X-ray flux depends only mildly on viewing angle.

For the later time slices, this mismatch in escape probability from the “ends” versus the equatorial plane ejecta is less pronounced, and the equator view spectrum has comparable contributions from both regions.

### 3.2.3 Gamma-ray Line Profiles

Although the overall hard X-ray emission shows little variation between pole and equator views, a detailed look at the  $\gamma$ -ray line profile shapes and strengths, for the 1.238 and 0.847 MeV  $^{56}\text{Co}$  lines, does reveal trends with viewing angle. Figures 3.10 and 3.2.3 show line profiles of these two  $^{56}\text{Co}$  lines for both the Symmetric and



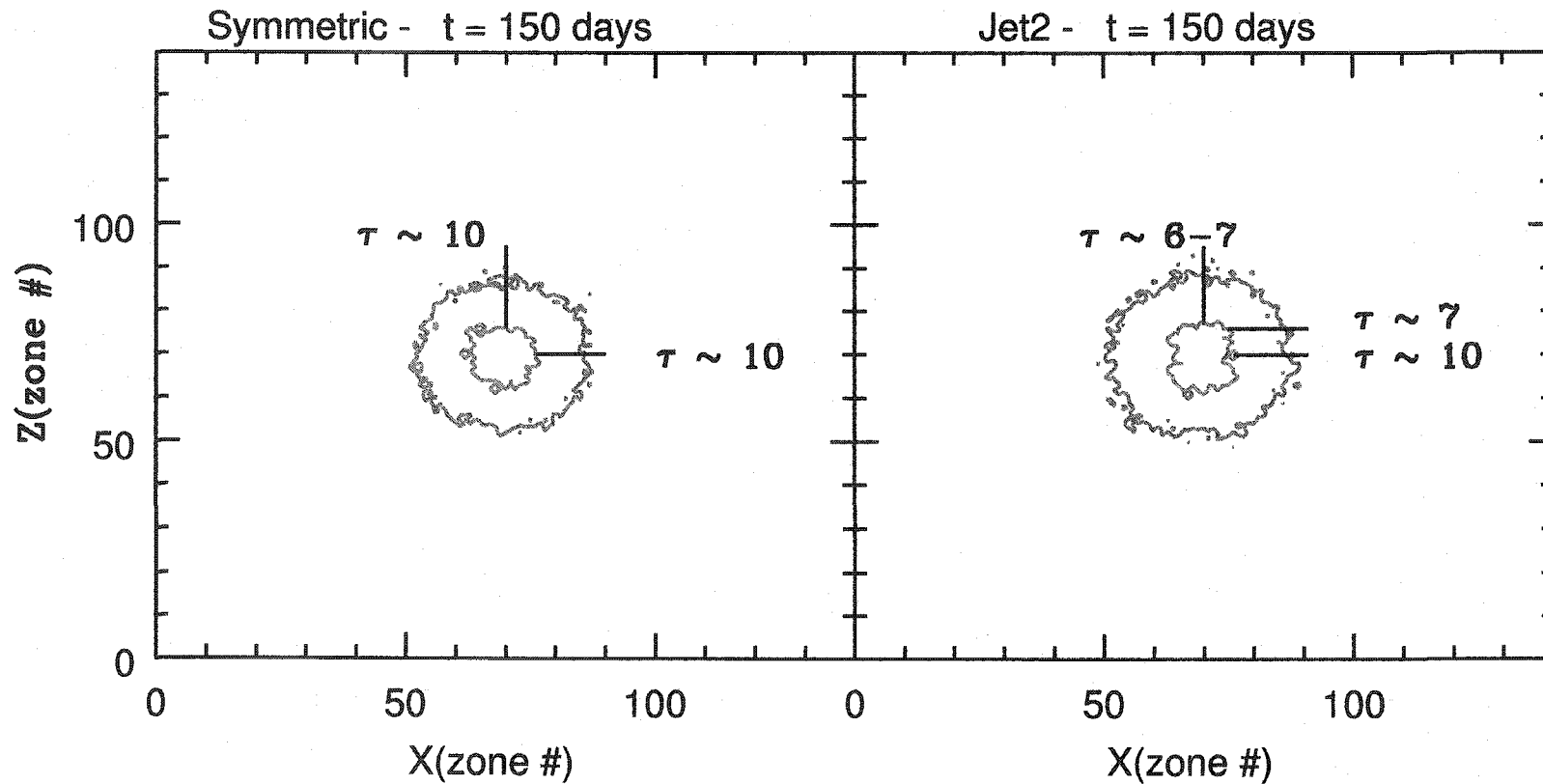


FIGURE 3.9. Contour plots in the  $xz$ -plane of the Symmetric and Jet2 explosion models at  $t = 150$  days. Inner contour is for  $^{56}\text{Co}$  number density which traces the surface of the  $\gamma$ -ray emitting region. Outer contour is for the mass density which follows electron density and thus traces the dominant opacity source (Compton scattering). The lines represent lines-of-sight through the ejecta for which the optical depth from emission region to ejecta surface has been calculated. Regardless of viewing angle, the optical depth of the  $^{56}\text{Co}$  ejected along the poles in the Jet2 explosion remains quite low. Hence, it is this material that dominates the observed emission for all viewing angles in the aspherical explosion.

Jet2 explosion models. At these  $\gamma$ -ray energies, a single Compton scatter reduces the photon energy by roughly a factor of 2. This effectively removes the photon from the line profile region, leaving the  $\gamma$ -ray line profiles to be formed primarily by photons that escape with no interaction. In this way, the broadening of the line is caused entirely by Doppler velocity shifts resulting from the *spatial* distribution of radioactive nickel in the homologously expanding ejecta. The 4 panels shown are for days 200, 250, 300, and 365 after explosion. The three lines in the Jet2 spectra represent different viewing angles through the ejecta (along the pole, the equator and an intermediate angle  $\sim 45^\circ$ .) For the Symmetric spectra, we have plotted these same viewing angles.

Both explosion scenarios (Symmetric and Jet2) show blue-shifted line profiles, though to varying degree. These differences can be best understood by examining the physical effects which dictate the formation of the line profile edges. The blue edge to the lines is set by the maximum observed line of sight velocity of the  $^{56}\text{Co}$  in the ejecta. Since the expansion is basically homologous after 100 days, the line of sight velocity of a fluid element in the ejecta is proportional to its distance above the mid-plane of the explosion. Each spectral energy bin in the line profile can be mapped to a unique line of sight velocity in the ejecta, which can in turn be mapped to a specific height above the mid-plane. For example, defining the line of sight to be along the z-axis, the line profile shape should be proportional to the total mass of Cobalt summed in x and y as a function of z height in the ejecta. Therefore, the bluest edge of the line will arise from material that was mixed furthest out along the line of sight direction.

It is clear from Figure 3.9 that the nickel was mixed furthest out in the polar direction (and thus achieves higher velocities) for the asymmetric explosion. Following the discussion above, it is not surprising that the  $\gamma$ -ray line profiles viewed along the polar direction are much more blueshifted for the Jet2 model than the Symmetric model. Figure 3.9 does not show a very large difference in the extent of mixing along

## Symmetric Model

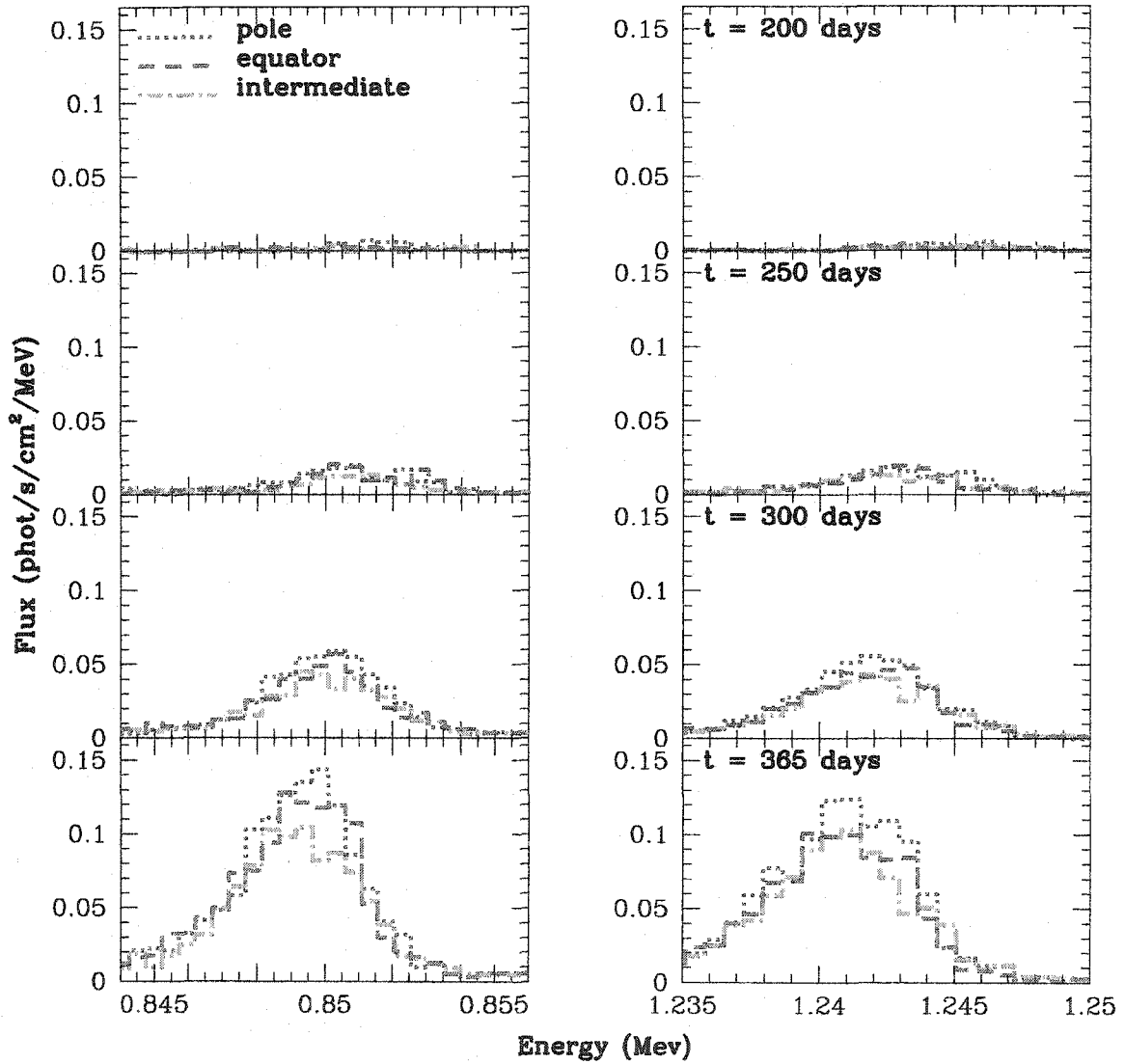


FIGURE 3.10. Line profiles of the  $^{56}\text{Co}$  1.238 and 0.847 MeV lines for the Symmetric model at 4 different times during the explosion (200, 250, 300, 365 days). 3 different viewing angles are shown: polar view (dotted lines), equatorial view (dashed lines) and an intermediate view angle of  $\sim 45^\circ$  (dash-dot lines). The line profiles do not show significant variation with viewing angle (as would be expected for a symmetric explosion.)

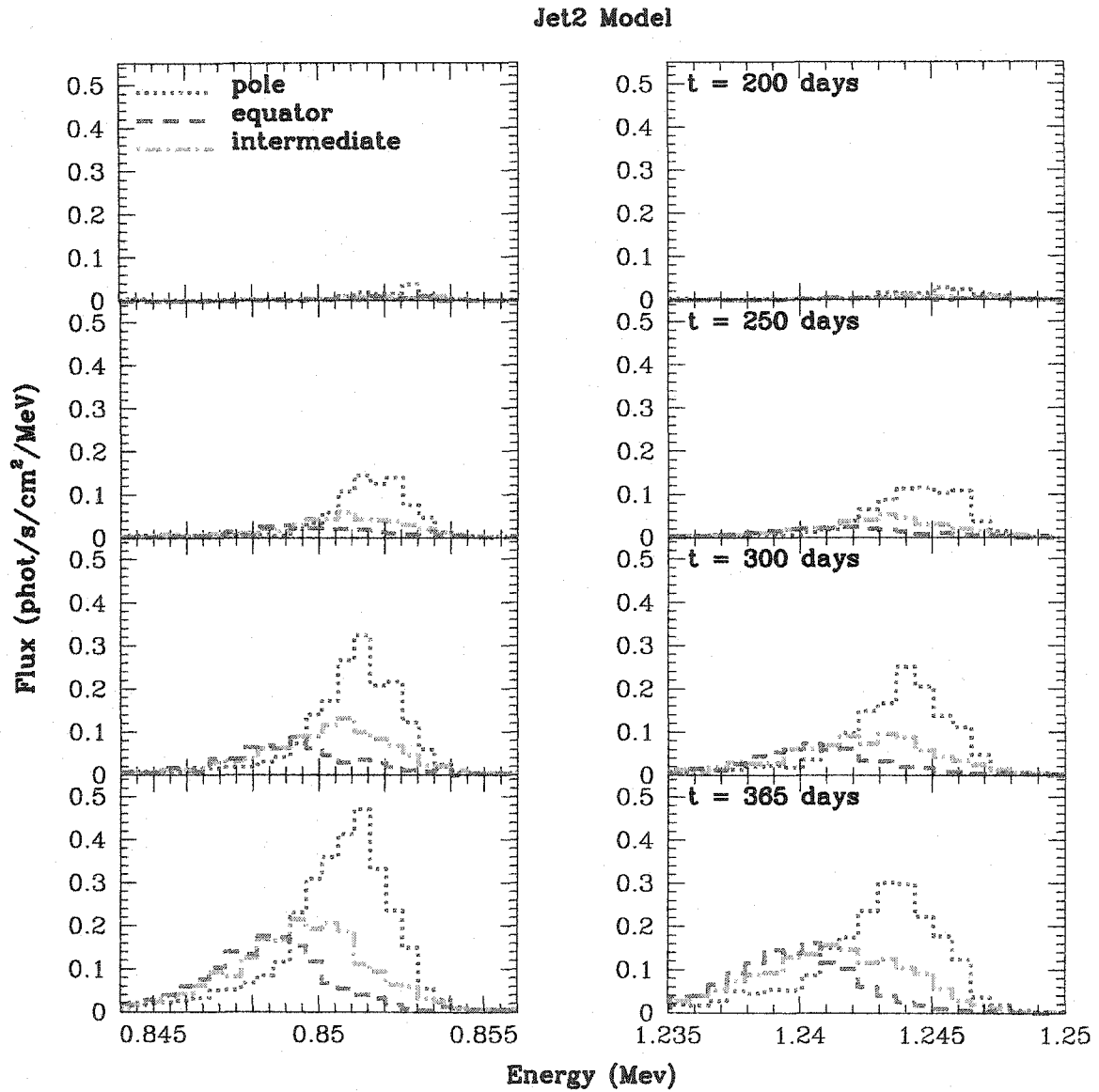


FIGURE 3.11. Line profiles of the  $^{56}\text{Co}$  1.238 and 0.847 MeV lines for the Jet2 model at 4 different times during the explosion (200, 250, 300, 365 days). 3 different viewing angles are shown: polar view (dotted lines), equatorial view (dashed lines) and an intermediate view angle of  $\sim 45^\circ$  (dash-dot lines). The flux axis is scaled by a factor of 4 over the Symmetric model profiles shown in Figure 11. Significant variations in the line profiles with viewing angle are apparent, and can be explained by considering the velocity distribution (and thus radial distribution in a homologous expansion) of the ejecta responsible for the observed emission.

the equatorial direction between the two models. Correspondingly, the blue edge of the Symmetric lines and the equator view of the Jet2 lines are comparable.

The red edge of the lines is determined by the escaping emission from  $^{56}\text{Co}$  with the smallest line of sight velocity in the ejecta. In a Symmetric model, this should be an indication of how deep into the ejecta we can see along a given viewing angle. However, there is a more pronounced effect at play in the asymmetric explosion models. As we mentioned in the previous sub-section, much of the  $\gamma$ -ray emission for the equatorial view arises from the ends of the  $^{56}\text{Co}$  distribution. This material has a very low line of sight velocity for an equatorial observer, since it is being ejected predominantly in the polar direction. This allows for a significantly lower velocity red edge of the equator view lines, even though the optical depth profiles do not vary much between polar and equator viewing angles.

Also note that the line centroids become less blue-shifted with time. As the supernova expands, the opacity in the ejecta drops and emission from material located deeper into the ejecta (and thus at smaller radial velocities) becomes visible. This results in an overall broadening of the line, as well as a redward shift of the line centroid.

### 3.3 Summary

The 3D simulations presented here show that globally asymmetric explosions lead to extensive mixing of the supernova ejecta, placing the products of explosive burning well into the helium layer of the star. Even mild 2:1 asymmetries can mix 10% of the nickel out to the inner edge of the hydrogen layer. If such mixing occurred in weak explosions, as well as the strong explosions presented in this paper, these mildly asymmetric supernova explosions could explain the extensive mixing required in population III stars (Umeda & Nomoto 2002) and black hole binary systems such as Nova Scorpii (Podsiadlowski et al. 2002).

As discussed in the introduction, the observed high energy spectrum of SN 1987A differed from the predictions of spherically symmetric modeling efforts in two fundamental ways. Both the broad lines of nickel and the early emergence of the hard X-rays could be explained qualitatively by invoking a mixing argument. From a theoretical standpoint, including a 1D prescription for that mixing makes the assumption that both data points can be fit with one free parameter. However, the simulations in this work suggest that the addition of a global asymmetry will change the direct correlation between the emergence time and the degree of line broadening. That is to say, for a given hard X-ray flux, the Symmetric model will correspond to a single line profile, regardless of viewing angle. The Jet2 model, however, produces similar hard X-ray continua for different viewing angles, but the line profile varies significantly with viewing angle.

In fact, the data for SN 1987A (the  $\gamma$ -line profiles and hard X-ray continuum) were not fit well by 1D models. In particular, the model 10HMM (Pinto & Woosley 1988b), which was mixed sufficiently to account for the flux in the hard X-ray continuum observations, resulted in  $\gamma$ -line centroids that were shifted too far to the blue and were too narrow (Tueller et al. 1990). Although the uncertainties in this data were relatively large, this trend may be in the right direction to suggest a global asymmetry. That is to say, an asymmetric explosion scenario for SN 1987A could produce the same hard X-ray flux level, but with a redder and broader line profile than the symmetric explosion scenario. While it is heartening that these simulations seem capable of supplying the enhanced mixing and broad line features observed toward SN 1987A, there remain features that they cannot explain.

For example, while the heavy element distribution does retain some of the explosion asymmetry, it also reflects the relatively smooth nature of the imposed velocity asymmetry (the angular profile of the input asymmetry was sinusoidal.) The mixing fingers are a small perturbation on the oblong cobalt distribution and do not provide any larger scale clumping in the outer envelope. This, combined with the essentially

spherical density distribution of the ejecta, make it very difficult to explain phenomena like the “Bochum event” (the high velocity red bump of emission seen in H- $\alpha$ ), or the “jet”-like structure observed in optical and X-ray emission towards Cassiopeia A SNR. Furthermore, the  $\gamma$ -ray line profiles from SN 1987A were in fact redshifted, a trend that is not obtained with these simulations. Although the  $\gamma$ -ray data uncertainties were quite high, this redshift was also observed in the mid-infrared forbidden lines of [FeII] and [Co II], possibly implying a verification for the  $\gamma$ -ray line centroid measurements (see Figure 1.3). A caveat to keep in mind for this argument is that alternative mechanisms for obtaining redshifts at infrared wavelengths do exist. In particular, Witteborn et al. (1989) showed that electron scattering effects from a homologously expanding envelope (at relatively low optical depth  $\sim 0.4$ ) were capable of matching the redshifted lines of Ar II (which exhibited similar features to the [FeII] line). The  $\gamma$ -ray lines do not suffer from this scattering effect, so as discussed above, the spectral line shape in the  $\gamma$ -lines is directly correlated with the total cobalt mass at a given z-coordinate along the line of sight. With this in mind, the observed redshifted line profiles towards SN 1987A imply, not only a break in spherical symmetry, but also a break in axisymmetry of the ejecta. Namely, there should be more nickel/cobalt mass on the far side of SN 1987A’s ejecta as seen from our viewing angle, implying a one-sided explosion mechanism.

Even more compelling than the Cas A morphology, the H- $\alpha$  and redshifted  $\gamma$ -line observations, are radio pulsar velocity measurements, which provide irrefutable evidence as to the existence of one-sided supernova explosions. Motivated by this evidence, the next chapter will take a parameterized look at single lobe explosions which have been seen to develop in core-collapse modeling efforts (Scheck et al. 2004, Burrows & Hayes 1996, Fryer & Warren 2002, Fryer 2004). In particular, we will place special emphasis on the resulting  $\gamma$ -ray line profiles and their observational potential for probing asymmetries of a “unipolar” nature.

## Chapter 4

### GAMMA-RAY LINE EMISSION FROM UNIPOLAR SUPERNOVAE

While a bipolar structure is the natural consequence of rotationally-induced asymmetries, a supernova explosion need not be bipolar. As discussed in the last chapter, there is strong evidence that core-collapse supernovae are one-sided. One of the strongest pieces of evidence for this is the high velocities of pulsars. These neutron stars are believed to attain these high velocities during their formation in the collapse of massive stars. One of the most striking examples is the beautiful Palomar Telescope image of the Guitar Nebula (reproduced in Figure 4.1). This image shows a supernova remnant (the body of the guitar) with a “kicked” neutron star being ejected from the remnant center, complete with a bow shock as it pushes its way through the surrounding medium (forging the neck of the guitar). Proper motion measurements of the head of the bow shock give a velocity of greater than  $\sim 1000$  km/s for the neutron star (Chatterjee & Cordes 2002). While its velocity places this neutron star near the high end of the observed pulsar velocity distribution, it is not off the charts. Figure 4.2 shows a theoretical fit (based on the observed properties of  $\sim 500$  radio pulsars) to the distribution of birth velocities for neutron stars. The distribution is bimodal, with peaks at 90 km/s and 500 km/s; each peak represents roughly 1/2 the total population. It is possible that the low-velocity peak of this distribution can be explained by nascent neutron stars retaining some amount of orbital velocity following a binary system disruption. However, the high-velocity peak cannot be explained by this mechanism; no binary system has nearly this orbital velocity. This argues strongly for the presence of a large impulse imparted to a significant fraction of neutron stars at the moment of their birth.

If the neutron stars formed in stellar collapse receive a kick during their forma-



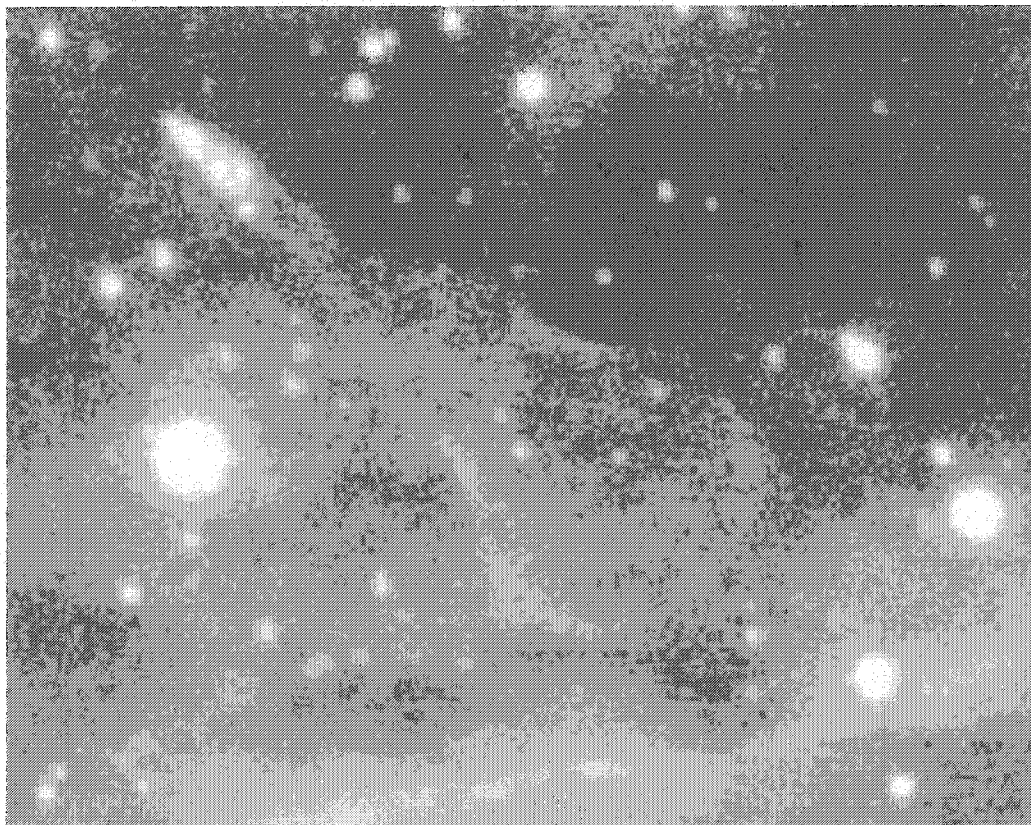


FIGURE 4.1. Image of the Guitar Nebula from the Hale Telescope at Palomar Observatory. (Chatterjee & Cordes 2002, reproduced by permission of the AAS)

tion, momentum conservation requires that some aspect of the explosion must also be asymmetric. Most of the proposed mechanisms for kicks rely on one of two asymmetries: asymmetries in the neutrino emission near the proto-neutron star (Arras & Lai 1999; Fryer 2004), and asymmetries in the explosive ejecta (Herant 1995; Burrows & Hayes 1996; Scheck et al. 2004). While the pulsar velocity distribution does not favor either asymmetry over the other, asymmetries in the ejected material might be able to match additional observations like the shifted  $\gamma$ -line and infrared line profiles mentioned in the introduction. A study by Grant & Dean (1993) demonstrated that ejecta asymmetries (in particular, asymmetries in the  $^{56}\text{Ni}$  distribution) were capable of reproducing the  $\gamma$ -ray line redshifts observed towards SN 1987A. However, their

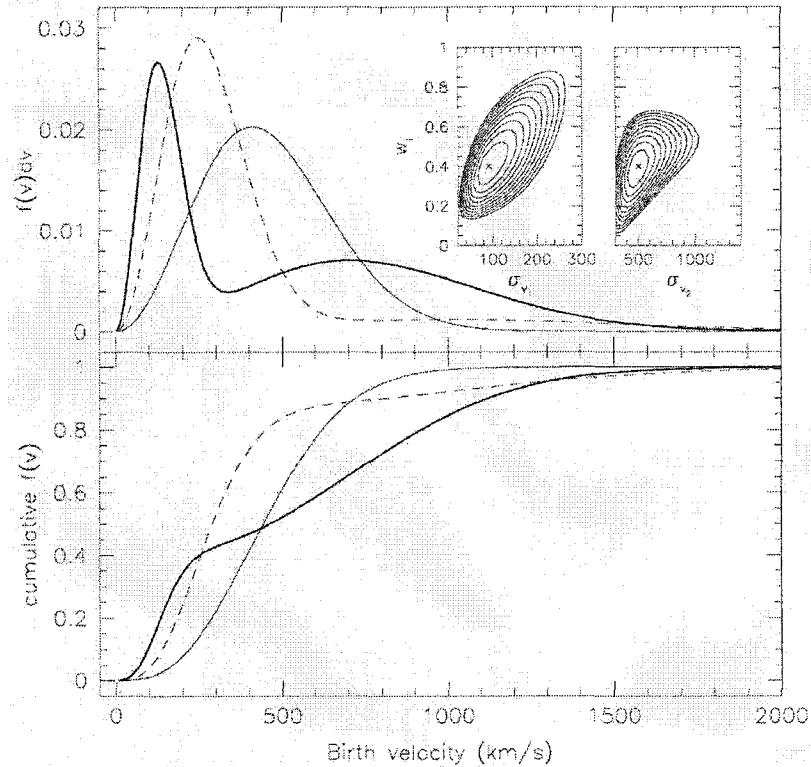


FIGURE 4.2. Pulsar velocity distribution (bold line in top panel) taken from Arzoumanian et al. 2002. (reproduced by permission of the AAS)

treatment of the asymmetry was at the level of a toy model, and the extent of the assumed asymmetry was extreme. Recent core-collapse simulations of Scheck et al. (2004) provide a more realistic representation of the asymmetric structure one could expect to arise within the context of stellar collapse. Their simulations show that asymmetries arise naturally within the standard model of convective, neutrino-driven supernovae. They find uni-polar or single-lobe asymmetries capable of imparting kicks from 0 km/s to 1500 km/s. These low-mode asymmetries result from merging hydrodynamic downflows in the convective region just outside the proto-neutron star.

In this chapter we undertake the same Monte Carlo post-processing of 3D hydrodynamic simulations to investigate the range of  $\gamma$ -ray line profiles which result from parameterized single-lobe explosions. We choose the structure of our input asymme-

try so as to mimic the asymmetries found in the Scheck et al. (2004) simulations. We investigate two different asymmetry configurations with kick velocities that bracket the observed range.

## 4.1 Explosion Simulations

For our parametric study of single-lobe explosion asymmetries, we use the same  $15 M_{\odot}$  progenitor star (s15s7b2 from Weaver & Woosley 1993) used in chapter 3. As in the previous chapter, we use hydrodynamic simulations to study the outward mixing of nickel in three dimensions. Low mode asymmetries in the explosion will lead to lopsided nickel distributions and may affect the nucleosynthetic yield of nickel. The simulations presented here concentrate on the hydrodynamic mixing motions and do not include the effects of enhanced nucleosynthetic yields.

### 4.1.1 Numerical Schemes

Roughly 1.2 million variably massed particles are used in the SPH simulation. The neutron star (with mass of  $1.4 M_{\odot}$ ) is cut out of the simulation, though its gravitational effect is mimicked with a central gravitational force term<sup>1</sup>. As with the bipolar asymmetries, the single lobe asymmetry is imparted by artificially altering the explosion velocities at 100 s after bounce. These input asymmetries require a magnitude of velocity enhancement and an angular profile describing the assumed structure of the asymmetry. In the previous chapter, the angular dependence of the imposed velocity asymmetry was chosen to be sinusoidal. This decision was made primarily to facilitate

---

<sup>1</sup>This is not a self-consistent treatment as the neutron star will have some velocity associated with it in order to conserve momentum in these one-sided explosions. The ejecta which are important for our  $\gamma$ -ray studies are homologously expanding with velocities greater than the escape velocity within a few weeks after the explosion is launched. The fastest moving neutron star in our simulations has a position offset from the center of the ejecta of roughly 20% the radius. This does not significantly affect the outflow trajectory of the ejecta that has already received escape velocity. In addition, this offset corresponds to material not yet probed by the escaping  $\gamma$ -ray emission, and can be neglected for this epoch.

closer comparison with the results of Nagataki et al. (2000) who also assumed this smoothly varying cosine behavior. Comparing with the 2D rotating collapse simulations of Fryer & Heger (2000) and the single lobe simulations of Scheck et al. (2004), we find that a sinusoidal velocity profile is probably smoother than the actual profiles in the hydrodynamic models. Figure 4.3 shows the SPH particle velocities from Fryer & Heger (2000) with a sinusoidal fit overplotted. A top-hat, with its sharp transition, represents the other extreme in fitting the asymmetries from the explosion models (Figure 4.3).

Our set of single lobe explosion asymmetries are created assuming the discontinuous top-hat distribution, which represents a conical geometry and can be described by two primary parameters: 1)  $\Theta$  = opening angle of the enhanced explosion cone, and 2)  $f$  = ratio of in-cone velocity to the corresponding out-of-cone velocity. The in-cone and out-of-cone radial velocities are determined by keeping the same kinetic energy as the symmetric explosion while forcing  $f$  to a chosen value. They are given by:

$$V_{in-cone} = f \left[ \frac{1-f^2}{2} \cos(\Theta) + \frac{1+f^2}{2} \right]^{-\frac{1}{2}} V_{symm} \quad (4.1)$$

and

$$V_{out-of-cone} = \left[ \frac{1-f^2}{2} \cos(\Theta) + \frac{1+f^2}{2} \right]^{-\frac{1}{2}} V_{symm} \quad (4.2)$$

where  $V_{symm}$  is the radial velocity from the input 1D calculation.

The computational intensity of these simulations allowed only 2 different conical geometries to be explored. The models are referred to as f2th20 and f3th40, corresponding to  $\Theta=20$ ,  $f=2$  and  $\Theta=40$ ,  $f=3$  respectively. As mentioned above, our choice of parameter values for this study were guided by the multi-dimensional simulations of Scheck et al. (2004) and Blondin et al. (2003), which find low mode instabilities driving the SN explosion. The kick velocities resulting from these input asymmetries

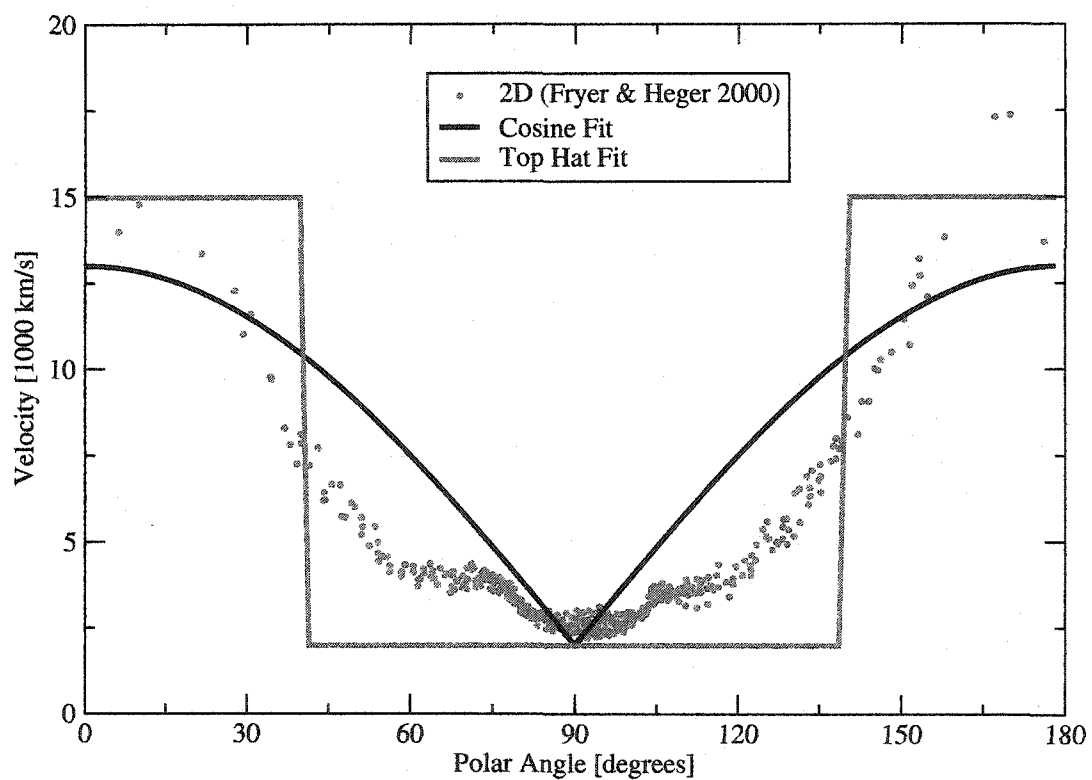


FIGURE 4.3. Plot of radial velocity versus polar angle for the 2D rotating collapse model of Fryer & Heger (2000). Overplotted are a cosine function and top-hat function which represent the two assumed profiles for the artificial velocity asymmetries imposed in this work. Note that the model profile lies somewhere between these two extremes.

were determined to be 100 km/s and 1700 km/s from calculations of the non-zero ejecta momentum imposed by the conical asymmetry. A neutron star mass of  $1.4 M_{\odot}$  was assumed. Plots of the initial kinetic energy distribution in angle are shown in Figures 4.8 and 4.9. The transition from the region of low velocity to the conical region of high velocity is clearly discontinuous and was adopted to more easily facilitate composite 1D studies of trends in nucleosynthetic yields.

#### 4.1.2 Explosion and Nickel Distribution

Figures 4.4 and 4.5 are the multi-dimensional plot counterparts of Figures 3.3 and 3.5 from Chapter 3. They give a nice global view of the ejecta morphologies which develop from our set of parameterized explosions. In particular, it is clear that the density asymmetries (background colored contours) in both of the single lobe explosion models are much more extreme than for the bipolar explosions. The 3:1 velocity asymmetry of model f3th40 is sufficient to push through the entire star, creating a spray of heavy elements at the outermost edge of the expanding ejecta. Even the 2:1 velocity asymmetry in model f2th20 leads to aggressive outward mixing of nickel and its decay products, placing them very near the edge of the stellar ejecta as well. The magnitude of these velocity asymmetries do not differ significantly from those of the Jet2 bipolar explosion model, so this increased extent of heavy element mixing is somewhat surprising. However, the angular profile of the velocity asymmetry differed appreciably between the two types of imposed asymmetry. As mentioned above, the bipolar explosions were given a smoothly varying cosine velocity asymmetry, while the single lobe explosions assume a discontinuous “top-hat” profile in polar angle. The discontinuity of the single lobe models allows a significant portion of the high velocity region to expand without drag from fluid shear forces, and is likely the cause of the increased heavy element penetration in the single lobe explosion models.

A more quantitative look at the mass motions and energetics of the explosions

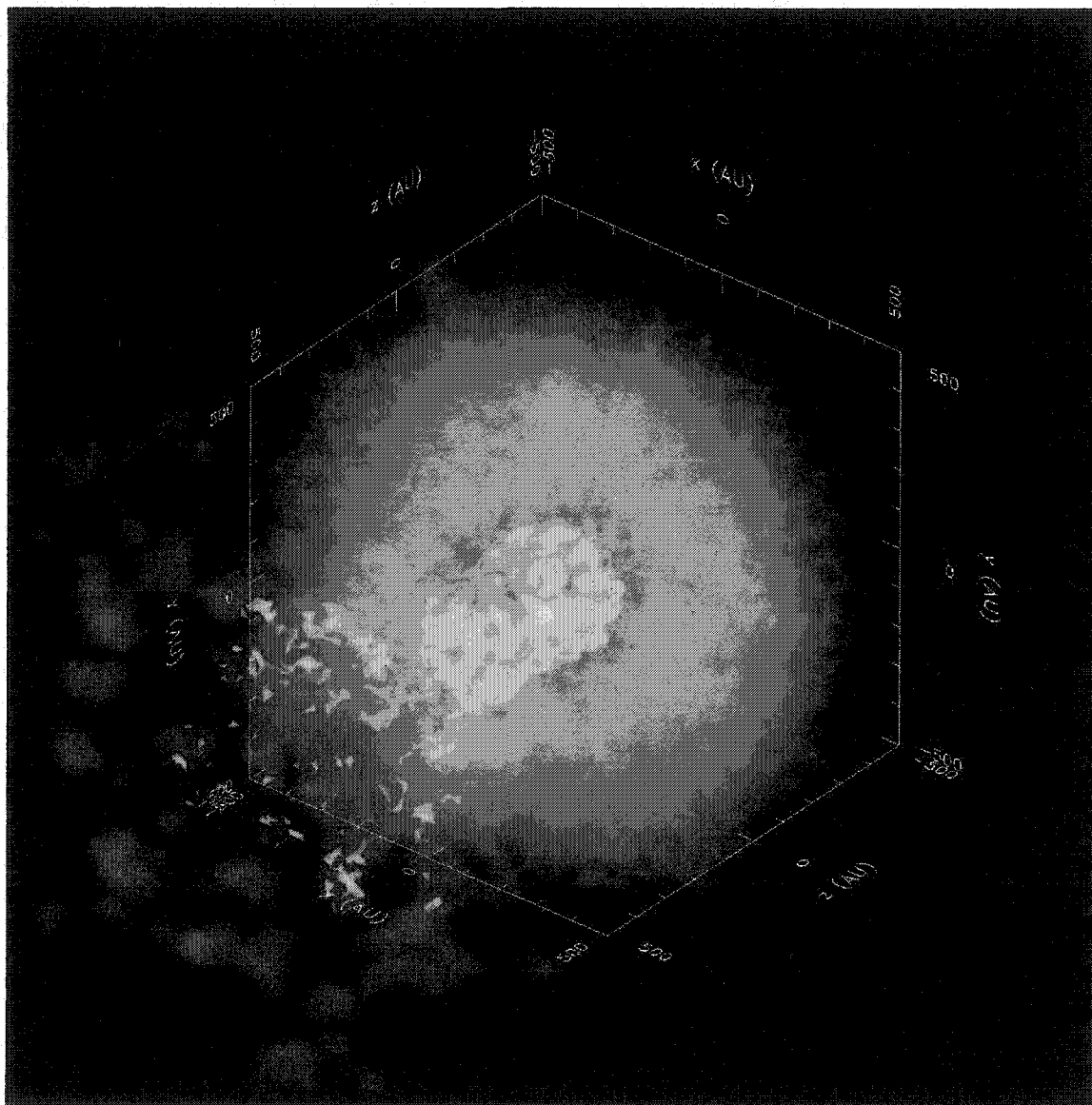


FIGURE 4.4. 3-dimensional rendering of the f3th40 explosion model 1 year after the shock launch. The isosurface represents the cobalt distribution with a number density of  $10^{-5}$ . The colors denote the density distribution. The top-hat distribution of the imposed velocity asymmetry allows a significant portion of the cone material to expand without drag from fluid shear forces, resulting in the large splash of material at the outer ejecta.

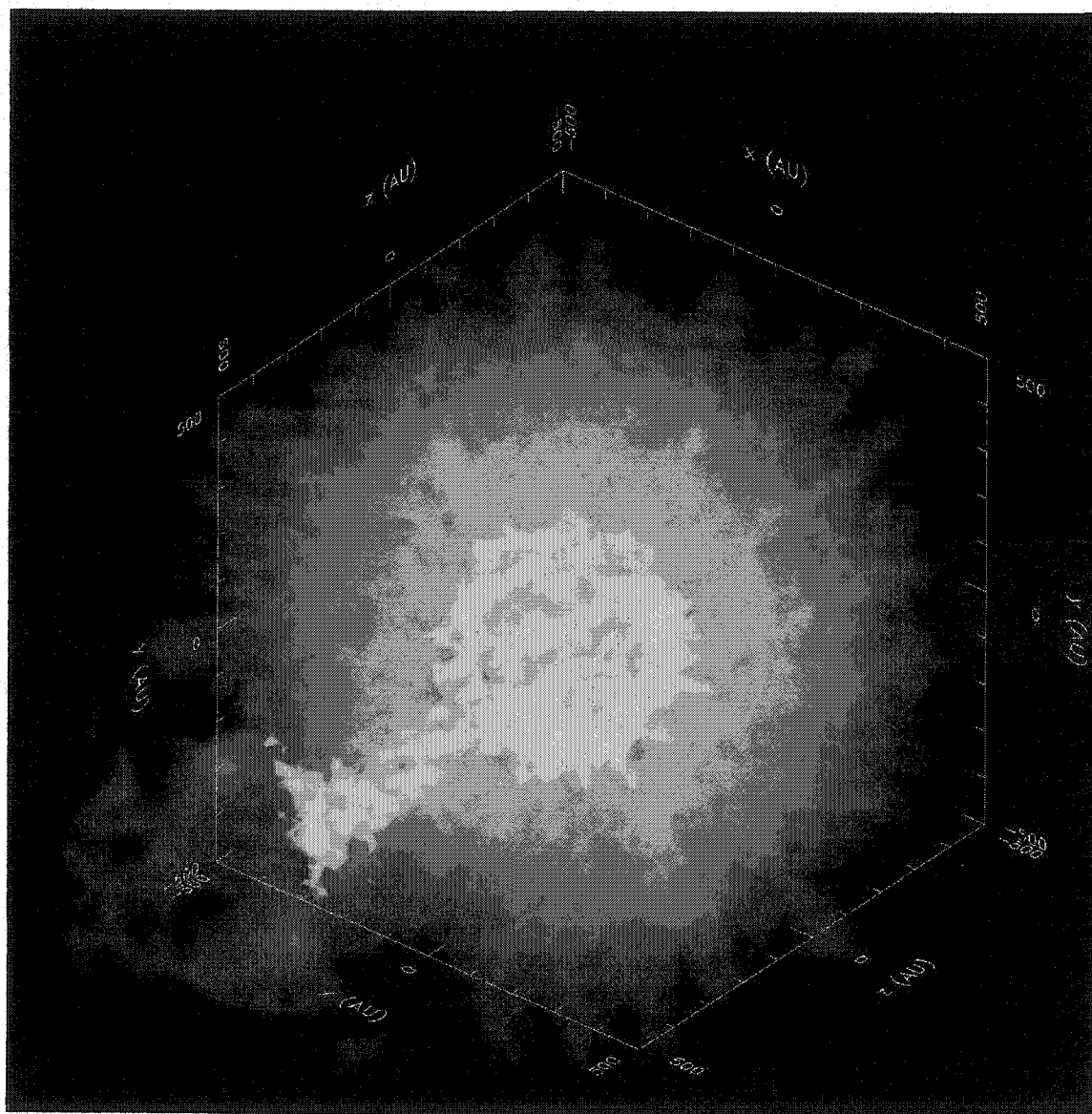


FIGURE 4.5. Same as previous figure, but for model f2th20. Again we see the splash of cobalt in the outer ejecta, though not as extreme due to the smaller angle and lower contrast of the velocity asymmetry.



can be seen in Figures 4.6 - 4.9 where the kinetic energy and mass are shown in cones with a  $9^\circ$  angular radius for a variety of polar angles in both explosion models. The blue curve in each plot is for the initial simulation time (100 s), and the red curve is at later times when the ejecta flow has become homologous. From the mass distributions, we see that the mass in the enhanced explosion lobe has increased while the mass at angles just outside the cone has been reduced. This trend is relatively easy to understand without invoking complicated hydrodynamics. Imagine a child at play in the ballroom of any arcade. Initially, the sea of colorful balls surrounds the child at a relatively uniform height. However, as the child moves through the sea of balls, he creates at his back a deficit of balls equal to the build up of additional balls at his front. This emptiness is filled primarily by the cascade of balls adjacent to the child's wake. The unipolar explosion is similar, in that the fast expanding cone initially creates a low density area into which the surrounding material is funneled, thus increasing the total mass in the cone region at the expense of the material just outside the cone. This migration of material to the high velocity cone region affects the heavy element distribution as well, resulting in a larger mass of radioactive nickel within the cone. For the specific case of model f3th40, the enhanced explosion lobe is sufficiently energetic to poke a hole out of the star, spraying the matter from this cone in all directions. This leaves it with an overall enhancement in mass over the enhanced velocity cone, but actually results in a reduction of material right along the cone axis. The f2th20 model was not energetic enough to poke through the edge of the envelope, so it retains the mass enhancement over the entire cone region.

In conjunction with the mass distributions, the energy distributions show that a spherization of the explosion is taking place. While the mass in the cone has increased over time, the kinetic energy of the cone material has actually dropped off. This lost energy is spreading to the rest of the ejecta, equalizing the explosion velocities in angle. In the bipolar explosions from Chapter 3, the spherization of the explosion was essentially complete once the shock had passed through the star. For the single

lobe explosions here, the density contours are not yet spherical after the shock has passed through the entire star. This is heartening as the morphology of SNR Cas A (with its optical jet) may require such a density asymmetry to survive not just propagation through the star, but even significant interaction with the interstellar medium.

For the purposes of understanding the redshifted line profiles of SN 1987A, we take a more detailed look at the nature of the lopsided nickel distribution. Figures 4.10 and 4.11 show contours of density (blue) and cobalt number density (red) in the x-z plane of model f3th40 and f2th20 at 365 days. In the panels surrounding the contour map are plotted the underlying nickel distributions versus line of sight velocity for various viewing angles. These profiles are a rough approximation to compare against observations at wavelengths where the optical depth is likely to be small (such as the infrared lines discussed in the introduction). The broadest line profiles are obtained when looking along the axis of the explosion asymmetry and are, if anything, narrower than the bipolar and symmetric explosions from Chapter 3 (Figure 4.12 shows similar information for the Jet2 model of the previous chapter for comparison). This is the price paid for the extreme outward mixing of these single lobe, top-hat explosion asymmetries: a much smaller fraction of the nickel mass is outwardly mixed for these discontinuous velocity distributions. The sinusoidal velocity profiles have very little material with velocities equal to the peak velocity enhancement, but much more material with milder enhancements. This gives rise to a larger mass of moderately mixed heavy elements compared to the simulations with an assumed top-hat distribution. This can be seen in the broader central line feature of the Jet2 model. There is, however, a highly mixed “spray” component seen in the unipolar models that the bipolar explosions do not possess. This extremely mixed nickel component adds a bump at high velocity, which is particularly interesting as such a “bump” was invoked to explain irregularities in the H- $\alpha$  line observations of SN 1987A (i.e. “the Bochum event”).

## Model f3th40

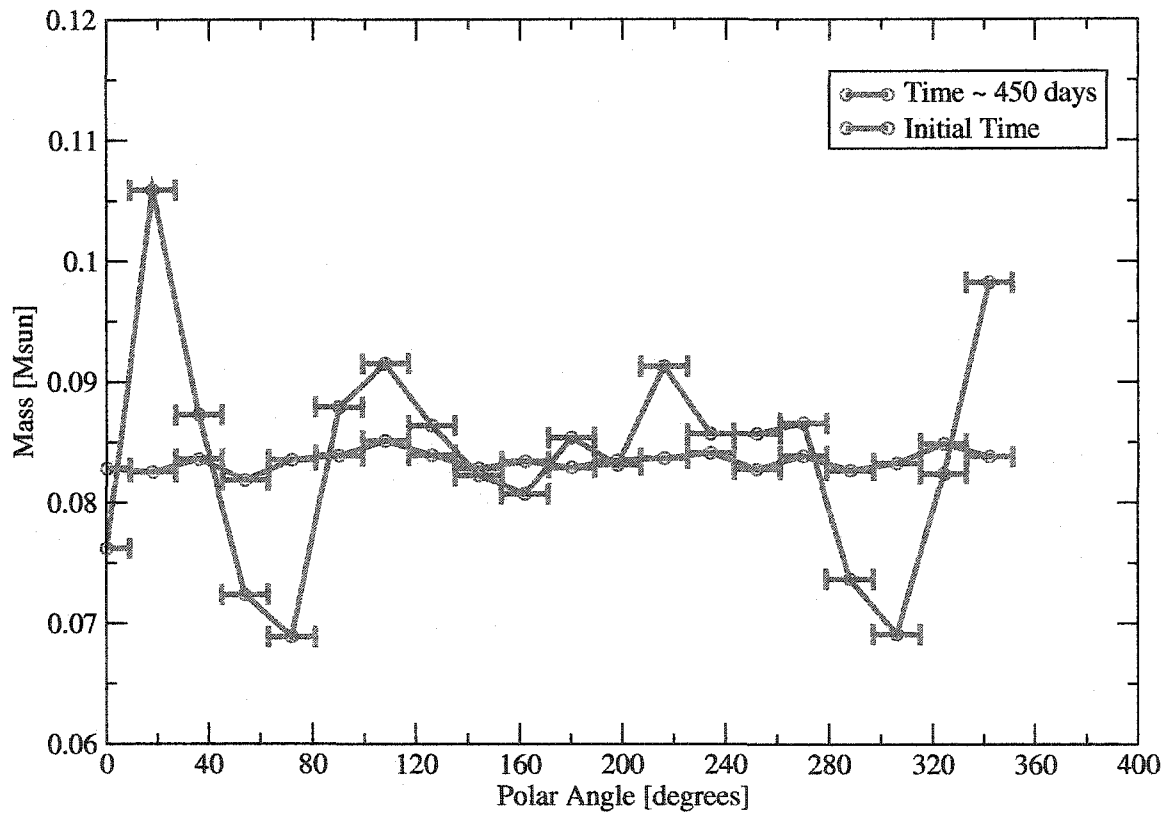


FIGURE 4.6. Plot of mass in a cone of radius  $9^\circ$  along a direction in polar angle for the f3th40 model. Error bars reflect the cone diameter. Blue line is for the initial time at  $t = 100$  s and red line is for  $t = 450$  days (long after flow has become homologous.) Matter is being funneled into the faster expanding, lower density region in the cone. This results in an enhancement of the mass for polar angles near zero, and a reduction in mass for angles just outside of this.

## Model f2th20

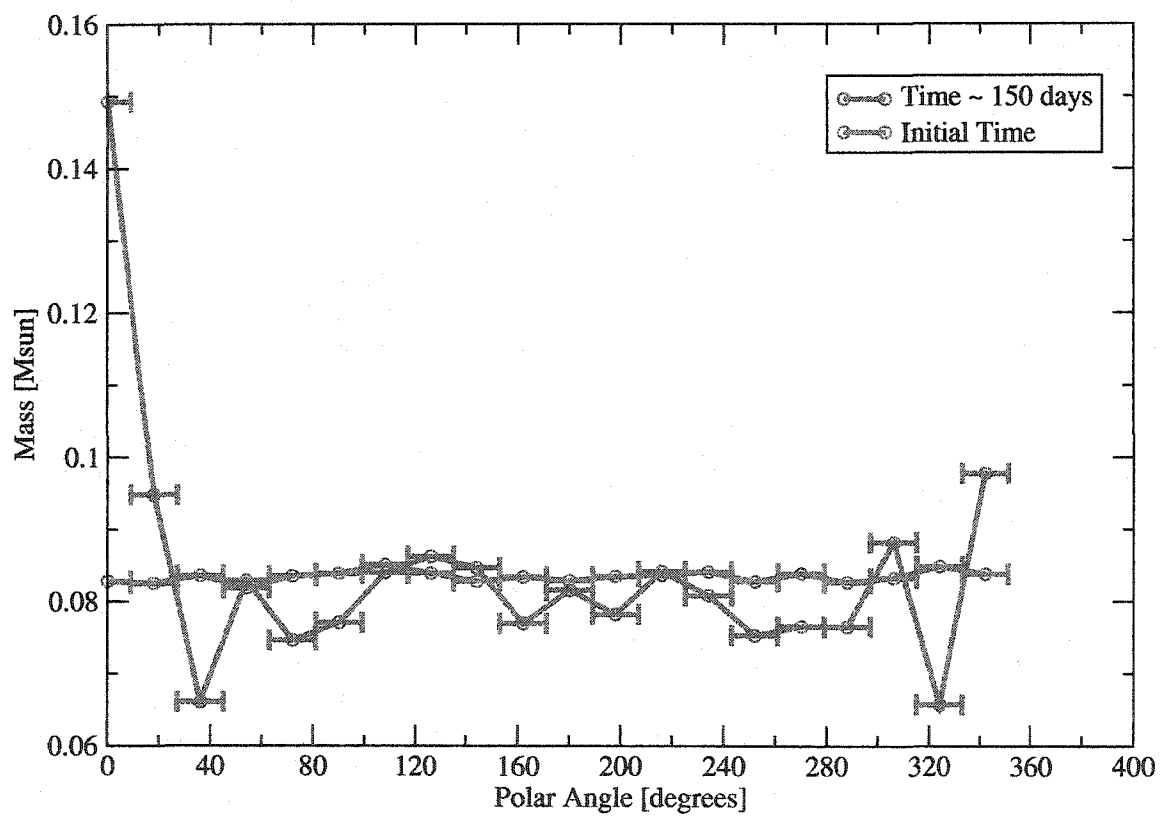


FIGURE 4.7. Similar to the previous figure, but for model f2th20 at  $t = 150$  d. The ejecta have already reached the phase of homologous expansion, so can be directly compared with the f3th40 results.

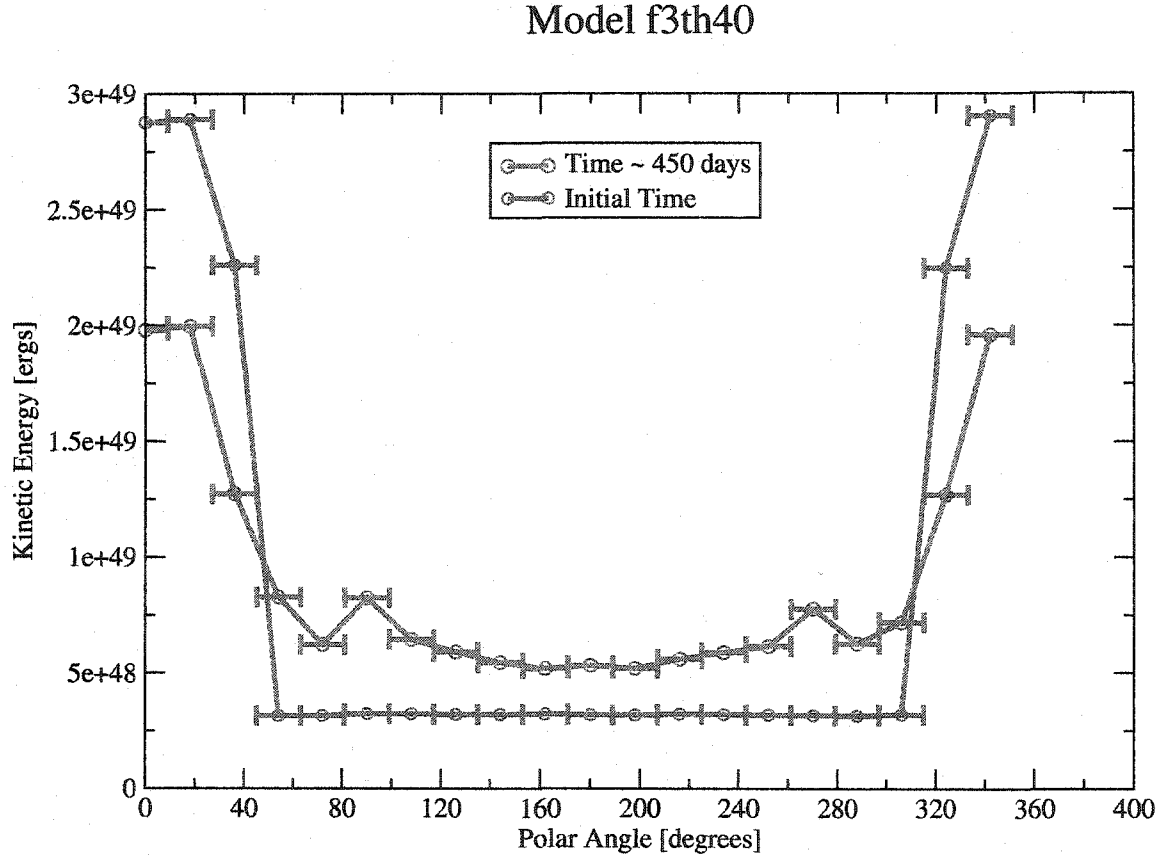


FIGURE 4.8. Similar to the previous figures, but showing kinetic energy as a function of polar angle for the f3th40 model. Blue line is for the initial time at  $t = 100$  s and red line is for  $t = 450$  days (long after flow has become homologous.) It is clear that the explosion is spherizing (i.e. energy in the enhanced explosion lobe is smearing and being shared with the rest of the ejecta.) Note from the previous figures that the mass in the cone actually increases at later times, suggesting that the velocity structure is even more spherical than the energy distribution shown here. Still, after having the shock pass through the entire star, there does still remain some asymmetry in contrast to the complete spherization of the bipolar explosion models.

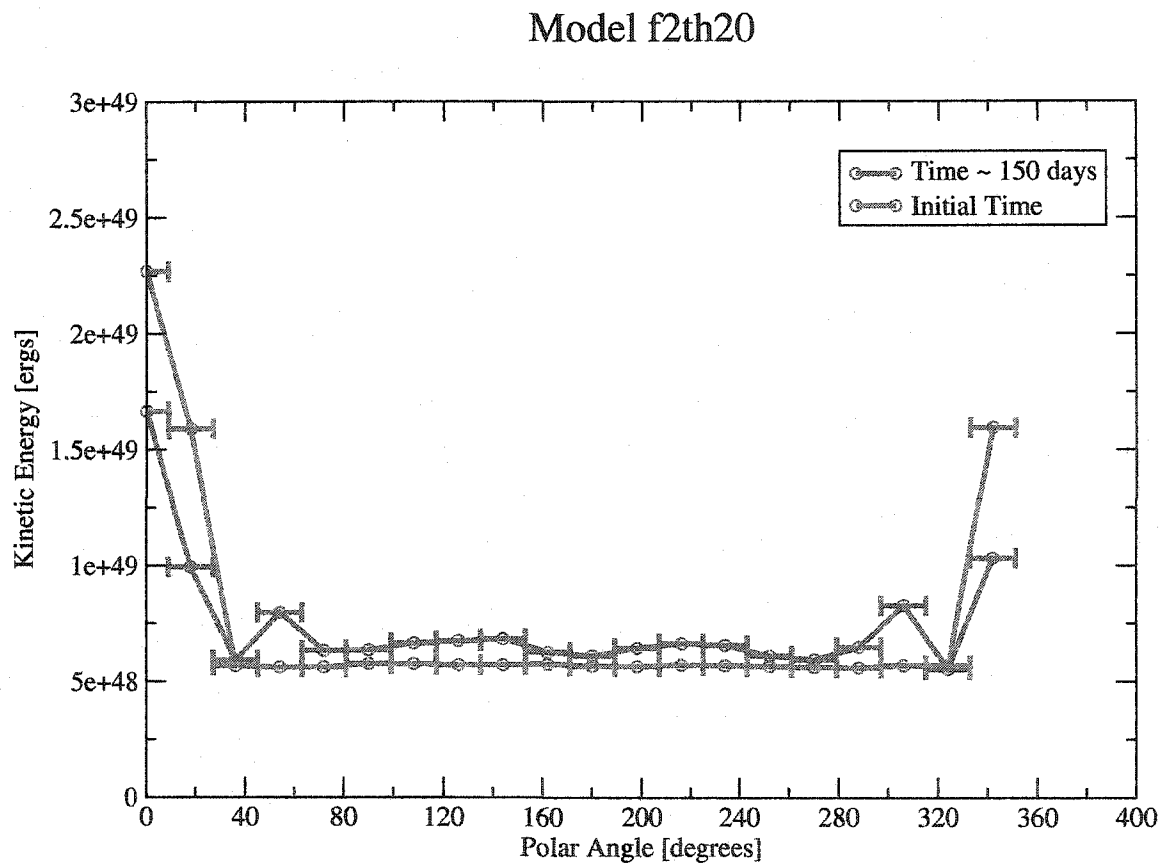


FIGURE 4.9. Similar to the previous figure, but for model f2th20 at  $t = 150$  d. The ejecta have already reached the phase of homologous expansion, so can be directly compared with the f3th40 results.

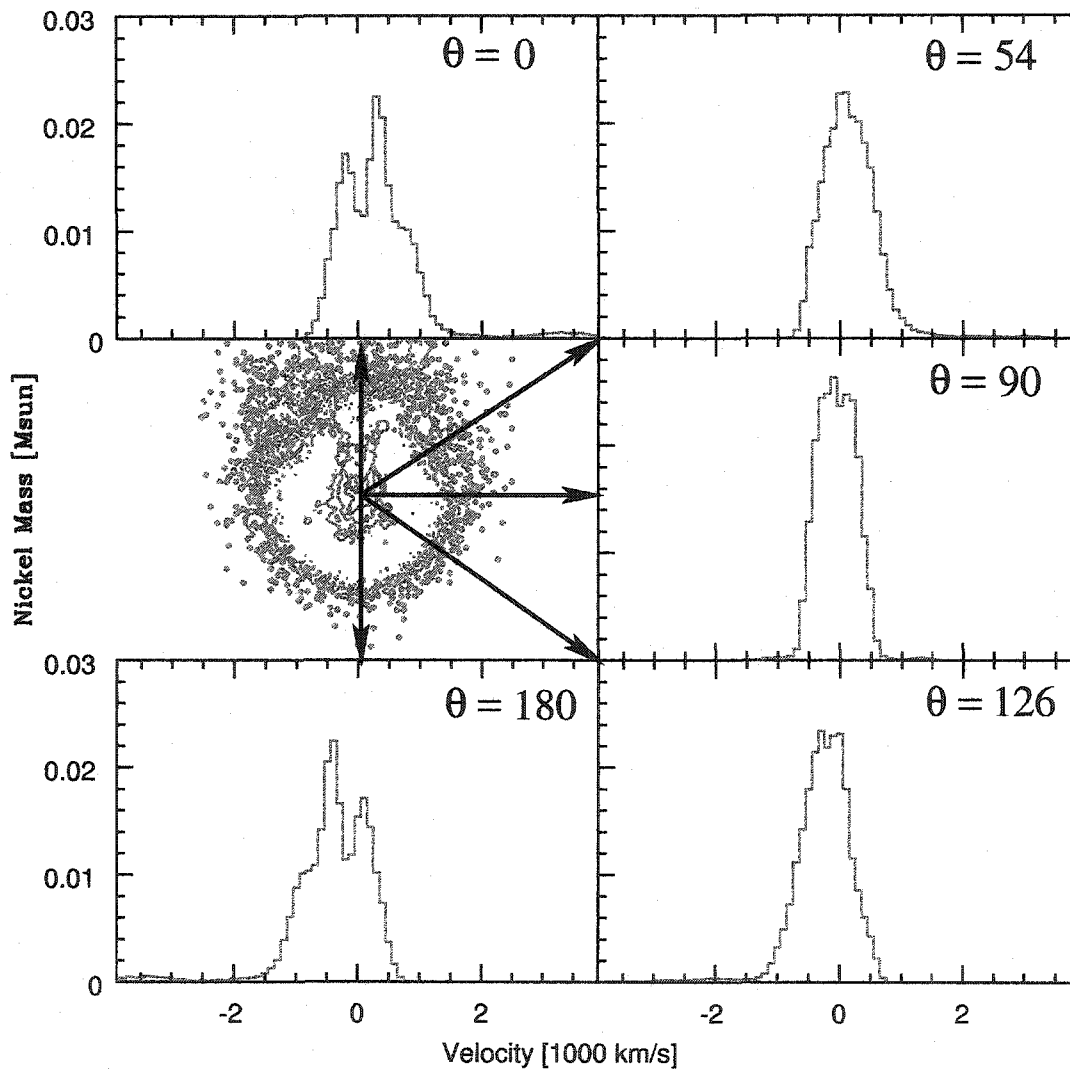


FIGURE 4.10. Mass of 56-weight elements (e.g. initial  $^{56}\text{Ni}$  mass) versus line of sight velocity for a number of viewing angles at  $t = 365$  days. Central panel on the left shows a contour plot of density (blue) and cobalt number density (red). Due to the homologous nature of the expansion, these distributions represent the line shapes one would expect from nickel, cobalt or iron emission in the absence of significant ionization or opacity effects.

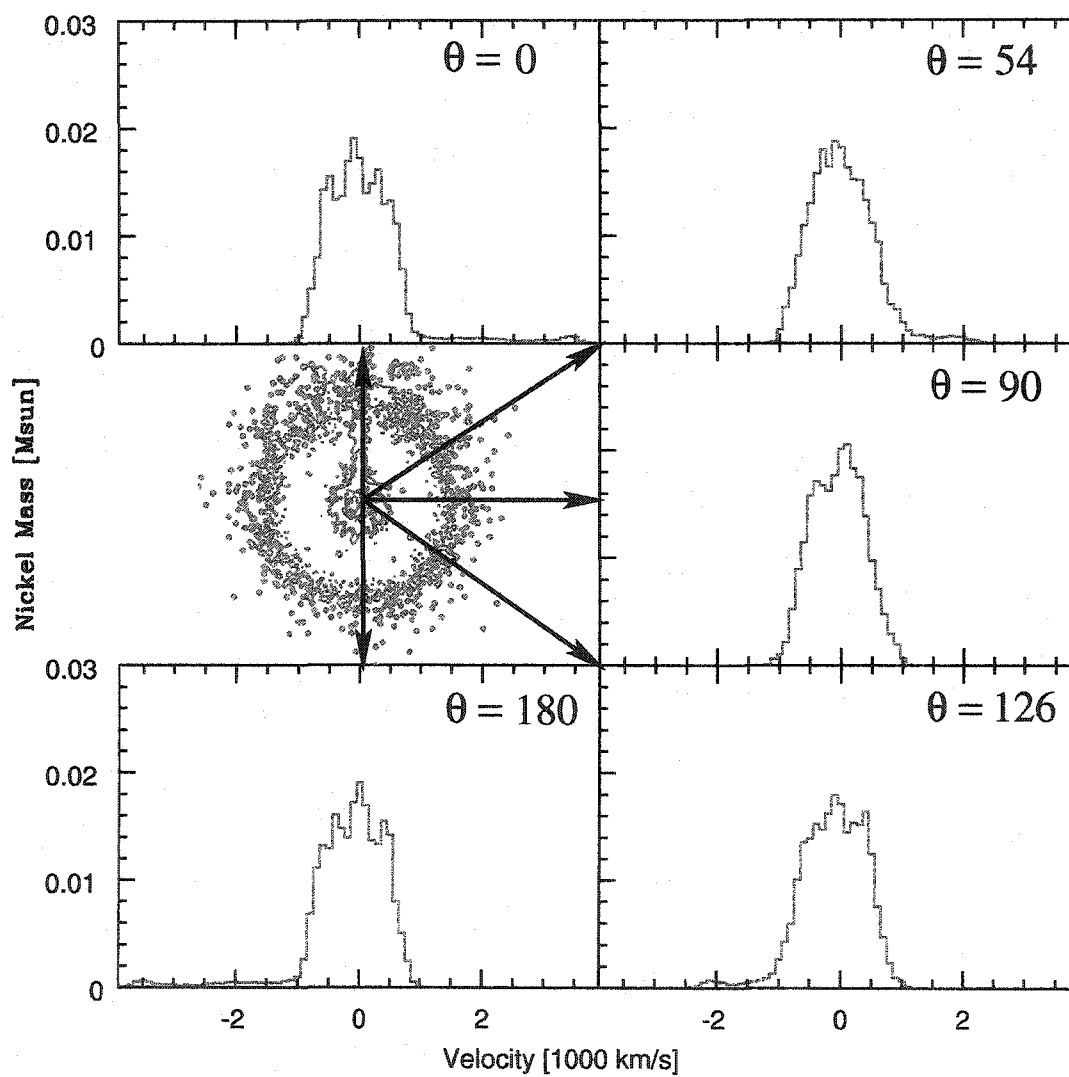


FIGURE 4.11. Same as previous figure, but for model f2th20.



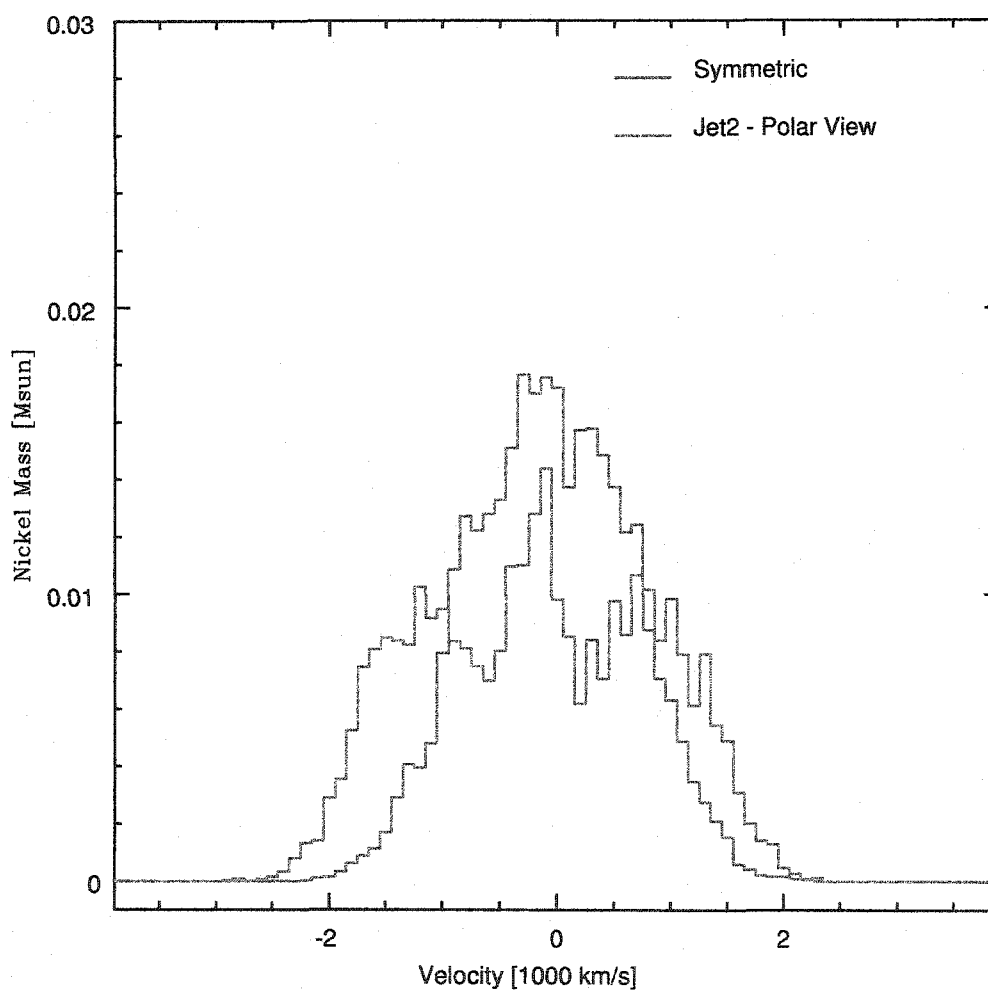


FIGURE 4.12. Mass of 56-weight elements (e.g. initial  $^{56}\text{Ni}$  mass) as a function of line of sight velocity for the Jet2 (polar view) and Symmetric explosion models of Chapter 3. Note the broader line profile for the Jet2, and even the Symmetric model, as compared to either of the unipolar explosion models. Also note the absence of higher velocity structure as compared to the unipolar models.

## 4.2 High Energy Spectral Calculations

We now turn to studying the effects these hydrodynamic asymmetries have on the  $\gamma$ -ray spectra and fluxes. In particular, we can test to see if one-sided explosion asymmetries can produce redshifts in the  $\gamma$ -line profiles. We concentrate our  $\gamma$ -transport simulation efforts on the ejecta structures at a single time ( $t = 1$  yr), and investigate trends in the line centroid shift with viewing angle. As we mentioned before, the progenitor star used in these simulations differs appreciably from the best-fit progenitor to SN 1987A. This precludes us from directly comparing our theoretical line shifts to the  $\gamma$ -line observations of Tueller et al. (1990) and the observed [FeII] forbidden lines from Spyromillio et al. (1990) and Haas et al. (1990).

### 4.2.1 Numerical Schemes

As with the previous simulations, our input models of the supernova ejecta (element abundances, density and velocities) are taken from the f2th20 and f3th40 SPH explosion simulations described above and mapped onto a  $140 \times 140 \times 140$  Cartesian grid. Escaping photons were tallied into 250 coarse energy bins, with finer binning at the decay line energies to provide line profile information. The emergent photons were also tallied into 11 angular bins ( $\Delta\theta = 10^\circ$ ). While the input data is not of an axisymmetric nature, the set of angles chosen are fairly representative of the overall structure.

Roughly  $5 \times 10^9$  Monte Carlo photon bundles were generated for each input model, in proportion to the mass of radioactive material distributed throughout the ejecta. For these models, photoelectric and pair production opacities were calculated for the elements H, He, C, O, Ne, Mg, Si, Fe, Co, and Ni. These elements correspond to those used in the nuclear network by Timmes, Hoffman & Woosley (2000), which has been incorporated into the SPH code but was turned off in these calculations for computational efficiency. This reduction in the number of elements treated manifests

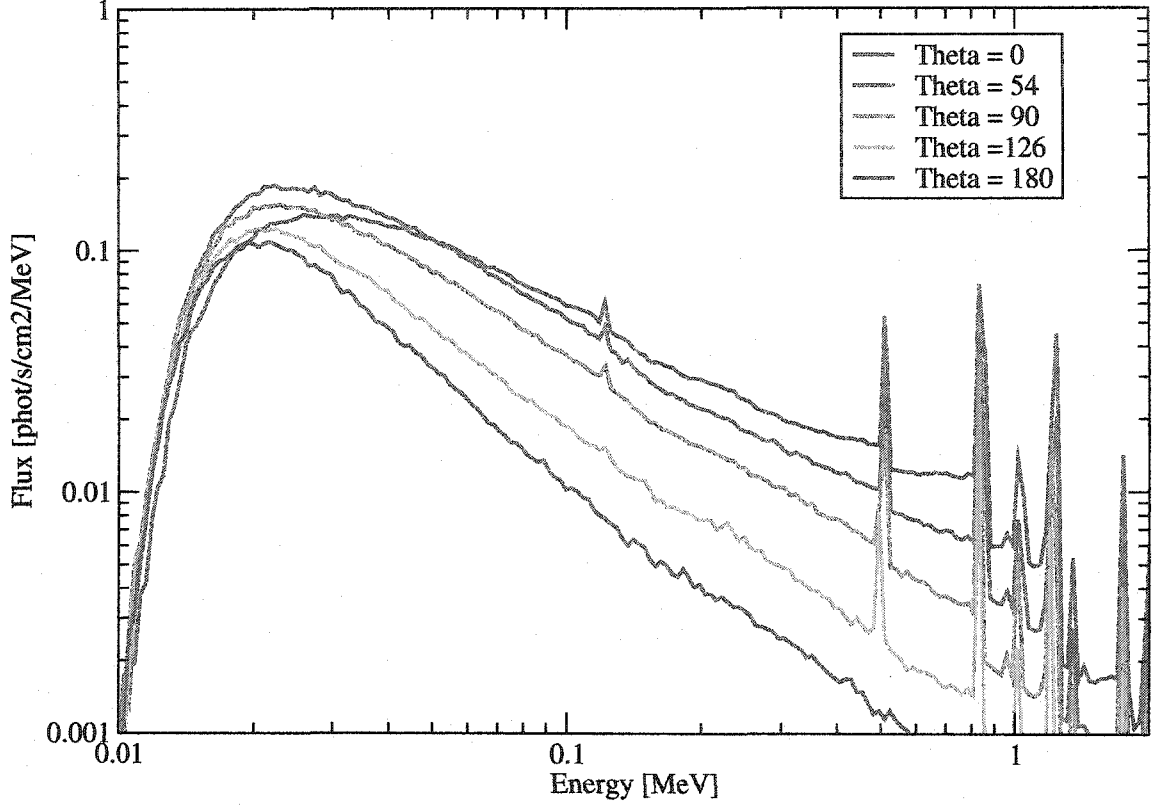


FIGURE 4.13. Logarithmic plot of total hard X- and  $\gamma$ -ray spectrum at  $t=365$  d for model f3th40. The flux was calculated assuming a distance of 60 kpc. The different colored lines refer to different viewing angles through the ejecta. Theta = 0 viewing angle is looking down the explosion lobe (positive z-axis) and Theta = 90 is perpendicular (looking down the positive x-axis). Theta = 0 direction shows a higher energy turnover indicating a larger abundance of heavy elements mixed to the outer ejecta.

itself in small variations in the spectral turnover at low energies, but does not affect the Compton scattered continuum as  $Y_e$ , and hence the electron density, is same. In all other aspects the details of the simulations remain the same as before.

#### 4.2.2 Hard X-ray and Gamma-ray Spectrum

Figures 4.13 and 4.14 are logarithmic plots of photon flux in units of  $\text{phot/s/MeV/cm}^2$  across the energy range investigated with these simulations (0.3 keV - 4 MeV). We

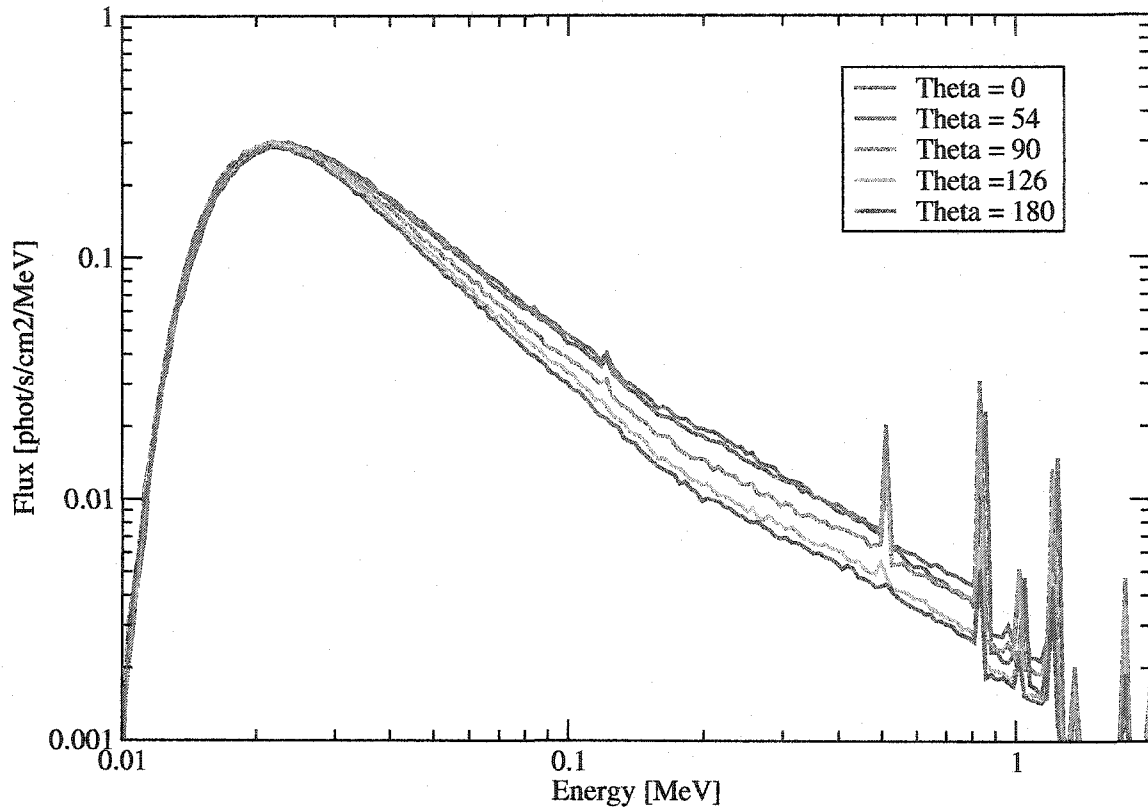


FIGURE 4.14. Same as previous figure, but for model f2th20.

have placed this object at the distance of the Large Magellanic Cloud (60 kpc) for easy comparison with flux data from SN 1987A observations. The 5 colored lines plotted represent the spectrum emerging along 5 different viewing angles as labeled in the legend. Variations between the spectra arising from different viewing angles provide qualitative information about the element distribution in the ejecta. For example, the earlier turnover for viewing angles along the explosion lobe are indicative of the enhanced abundance of heavy elements at large distances along this axis.

The general picture to keep in mind is that photons contributing to the lower energy Comptonized spectrum were emitted deep in the ejecta and have scattered repeatedly in their journey outwards. So there is a loose correlation between the photon's energy and its outward progress through the ejecta. The energy at which bound free cross sections begin to dominate the Compton scatter cross section is

element dependent. After a sufficient number of scatterings (which corresponds to a rough distance out in the ejecta) the photon's energy will be low enough to have entered the region dominated by bound free absorption. The turnover energy will reflect the mix of elements (i.e. the metallicity) in the material at this ejecta location. For example, by the time a typical  $\gamma$ -ray is down scattered enough to be photoelectrically absorbed, it will have made its way to the outer ejecta. The composition of this outlying material has been basically unchanged by the passage of the shock and reflects the metallicity of the star forming region from which it was born. The metallicity dependence of the spectral turnover is shown quantitatively in Figure 2 of Grebenev & Sunyaev (1987). They calculate a turnover energy of roughly 20 keV for solar metallicity, in agreement with the majority of viewing angles shown in our models. However, for the "Theta=0" direction in model f3th40 (and to a lesser extent in model f2th20), the turnover begins at higher energy suggesting that a significant amount of heavier elements have been mixed out to the region where photoelectric absorptions dominate.

### 4.2.3 Gamma-ray Line Profiles

Figures 4.15 and 4.16 show the 847 keV  $\gamma$ -ray line profiles for both single lobe explosion models. The plots are the same layout and represent the same viewing angles as in Figures 4.10 and 4.11. These figures demonstrate that redshifted line profiles *are* attainable given the types of asymmetries assumed here. However, it is clear by comparing to Figures 4.10 and 4.11 that the line profiles do not reflect the entirety of the underlying nickel distribution. Indeed, as we argued in the previous chapter, the high energy emission can be understood by assuming that the emission at all viewing angles is dominated by the extremities of the nickel distribution (which has mostly decayed to cobalt at this epoch.)

Recall from Chapter 3 that each energy bin in the Doppler broadened profile can

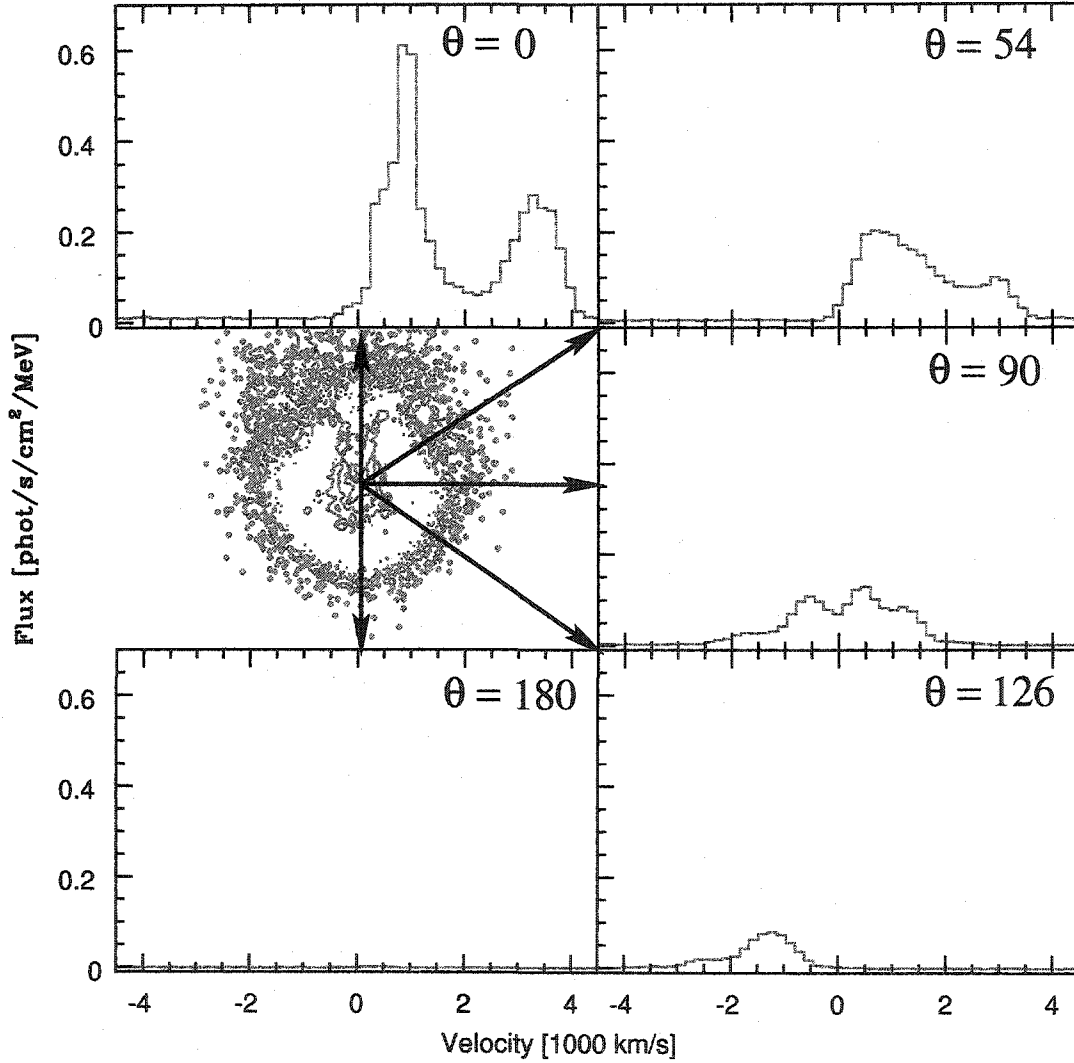


FIGURE 4.15. Line profiles of the  $^{56}\text{Co}$  847 keV decay line for model f3th40 at  $t = 365$  days. Central panel on the left shows a contour plot of density (blue) and cobalt number density (red). Surrounding panels represent line profiles for the set of viewing angles depicted by the black vectors overplotted on the density contours. The emission in the line profiles arises predominantly from the cobalt ejected along the enhanced explosion lobe. Due to the homologous nature of the ejecta, the structure in the lines can be understood by summing this extended cobalt material along lines perpendicular to the viewing angle vectors. See text for a more in depth discussion.

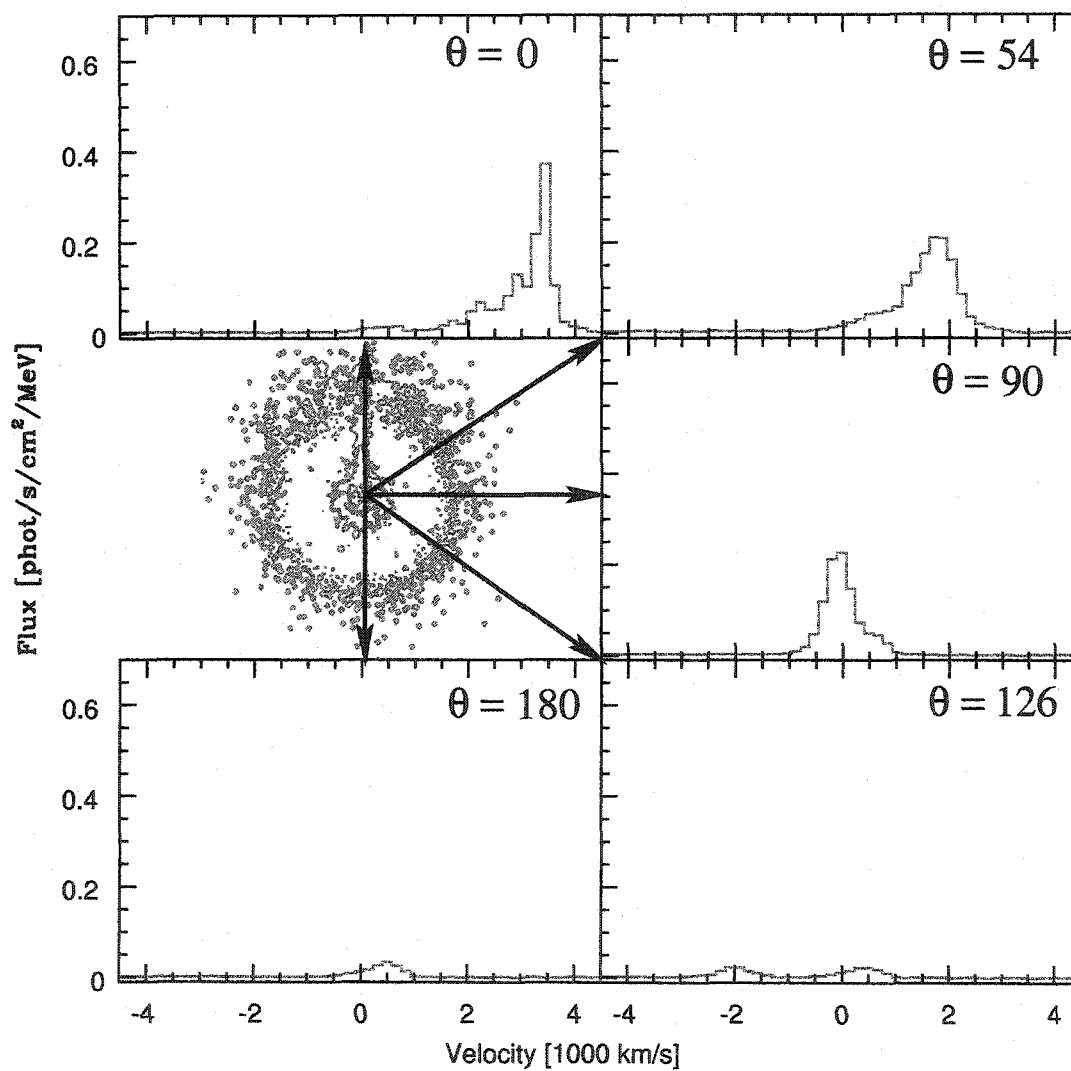


FIGURE 4.16. Same as previous figure, but for model f2th20.

be mapped to a spatial location in the ejecta. This is due to the homologous nature of the expansion, in which line of sight velocity is proportional to line of sight distance from the mid-plane of the explosion. Keeping this in mind, one can use the structure of the cobalt contour plots in Figures 4.15 and 4.16 to understand the line profiles plotted in the surrounding panels. Each energy bin in the line profile corresponds to emission from all the cobalt located along a line perpendicular to the viewing angle vector (black line drawn from explosion center to line profile panel.)

In particular, for the f3th40 model, the base of the antenna-like structures is the primary emission site for  $\gamma$ -rays that escape at all angles. For the  $\theta=0$  direction, this leads to a blue shifted line with a long blue wing contributed by photons from the antenna structures themselves. The  $\theta=90$  direction shows two separate peaks with emission shoulders to the red and blue. The peaks arise from the structure just at the split of the two antennae, with the near side giving rise to the slightly blueshifted peak and the far side making up the slightly redshifted peak. The shoulders on these peaks arise from the emission of the antenna material. The same correspondence between the outlying cobalt distribution and line profile structure can be made for the f2th20 model. In each panel there is a small contribution from the mildly blueshifted material at the outer edge of the spherical structure in the center. However, for the viewing angles with a clear view to the cylindrical structure along the z-axis, the profiles are dominated by that emission. In particular, the  $\theta=0$  direction shows a strongly blueshifted peak from the spray at the end of the cylinder and a shallow redward wing from the emission of the cylinder itself. In the  $\theta=90$  direction, the high z-velocity material in the cylinder has a low line of sight velocity and gives an emission peak at roughly the rest frequency. However, this profile does show extended red and blue wings arising from the spray at the end of the cylindrical structure.

While it is encouraging that such a line shape can be reproduced at all, it is important to note that in both models the redshifted line shape comes at the expense of line flux. We see significant redshifts because we see only a fraction of the radioactive



emission which has been mixed out to low densities in the ejecta (and thus low opacities.) Indeed, the integrated flux for any viewing angle in the 847 keV line represents only a few percent of the total flux from the  $0.24 M_{\odot}$  of nickel ejected in these models. The  $\gamma$ -line observations of SN 1987A implied 20% escape fraction at roughly 400 days (Tueller et al. 1990), however the explosion energy for SN 1987A was roughly twice that of our simulations. The faster expansion velocity would result in lower opacities at similar epochs allowing for a larger escape fraction than we find for our models. However, for the models considered here, a larger escape fraction would mean a more significant contribution from the spherically distributed nickel deeper in the ejecta, possibly washing out the redshift in the observed profile.

Without the benefit of a model progenitor tuned specifically to SN 1987A, we cannot say much as to how the cobalt distribution and opacity profile will affect this detailed interplay between line shift and line flux. However, we can say that, for the specific explosion parameters assumed here, the asymmetry in the explosion manifests itself most clearly in the “spray” of heavy elements along the enhanced explosion lobe. It is the detailed structure of this nickel “spray” that is directly probed by the  $\gamma$ -ray line profiles at this epoch, thus probing the material most likely to indicate a break in global symmetry. There remain many “ifs” regarding the ability of this mechanism to match the line fluxes and time evolution of the  $\gamma$ -ray lines of SN 1987A. However, the outlook is good that this may be the solution we have been looking for and a serious effort to match the SN 1987A data specifically using asymmetries of this nature is definitely warranted.

#### 4.2.4 Summary

The hydrodynamic simulations investigated here probe only a small portion of the large parameter space for explosion asymmetries. From this limited sample we can say that the outward mixing of heavy elements in these single lobe explosion mod-

els is more extended than the bipolar explosion simulations of the previous chapter. The differences in adopted angular profile of the imposed velocity asymmetry is likely responsible for this enhancement, rather than the difference between bipolar and unipolar explosion geometry. So, for these particular models, it is the differences in extended nickel distributions which reflect most strongly on the differences in assumed velocity asymmetry. The overall morphology of the f3th40 explosion is particularly reminiscent of the Cassiopeia A supernova remnant in that the heavy element distribution shows a clear “jet” blowing out of the star. Furthermore, the “spray” of material blown out of the star is effectively dispersed, leaving the central pole evacuated of most material. This is consistent with the most recent Chandra images of Cas A (Hwang et al. 2004, in preparation), which reveal an absence of X-ray emitting iron along the “jet” axis.

The high energy transport simulations, which are calculated as a post-process on the hydrodynamic models, verify that redshifted line profiles are attainable for  $\gamma$ -ray decay emission in single lobe explosion asymmetries. However, the redshifted emission is primarily attributed to the “spray” regions of enhanced outward mixing of cobalt. This means that the specifics of the  $\gamma$ -ray line profiles are strongly tied to the structure of the hydrodynamic mixing and do not probe the entirety of the nickel distribution. This is extremely fortunate, as it is this outlying material that contains the most information regarding the initial velocity asymmetry. In this way, the combined sensitivity of the  $\gamma$ -rays to the “spray” material, and the “spray” material to the underlying velocity structure, make the  $\gamma$ -rays an ideal probe of the explosion mechanism itself.

As Figures 4.10-4.12 clearly show, the nickel “spray” region, which gives rise to the redshifted line profiles, comes at the expense of the broad line core. For the Jet2 model in chapter 3, the underlying nickel distribution is extended beyond 2000 km/s for a viewing angle aligned with the enhanced explosion axis. When viewed along the explosion lobe axis, the single lobe explosions have nickel distributions

which are more centrally condensed overall, but with a few percent the total mass mixed to very high velocities of order 3500 km/s. Concentrating on the core of the distribution (where 95% of the nickel mass is located), these profiles are more reminiscent of the Symmetric model nickel distributions. The high velocity imposed on the cone material, when combined with the constraint of keeping the total explosion energy constant, leaves the out-of-cone material with velocities even smaller than the symmetric explosion. The out-of-cone material represents a large fraction of the mass as we've said, so it is not surprising that, if anything, the core distribution is even more centrally condensed in the single lobe explosions. This does not bode well for explaining an earlier emergence time for the hard X-ray continuum, nor the broad nature of the relatively low optical depth infrared lines.

Both asymmetry types discussed (bipolar and unipolar) have strengths and weaknesses regarding their ability to match various aspects of core-collapse supernova observations. Current limitations in computing resources prohibit an exhaustive parameter study of 3-dimensional explosion asymmetries. The work presented here simulates what are likely extreme cases (discontinuous, one-sided velocity asymmetries and sinusoidal, bipolar velocity asymmetries.) Reality is likely to fall somewhere in the middle, and the ultimate value of this work is to demonstrate that the high energy diagnostics are quite sensitive to the details of "where in the middle". This sensitivity makes the high energy emission an excellent probe of supernova explosion asymmetry for nearby supernova events.

## Chapter 5

### SUMMARY

$\gamma$ -ray observations of core-collapse supernovae have played an integral role in motivating theoretical studies to go beyond the spherically symmetric paradigm of stellar structure. The early emergence of  $^{56}\text{Co}$  decay lines observed from SN 1987A, and the broadened, redshifted line profiles in those detections, were among the first observational signs that a break in spherical symmetry had occurred during the supernova explosion. Furthermore, attempts to explain the unexpectedly bright line flux from decay lines of  $^{44}\text{Ti}$  in Cas A have also required the presence of inhomogeneities in the heavy element distribution, and possibly even global asymmetries in the explosion itself.

This thesis has concentrated on translating the ejecta structure from asymmetric, core-collapse supernova models into  $\gamma$ -ray spectral observables. We employed smoothed particle hydrodynamic (SPH) techniques to the problem of calculating the outward mixing of radioactive elements synthesized in the supernova explosion. In particular, we have emphasized the effect that global explosion asymmetries (artificially imposed at 100 seconds after bounce) may have on the extent of this outward mixing. This work differs from previous work in that it treats the problem in 3 dimensions. This avoids the complications of boundary conditions and probes the inherent differences between 2-dimensional and 3-dimensional hydrodynamic instabilities and their evolution. We find that the amount and extent by which the  $^{56}\text{Ni}$  is mixed outward in the supernova ejecta depends sensitively on the nature of the explosion asymmetry. In particular, differences in the angular profile of the imposed velocity asymmetry are evident in the spatial distribution of nickel within the homologously expanding ejecta. Smoothly varying angular profiles give rise to a larger amount of

nickel mass mixed to moderate radii. Narrower, discontinuous profiles eject smaller amounts of nickel to much larger radii, pushing all the way through the ejecta in our most extreme case.

High energy transport calculations are performed as a post-process on these 3-dimensional hydrodynamic structures (using a Monte Carlo transport technique). Multi-dimensional calculations of the hard X- and  $\gamma$ -ray spectrum from core-collapse models have been carried out using toy models for the compositional structure of the supernova ejecta (Grant & Dean 1993; Burrows & Van Riper 1995). These simulations, however, represent the first set of  $\gamma$ -ray emission calculations using realistic hydrodynamic model inputs from core-collapse supernova simulations in 3 dimensions. We find that the  $\gamma$ -ray line emission at roughly 1 year after the explosion probes the extremities of the radioactive nickel/cobalt distribution in the ejecta. The mass and extended nature of this outlying material reflects the nature of the imposed velocity asymmetry. This makes the  $\gamma$ -ray emission a sensitive probe of the underlying explosion asymmetry.

The progenitor star and explosion parameters used in these simulations were not specifically chosen to match those of SN 1987A. We can, however, comment on trends in the high energy observations of SN 1987A and their correspondence to the results found here. The hard X- and  $\gamma$ -ray observations of SN 1987A posed 3 primary puzzles for theoretical models at the time. First, the emergence of the Comptonized hard X-ray continuum was observed by the GINGA satellite much earlier than was expected from spherical models of the supernova explosion. Second, the  $\gamma$ -ray line profiles measured by the Gamma-Ray Imaging Spectrometer (GRIS) were broadened to roughly 3500 km/s. Finally, these same line profiles showed a redshift of roughly 500 km/s relative to the rest-frame of the Large Magellanic cloud. Our high energy calculations probed two types of explosion asymmetries (bipolar and unipolar) in an attempt to reproduce the observed trends.

We find that the hard X-ray continuum is larger for the bipolar model than the

symmetric explosion model regardless of viewing angle, providing an earlier detection for a given sensitivity. The line profiles for polar viewing angles are broadened beyond what could be achieved with a globally symmetric model, though equatorial views show little difference. Mixed versions of spherically symmetric models were forced to fit both the line broadening and early emergence of high energy emission by a single mixing algorithm. In fact, model fits to SN 1987A seemed to have trouble achieving close matches with both observations using only one parameter. This work has shown that the introduction of global asymmetries allows for a variety of line profile shapes with very little variation in hard X-ray continuum, easing the job of matching both observations. However, the bipolar explosions do not reproduce the redshifted line. Our set of unipolar explosions were modeled at a single epoch ( $t = 365$  days) and do not give information as to the early emergence time of the hard X-ray continuum. The underlying nickel distribution in these models is narrower in velocity space for the majority of nickel mass, but with small amounts of nickel (a few percent of the total) mixed to very high velocities. The resulting  $\gamma$ -ray line profiles do exhibit redshifts for certain viewing angles. The line emission arises primarily from the small, but extended “spray” of nickel along the enhanced explosion cone. The redshifted profiles are attained for those viewing angles which see the “sprayed” nickel cone moving away from the observer. The redshifted lines represent emission from only the small amount of nickel mixed to large radii, and for these models, we seem unable to reproduce the enhanced broadening of the line profiles. However, the line width depends sensitively on the structure of the outlying nickel distribution and the viewing angle. While these simulations do not show broad, redshifted profiles, they also do not preclude such a profile from occurring.

The  $\gamma$ -ray studies presented here argue for the utility of high energy observations in diagnosing asymmetric supernova explosions. The material to which the  $\gamma$ -rays are a sensitive probe is the same material that would most obviously demonstrate a break in global explosion symmetry. However, the diagnostic potential requires at

the very least, a comparison of line flux versus continuum flux for these explosions. So the question arises, what is the likelihood of detecting the  $\gamma$ -ray line emission from core-collapse supernovae with current and future  $\gamma$ -ray instruments? Observations at these high energies require space observatories, or at the very least, high-altitude balloon missions. The current state-of-the-art for  $\gamma$ -ray observations is the International Gamma-Ray Astrophysics Laboratory (INTEGRAL, operated by European Space Agency). A caveat to keep in mind is that the nickel mass synthesized in this  $15 M_{\odot}$  model is roughly 2 times larger than the mean observed value ( $\sim 0.13 M_{\odot}$ ; Hamuy 2003) for core-collapse SN explosions. However, as mentioned earlier, the explosion energy was roughly half that of a normal supernova. These two effects serve to balance one another, though it is difficult to determine the exact effect as nickel distributions and optical depth profiles are not simply described.

At energies around 1 MeV, INTEGRAL will have a spectral resolution of 2 keV and a narrow line sensitivity ( $3 \sigma$  in  $10^6$  seconds) of  $\sim 5 \times 10^{-6}$  phot s $^{-1}$  cm $^{-2}$  (Hermesen & Winkler 2002). Our model lines are about 5 times broader than this resolution element, so the sensitivity for detecting them is worse by roughly  $\sqrt{5}$ . Using these specifications, INTEGRAL would be able to detect the  $^{56}\text{Co}$  lines from the polar view of the Jet2 model at a distance of  $\sim 700$  kpc. The single lobe explosion models (looking along the explosion lobe) could be seen to roughly 850 kpc and 300 kpc for the f3th40 and f2th20 models respectively. Table 5.1 shows the luminosities for various continuum energy bands and line energies from the four models studied here (Symmetric, Jet2, f2th20 and f3th40). At these distances (less than a Mpc), the occurrence rate for core-collapse supernovae is essentially the rate for a Galactic event (roughly 1-2 per century; Cappellaro et al. 1993). For a Galactic supernova event, INTEGRAL would be able to measure not only line flux but line profile information, allowing the full diagnostic potential of the  $\gamma$ -rays to be tapped.

However, the event rate at this distance is such that we would be lucky to have even 1 event in the foreseeable future. In order to achieve event rates of order 1 per

Model	Time (day)	3-30 keV (erg s <sup>-1</sup> )	30-100 keV (erg s <sup>-1</sup> )	100-500 keV (erg s <sup>-1</sup> )	847 keV Line (γ s <sup>-1</sup> )	1238 keV Line (γ s <sup>-1</sup> )
Sym	150	$3.715(0.138) \times 10^{35}$	$2.008(0.162) \times 10^{36}$	$6.537(0.930) \times 10^{36}$	$6.828(1.593) \times 10^{41}$	$4.687(1.588) \times 10^{41}$
	200	$5.172(0.044) \times 10^{36}$	$3.183(0.055) \times 10^{37}$	$1.058(0.032) \times 10^{38}$	$1.156(0.061) \times 10^{43}$	$9.622(0.632) \times 10^{42}$
	250	$1.844(0.006) \times 10^{37}$	$1.272(0.009) \times 10^{38}$	$4.302(0.052) \times 10^{38}$	$5.008(0.103) \times 10^{43}$	$4.476(0.106) \times 10^{43}$
	300	$3.714(0.007) \times 10^{37}$	$2.996(0.011) \times 10^{38}$	$1.043(0.007) \times 10^{39}$	$1.362(0.014) \times 10^{44}$	$1.280(0.014) \times 10^{44}$
	365	$4.529(0.010) \times 10^{37}$	$4.910(0.018) \times 10^{38}$	$1.855(0.011) \times 10^{39}$	$3.016(0.027) \times 10^{44}$	$2.886(0.026) \times 10^{44}$
Jet2-E <sup>a</sup>	150	$1.503(0.585) \times 10^{36}$	$9.891(4.221) \times 10^{36}$	$2.812(1.573) \times 10^{37}$	$2.748(2.547) \times 10^{42}$	$3.041(2.813) \times 10^{42}$
	200	$8.262(1.177) \times 10^{36}$	$5.565(1.103) \times 10^{37}$	$1.779(0.543) \times 10^{38}$	$2.150(1.188) \times 10^{43}$	$1.244(0.942) \times 10^{43}$
	250	$2.783(0.164) \times 10^{37}$	$2.290(0.249) \times 10^{38}$	$7.969(1.379) \times 10^{38}$	$8.641(2.862) \times 10^{43}$	$7.455(2.908) \times 10^{43}$
	300	$4.260(0.279) \times 10^{37}$	$3.996(0.460) \times 10^{38}$	$1.475(0.262) \times 10^{39}$	$1.937(0.612) \times 10^{44}$	$1.712(0.572) \times 10^{44}$
	365	$4.576(0.218) \times 10^{37}$	$5.667(0.435) \times 10^{38}$	$2.285(0.268) \times 10^{39}$	$3.864(0.674) \times 10^{44}$	$3.624(0.634) \times 10^{44}$
Jet2-P <sup>a</sup>	150	$2.136(0.710) \times 10^{36}$	$1.447(0.516) \times 10^{37}$	$4.529(2.289) \times 10^{37}$	$5.486(3.883) \times 10^{42}$	$3.041(2.820) \times 10^{42}$
	200	$1.160(0.139) \times 10^{37}$	$8.387(1.527) \times 10^{37}$	$2.887(0.783) \times 10^{38}$	$4.442(1.973) \times 10^{43}$	$4.628(2.118) \times 10^{43}$
	250	$3.461(0.181) \times 10^{37}$	$3.191(0.301) \times 10^{38}$	$1.186(0.181) \times 10^{39}$	$2.244(0.439) \times 10^{44}$	$2.334(0.448) \times 10^{44}$
	300	$4.556(0.286) \times 10^{37}$	$5.015(0.520) \times 10^{38}$	$1.995(0.319) \times 10^{39}$	$4.357(0.884) \times 10^{44}$	$4.210(0.821) \times 10^{44}$
	365	$4.151(0.208) \times 10^{37}$	$6.217(0.464) \times 10^{38}$	$2.746(0.300) \times 10^{39}$	$7.200(0.899) \times 10^{44}$	$6.383(0.832) \times 10^{44}$
f2th20-P <sup>a</sup>	365	$6.133(0.080) \times 10^{37}$	$2.731(0.065) \times 10^{38}$	$9.929(0.039) \times 10^{38}$	$3.087(0.144) \times 10^{44}$	$2.614(0.176) \times 10^{44}$
f3th40-P <sup>a</sup>	365	$2.882(0.055) \times 10^{37}$	$2.611(0.067) \times 10^{38}$	$1.645(0.052) \times 10^{39}$	$1.023(0.030) \times 10^{45}$	$9.531(0.348) \times 10^{44}$

<sup>a</sup> Models Jet2P, f2th20P, f3th40P correspond to the viewing angle along the axis of the enhanced explosion velocities. Jet2E corresponds to the equatorial viewing angle for model Jet2.

TABLE 5.1. Line and continuum fluxes for the four models investigated in this thesis at various epochs.



year, we would need telescopes capable of detecting MeV  $\gamma$ -rays at roughly 10 Mpc (assuming a SNII/SNIb rate of  $\sim 1$  SNU from Cappellarro et al. 1993, and the nearby galaxy blue luminosity function from Nutzman et al. 2004). This requires a sensitivity of  $2 \times 10^{-8}$  phot/s/cm<sup>2</sup> over a 20 keV linewidth. At the current time, proposed plans for an Advanced Compton Telescope have estimated sensitivities of roughly  $1 \times 10^{-7}$  phot/s/cm<sup>2</sup> for a  $3\sigma$  detection in  $10^6$  seconds at 1 MeV (over a 20 keV linewidth; Kurfess 2004). This target sensitivity, had it been available today, would be marginally sufficient to detect the  $^{56}\text{Co}$  MeV decay lines from the recent SN Iip 2004dk (located in NGC 2403 at a distance of roughly 3.5 Mpc). This means that, in the near term, detection in  $\gamma$ -rays of a core-collapse supernova awaits the occurrence of a Galactic supernova. Even being this lucky, from the perspective of probing the class of core-collapse objects, relying on Galactic supernova events will not provide a meaningful sample of core-collapse targets. However, as SN 1987A, with its wealth of data, has shown, a single Galactic event is likely to be worth the wait.

## APPENDIX

Chapter 2 discussed in a general way the physics needed to calculate high energy emission from supernovae using a Monte Carlo transport technique. This appendix discusses in more detail the implementation used by Maverick for the various physical processes introduced in that chapter.

The grid used by Maverick employs a 3-dimensional Cartesian coordinate system. Zones are equally-sized cubes, within which are defined the composition and kinematic properties of the supernova's ejecta. For a grid size of  $140^3$  (2744000 zones) the memory usage is roughly  $2/3 - 3/4$  gigabyte, which is near the maximum resolution that can be used effectively within the one gigabyte of memory available for these Monte Carlo calculations (the SPH simulations were run on the 100-processor Space Simulator cluster at LANL).

In Maverick's analog Monte Carlo radiation transport model, the radiation field is represented by discrete quanta: "photon packets." Each packet represents a given number of photons per time per volume, traveling in a given direction with a given energy. They are a discrete representation of the specific intensity. Packets are released within the supernova ejecta and then followed along their world lines, possibly through multiple interactions with the gas, until they are destroyed by absorption or escape to infinity. The packets which escape are samples from the underlying continuous emergent intensity distribution. They are tallied into bins of energy and direction to form an approximation to the continuous emergent intensity distribution which increases in accuracy as the square root of the number of samples.

The initial locations of these packets are generated randomly within each zone, with the number of packets per zone proportional to the emission rate of radioactive material present in the zone at the given time. The total rate of photon emission in the ejecta is determined, and the weight per packet (the number of photons per

Radioactive Isotope	Mean Lifetime [s]
$^{56}\text{Ni}$	$7.60 \times 10^5$
$^{56}\text{Co}$	$9.63 \times 10^6$
$^{57}\text{Co}$	$3.39 \times 10^7$
$^{44}\text{Ti}$	$2.73 \times 10^9$
$^{22}\text{Na}$	$1.19 \times 10^8$

TABLE 5.2. Lifetimes for the radioactive isotopes included in Maverick.

second each packet represents) is determined by dividing the total emission rate by the number of packets to follow. The number of packets emitted in each zone is then simply the emission rate in the zone divided by the packet weight. The emission rate is calculated in the observer frame of the material and does not account for the time dilation effect discussed in Chapter 2. Furthermore, the emission rate in each zone is calculated at the model time, with no correction for the delay in escape from the ejecta arising from the packet's time to escape or destruction.

A packet's initial four-momentum (energy and direction cosines) is sampled in the co-moving frame of the zone in which it is emitted. The direction is chosen from a uniform distribution in solid angle (corresponding to isotropic emission in the fluid frame). Three direction cosines, corresponding to the angles from each of the coordinate directions, are retained to simplify distance calculations within the ejecta.

The emission energy is chosen from one of the decay lines, with a probability given by the branching ratios listed in Browne, Dairiki & Doebler (1978) for the radioactive species  $^{56}\text{Ni}$ ,  $^{56}\text{Co}$ ,  $^{57}\text{Co}$ ,  $^{44}\text{Ti}$  and  $^{22}\text{Na}$ . The decay lifetimes used in Maverick for  $^{56}\text{Ni}$ ,  $^{57}\text{Co}$ , and  $^{22}\text{Na}$  were taken from Browne, Dairiki & Doebler (1978). Lifetimes for  $^{56}\text{Co}$  and  $^{44}\text{Ti}$  were adopted from Junde et al. (1999) and Gorres et al. (1998) respectively. (See Table 5.2 for a summary of adopted lifetimes.)

Once created, the packet is then boosted to the observer's frame, using the fully-

relativistic expressions

$$\hat{\mu}_o = \frac{\epsilon}{\epsilon_o} \left[ \hat{\mu} - \gamma \frac{\vec{v}}{c} + \frac{\gamma^2}{\gamma + 1} \frac{\vec{v}}{c} \frac{\hat{\mu} \cdot \vec{v}}{c} \right] \quad (5.1)$$

$$\frac{\epsilon_o}{\epsilon} = \gamma \left( 1 - \frac{\hat{\mu} \cdot \vec{v}}{c} \right) \quad (5.2)$$

(Mihalas & Mihalas 1984) with  $\vec{v}$  the velocity of the material,  $\gamma = 1/\sqrt{1 - v^2/c^2}$ , and  $\hat{\mu}$  the unit direction vector for the packet (with component values equal to the direction cosines along each coordinate axis).  $\epsilon$  is the packet energy, and the subscript “o” denotes quantities defined in the co-moving fluid frame.

For the subsequent fate of each packet, motion through space is computed in the observer frame, and all interactions are treated in the co-moving frame. This allows the simulation to take into account Doppler, advection, and aberration effects due to the differential velocity in the expanding supernova ejecta while allowing the simpler computation of trajectories in the observer frame and of local interaction physics in the co-moving frame (where the opacities are isotropic). No account is taken of the density evolution during the flight time of the packet; as noted in Chapter 2, at the late times considered here, this effect is negligible. The computation can easily be modified to take this effect into account, however.

Once emitted, photon packets propagate through the Cartesian mesh in the observer frame along straight-line trajectories until they encounter one of three “events”. When the packet reaches the edge of the current zone, the composition and velocity of the medium change. This changes the opacity experienced by the packet, and thus the opacity must be recomputed by boosting to the local frame, computing the co-moving opacity, and then boosting this quantity back to the observer’s frame. When the packet has traveled the distance to the next interaction, it must undergo an absorption or scattering by the material, changing its intensity, energy, and direction. When the packet reaches the edge of the ejecta, it leaves the problem space and we no longer need to track its trajectory, but must consider how to tally its properties

into observable quantities.

In *Maverick*, the fate of each packet is followed in a loop which starts by determining which event will occur first; which is nearest along the packet's direction of flight. The distance to the next interaction is determined from the decrease in specific intensity  $I$  with optical depth  $\tau$ :  $\partial I / \partial \tau = -I$ . The probability density of scattering within optical depth  $(\tau, \tau + d\tau)$  is thus  $e^{-\tau}$ . This is easily sampled by inversion from the cumulative distribution  $P(\tau) = \int_0^\tau e^{-\tau'} d\tau' = 1 - e^{-\tau}$ , as  $\tau = -\ln(1 - \xi) = -\ln(\xi')$ , where  $\xi$  is a uniform random number on  $(0, 1)$ . For our uniprocessor runs, these were generated with the **ran2** generator from Press et al. (1988); parallel computing considerations are discussed below. Given the optical depth  $\tau_i$  to the next interaction, we must integrate the optical depth along the chosen trajectory to determine the physical distance to travel. In *Maverick*, this is done in the following loop.

The total extinction coefficient,  $\chi_{tot}$ , is determined in the photon's current zone. This is done by boosting the photon energy to the co-moving frame at the zone's velocity, interpolating in the tables discussed in Chapter 2 to find the opacity at this energy, and then boosting the opacity back to the observer frame:  $\chi(\mu, \epsilon) = (\epsilon_0/\epsilon)\chi_0(\epsilon_0)$ . This value of the observer-frame opacity is then assumed to hold throughout the zone. For 140 zones per direction, the velocity across a zone is roughly 1/70 of the maximum velocity, or about 150 km/s, a 0.05% change in the comoving energy of the photon. For the continuous opacities of interest to  $\gamma$ -ray transport, this is a reasonable approximation: if the opacity were to vary with energy as the hydrogenic  $E^{-3}$ , this is a 0.1% change in opacity. Were we to consider more sharply varying opacities such as lines, we would need to employ a more accurate prescription for integrating the opacity across a zone.

With  $\chi_{tot}$ , the optical depth across the zone  $\tau_{bdry}$  is simply the width of the zone along the trajectory,  $d_{bdry}$ , times  $\chi_{tot}$ . If this optical depth is greater than the remaining optical depth to interaction  $\tau_i$ , the photon is moved a distance  $d_i = \tau_i / \chi_{tot}$  within the zone and an interaction is then simulated. If  $\tau_i > \tau_z$ , then the photon

is moved to the intersection of the trajectory with the next zone boundary and  $\tau_i$  is decremented by  $\tau_{bdry}$ . The opacity for the new zone is then determined and the process repeated in subsequent zones until the remaining  $\tau_i < \tau_{bdry}$  or the photon escapes the ejecta.

Once the photon packet has arrived at the site of the next interaction, the type of the interaction is determined. Three types are considered in the current simulations, each with its own extinction coefficient: photoelectric absorption ( $\chi_{pe}$ ), pair production ( $\chi_p$ ), and Compton scattering ( $\chi_c$ ), with  $\chi_{tot} = \chi_{pe} + \chi_p + \chi_c$ . Which interaction occurs is determined in proportion to the fraction of the total opacity contributed by each process. The unit interval is divided into three,  $[0, \chi_{pe}/\chi_{tot})$ ,  $[\chi_{pe}/\chi_{tot}, (\chi_{pe} + \chi_p)/\chi_{tot})$ , and  $[(\chi_{pe} + \chi_p)/\chi_{tot}, 1)$ . A uniform random number  $\xi$  is generated, and the process to be followed is chosen by the subinterval in which this number lies. For example, if each interaction contributed a third of the total opacity, then for  $1/3 \geq \xi < 2/3$ , pair production would be chosen.

For the photoelectric and pair production interactions, the photon packet is lost to absorption at the interaction site. The version of Maverick used for these simulations does not keep track of this deposition event, but moves directly to creating a new photon packet. If the interaction is chosen to be Compton scattering, a new packet direction and energy are chosen from the Klein-Nishina distribution. This is accomplished via a multi-step sampling technique proposed by Kahn (1954). The technique is a combination inversion/rejection technique with unequal weighting for these two samples, and is accomplished as follows:

- Draw three random numbers  $\xi_1, \xi_2, \xi_3$
- Is  $\xi_1 > \frac{1+2E}{9+2E}$ ? (where  $E$ =photon energy in units of  $m_o c^2$ )
- If Yes, follow branch 1 and define  $R = \frac{1+2E}{1+2\xi_2 E}$ .  
Else follow branch 2 and define  $R = 1 + 2\xi_2 E$ .

- Branch 1: if  $\xi_3 \leq \frac{1}{2} \left[ \left( \frac{1-R}{E} + 1 \right)^2 + \frac{1}{R} \right]$ , then outgoing energy is equal to  $\frac{1}{R}$  times the incoming energy, otherwise start over by choosing a different set of 3 random numbers.
- Branch 2: if  $\xi_3 \leq \frac{4}{R} \left( 1 - \frac{1}{R} \right)$ , then outgoing energy is equal to  $\frac{1}{R}$  times the incoming energy, otherwise start over by choosing a different set of 3 random numbers.

Given an incoming energy, this process yields an outgoing energy sampled from the Klein-Nishina distribution. Eqn. 2.6 then gives the angle of scattering given these two energies, and the remaining azimuthal angle of scattering is sampled uniformly. All of these quantities are defined in the co-moving frame of the zone. The packet's direction cosines are then rotated through the angle of scattering, the packet is boosted back into the observer frame, a new interaction optical depth  $\tau_i$  is sampled, and the process of moving the packet through the ejecta continues.

If at any time the packet's new position places it outside the ejecta radius, the packet has escaped. The "edge" of the ejecta is defined by  $R_{ej} = \frac{N_{x,y,z}}{2} \times L_{zone}$ , where  $L_{zone}$  is the length of each zone and  $N_{x,y,z}$  is the number of zones along the x, y, or z direction. The emergent packet is then tallied into a set of observables. For the simulations discussed here, packet properties were tallied into global spectra (summed over the entire ejecta) and angular spectra (summed over a subset of emerging angles). The global spectral properties were tallied into 250 coarse energy bins (logarithmically spaced). Energy bins near the decay line energies were further refined to adequately resolve the line profile shapes (50 refined bins per coarse bin; those bins with bin energies within 7000 km/s of the decay line energy were refined to the higher energy resolution.) Packet properties which were tallied include number of packets escaped and luminosity of packet (units of photons per second). For equal luminosity-weighted packets, the square root of the number of escaped packets gives the  $1\sigma$  errors for the Monte Carlo determined luminosities. These errors are largest for the angular spectra,

which tally only a subset of the total escaped packets. The angular bins are spaced at  $18^\circ$  intervals along the polar angle, resulting in 11 angular bins spanning the  $180^\circ$  between the positive z-axis and the negative z-axis. The angular tallies include all escaping packets with direction vectors within  $5^\circ$  of the defined bin direction. The width of the bin was chosen to achieve minimum signal-to-noise values of roughly 3 in the decay line energy bins.

In general, radiation transport through a scattering medium is a boundary-value problem in which, in principle, all zones can communicate with all other zones (unlike hydrodynamics in which zones only communicate with nearest neighbors). This property makes it very difficult in general to design parallel algorithms for radiation transport. One attractive property of a Monte Carlo approach is its ease of parallelism, at least when a copy of the entire problem grid will fit in the memory of each processor. One can simply run multiple copies of the problem independently, and add the results at the end. There is no communication between processors, and the speed-up which results is the optimum of a factor of  $N$  for  $N$  processors. The only subtlety is that one must be sure that the runs of random numbers generated for each process are mutually independent, for which a large class of parallel random number generators is available.



## REFERENCES

- [1] Ait-Ouamer, A.D. et al. 1990, in Proceedings of the 21st International Cosmic Ray Conference, University of Adelaide Press, Vol. 2, 183
- [2] Ambwani, K. & Sutherland, P. 1988, ApJ, 325, 820
- [3] Arnett, W. D., Bahcall, J. N., Kirshner, R. P., & Woosley, S. E. 1989, ARA&A, 27, 629
- [4] Arras, P. & Lai, D., 1999, ApJ, 519, 745
- [5] Arzoumanian, Z., Chernoff, D. & Cordes, J., 2002, ApJ, 568, 289
- [6] Ashworth, W., 1980, Journal Hist. Astron., 11, 1
- [7] Bazan, G., & Arnett, D 1998, ApJ, 496, 316
- [8] Blinnikov, S. I., Dunina-Barkovskaya, N. V., & Nadyozhin, D. K. 1996, ApJS, 106, 171
- [9] Blondin, J., Mezzacappa, A. & DeMarino, C., 2003, ApJ, 584, 971
- [10] Browne, E., Dairiki, J.M., & Doebler, R.E. 1978, Table of Radioactive Isotopes, Eds. C.M. Lederer, & V.S. Shirley, John Wiley & Sons, p. 160
- [11] Browne, E. & Firestone, R.B. 1986, Table of Radioactive Isotopes, Ed. V.S. Shirley, John Wiley & Sons, p. 56-2
- [12] Brown, B.L., & Leventhal, M. 1987, ApJ, 319, 637
- [13] Burbidge, M., Burbidge, G., Fowler, W., & Hoyle, F. 1957, RvMP, 29, 547
- [14] Burrows, A. & The, L.-S. 1990, ApJ, 360, 626
- [15] Burrows, A., Hayes, J., & Fryxell, B. A. 1995, ApJ, 450, 830
- [16] Burrows, A. & Van Riper, K. 1995, ApJ, 455, 215
- [17] Burrows, A., & Hayes, J. 1996, PRL, 76, 352
- [18] Bussard, R.W., Burrows, A., The, L.-S. 1989, ApJ, 341, 401
- [19] Cappellaro, E., Turatto, M., Benetti, S., Tsvetkov, D.Yu., Bartunov, O., & Makarova, I. 1993, ApJ, 273, 383
- [20] Chan, K.-W., & Lingenfelter, R.E. 1987, ApJ, 318, L51

- [21] Chan, K.-W., & Lingenfelter, R.E. 1991, ApJ, 368, 515
- [22] Chatterjee, S., & Cordes, J. 2002, ApJ, 575, 407
- [23] Chevalier, R. A., & Klein, R. I. 1978, ApJ, 269, 281
- [24] Chevalier, R. A., & Soker, N. 1989, ApJ, 341, 867
- [25] Chugai, N. 1991, SvAL, 17, 400
- [26] Clayton, D.D., Colgate, S.A., Fishman, G.J. 1969, ApJ, 155, 75
- [27] Clayton, D.D., & The, L.-S. 1991, ApJ, 375, 221
- [28] Colgate, S. A., Petschek, A. G., Kriese, J. T. 1980, ApJ, 237, L81
- [29] Colgate, S., & McKee, C. 1969, ApJ, 157, 623
- [30] Cook, W. R., Palmer, D. M., Prince, T. A., Schindler, S. M., Starr, C. H., & Stone, E. C. 1988, ApJ, 334, L87
- [31] Dotani, T., Hayashida, K., Inoue, H., Itoh, M., & Koyama, K. 1987, Nature, 330, 230
- [32] Ebisuzaki, T., & Shibazaki, N. 1988, ApJ, 327, 5
- [33] Fesen, R., Becker, R. & Blair, W., 1987, ApJ, 313, 378
- [34] Firestone, R.B. 1996, 8th Table of Isotopes, Ed. V.S. Shirley, John Wiley & Sons, p. 249
- [35] Fansson, C., & Kozma, C. 1993, ApJL, 408, L25
- [36] Fryer, C., Burrows, A. & Benz, W., 1998, ApJ, 496, 333
- [37] Fryer, C. L., & Heger, A. 2000, ApJ, 541, 1033
- [38] Fryer, C. L., & Kalogera, V. 2001, ApJ, 554, 548
- [39] Fryer, C., & Warren, M. 2002, ApJ, 574, 65
- [40] Fryer, C., 2004, ApJ, 601L, 175
- [41] Gehrels, N., MacCallum, C., & Leventhal, M. 1987, ApJL, 320, L19
- [42] Gorres, J., Meissner, J., Schatz, H., Stech, E., Tischhauser, P., Wiescher, M., Bazin, D, et al. 1998, PhRvL, 80, 2554

- [43] Grant, K. J. & Dean, A. J., 1993, A&AS 97, 211
- [44] Grebenev, S. A. & Sunyaev, R. A., 1987, SvAL, 13, 397
- [45] Haas, M. R., Erickson, E. F., Lord, S. D., Hollenbach, D. J., Colgan, S. W. J., & Burton, M. G. 1990, ApJ, 360, 257
- [46] Hamuy, M. 2003, ApJ, 582, 905
- [47] Harris, M.J., Teegarden, B.J., Cline, T.L., Gehrels, N., Palmer, D.M., Ramaty, R., & Seifert, H. 1998, ApJL, 501, L55.
- [48] Herant, M., & Benz, W. 1992, ApJ, 387, 294
- [49] Herant, M., & Woosley, S.E. 1994, ApJ, 425, 814
- [50] Herant, M., Benz, W., Hix, W.R., Fryer, C.L. & Colgate, S.A. 1994, ApJ, 435, 339
- [51] Herant, M., 1995, SSRv, 74, 335
- [52] Hermesen, W., & Winkler, C. 2002, in The Gamma Ray Universe, Proc. 22nd Moriond Astrophysics Meeting, ed. A. Goldwurm, D. Neumann, & J. Trân Thanh Vân (Hanoi: Thê Giói)
- [53] Hoffman, R., Woosley, S, Weaver, T., Timmes, F., Eastman, R., & Hartmann, D. 1995, in The Gamma Ray Sky with Compton GRO and SIGMA, ed. M. Signore, P. Salati, & G. Vedrenne (Dordrecht: Kluwer), 267
- [54] Höflich, P., 1991, A&A, 246, 481
- [55] Höflich, P., Khokhlov, A., Müller, E. 1992, A&A, 259, 549
- [56] Höflich, P., Khokhlov, A., & Wheeler 1995, ApJ, 444, 831
- [57] Höflich, P., & Khokhlov, A. 1996, ApJ, 457, 500
- [58] Höflich, P., Wheeler, J. C., & Khokhlov, A. 1998, ApJ, 492, 228
- [59] Höflich, P., Wheeler, J. C., & Thielemann, F.-K. 1998, ApJ, 495, 617
- [60] Höflich, P. 2002, *New Astronomy Reviews*, 46, 475
- [61] Höflich, P., & Wheeler, J., C. 2004, ApJ, 605, 573
- [62] Hubbell, J. H., 1969, NSRDS-NBS 29
- [63] Hungerford, A.L., Fryer, C.L., Warren, M.S. 2003, ApJ, 594, 390

- [64] Itoh, M., Kumagai, S., Shigeyama, T., Nomoto, K., & Nishimura, J. 1987, *Nature*, 330, 233
- [65] Hwang, U., Laming, J.M., Badenes, C., et al. 2004, *ApJL*, in press.
- [66] Isern, J., Gómez-Gomar, J., Bravo, E., & Jean, P. 1996, in *Proceedings of the 2nd INTEGRAL Workshop*, Eds. C. Winkler, J.-L. Courvoisier, Ph. Douchoux, ESA, p. 89
- [67] Iwabuchi, K. & Kumagai S. 2001, *PASJ*, 53, 669
- [68] Iyudin, A., Diehl, R., Bloemen, H., Hermsen, W., Lichti, G., Morris, D., Ryan, J., Schoenfelder, V., Steinle, H., Varendorff, M., de Vries, C. & Winkler, C., 1994, *A&A*, 284, L1
- [69] Iyudin, A., 1997, *Nuclear Phys. A*, 654, 900c
- [70] Janka, H.-T. & Mönchmeyer, R., 1989, *A&A*, 209, L5
- [71] Janka, H.-Th., & Müller, E. 1996, *A&A*, 306, 167
- [72] Junde, H. 1999, *Nucl. Data Sheets*, 86, 315
- [73] Kahn, H. 1954, U.S. Atomic Energy commission Report AECU-3259, p. 39
- [74] Kazaryan, S.M. et al. 1990, in *Proceedings of the 21st International Cosmic Ray Conference*, University of Adelaide Press, Vol. 2, 187
- [75] Khokhlov, A.M., Höflich, P.A., Oran, E.S., Wheeler, J.C., Wang, L., Chtchelkanova, A. Yu. 1999, *ApJ*, 524, L107
- [76] Kinzer, R.L. et al. 2001, *ApJ*, 559, 282
- [77] Kumagai, S., Shigeyama, T., Nomoto, K., Itoh, M., & Nishimura, J. 1988, *A&AL*, 197, L7
- [78] Kumagai, S., & Nomoto, K. 1997, in *Proceedings of the NATO ASI on Thermonuclear SNe (C486)*, eds. P. Ruiz-Lapuente, R. Canal, & J. Isern, Kluwer, Dordrecht, p. 515
- [79] Kumagai, S., Iwabuchi, K., & Nomoto, K. 1999, in *Proceedings of Astronomy with Radioactivities III (MPE Report 274)*, eds. R. Diehl & D. Hartmann, Max-Planck Institute for Extra-terrestrial Physics, p. 181
- [80] Kurfess, J. 2004, *NewAR*, 48, 177
- [81] Lai, D. 2000, *ApJ*, 540, 946

- [82] Lederer, C.M., Hollander, J.M., & Perlman, I. 1967, 6th Table of Isotopes, John Wiley & Sons, p. 189
- [83] Leising, M. 1988, *Nature*, 332, 516
- [84] Leonard, D. C., & Filippenko, A. V. 2001, *PASP*, 113, 920
- [85] Livio, M. 2000, in *Type Ia Supernovae, Theory and Cosmology*, ed. J. Niemeyer & J. Truran (Cambridge University Press), 33
- [86] Mahoney, W. A., Varnell, L. S., Jacobson, A. S., Ling, J. C., Radocinski, R. G., & Wheaton, Wm. A. 1988, *ApJ*, 334, L81
- [87] Matz, S. M., Share, G. H., Leising, M. D., Chupp, E. L., & Vestrand, W. T. 1988, *Nature*, 331, 416
- [88] McCray, R. 1993, *ARA&A*, 31, 175.
- [89] McCray, R., Shull, J.M., Sutherland, P. 1987, *ApJ*, 317, 73.
- [90] Mihalas, D., & Mihalas, B. 1984, *Foundations of Radiation Hydrodynamics*, Oxford University Press
- [91] Milne, P., The, L.-S., & Leising, M. 1999, *ApJS*, 124, 503
- [92] Milne, P., Kroeger, R., Kurfess, J., & The, L.-S. 2002, *NewAR*, 46, 617
- [93] Mochizuki, Y., Takahashi, K., Janka H.-TH., Hillebrandt, W., Diehl, R. 1999, *A&AS*, 346, 831
- [94] Mönchmeyer, R. & Müller, E., 1989, in *NATO ASI series, Timing Neutron Stars*, ed. H. Ögelman & E.P.J. van den Heuvel (New York: ASI)
- [95] Müller, E., Höflich, P. & Khokhlov, A. 1991, *A&A*, 249, L1
- [96] Nagataki, S., Shimizu, T.M., & Sato, K. 1998a, *ApJ*, 495, 413
- [97] Nagataki, S., Hashimoto, M., Sato, K., Yamada, S. & Mochizuki, Y., 1998b, *ApJ*, 492, L45
- [98] Nagataki, S. 2000, *ApJS*, 127, 141
- [99] Nomoto, K., Thielemann, F., & Yokoi, K. 1984, *ApJ*, 286, 644
- [100] Nutzman, P., Kalogera, V., Finn, L. S., Hendrickson, C., & Bleczynski, K. 2004, *astro-ph/0402091*
- [101] Ore, A., & Powell, J. 1949, *Phys. Rev.*, 75, 1696

- [102] Perlmutter, S., Aldering, G., Goldhaber, G., et al. 1999, ApJ, 517, 565
- [103] Pinto, P. A., & Woosley, S. E. 1988a, ApJ, 329, 820
- [104] Pinto, P. A., & Woosley, S. E. 1988b, Nature, 333, 534
- [105] Pinto, P.A., Eastman, R., Rogers, T. 2001, ApJ, 551, 231
- [106] Plechaty, E., Cullen, D. & Howerton, R., 1981, LLNL Rep. UCRL-50400, Vol. 6(rev. 3[1987])
- [107] Podsiadlowski, P., Nomoto, K., Maeda, K., Nakamura, T., Mazzali, P., & Schmidt, B. 2002, ApJ, 567, 491
- [108] Press, W., Flannery, B., Teukolsky, S., & Vetterling, W. 1988, *Numerical Recipes in C*, Cambridge University Press
- [109] Raeside, D., E. 1976, Phys. Med. Biol., 21, 181
- [110] Reed, J., Hester, J, Fabian, A. & Winkler, P., 1995, ApJ, 440, 706
- [111] Rester, A.C. et al. 1989, ApJ, 342, L71
- [112] Scheck, L., Plewa, T., Janka, H.-Th., Kifonidis, K., Müller, E., 2004, PhRvL, 1992, 011103
- [113] Spyromilio, J., Meikle, W. P. S., & Allen, D. A. 1990, MNRAS, 242, 669
- [114] Sunyaev, R., Kaniovskii, A., Efremov, V., Gilfanov, M., & Churazov, E. 1987, Nature, 330, 227
- [115] Sunyaev, R., Kaniovskii, A., Efremov, V., Grebenev, S., Kuznetsov, A., Engelhauser, J., Döbereiner, S., Pietsch, W., Reppin, C., Tuümpfer, J., Kendziorra, E., Maisack, M., Mony, B., & Staubert, R., 1990, Soviet Astron. Lett., 16(3), 171
- [116] Teegarden, B., Barthelmy, S., Gehrels, N., Tueller, J., & Leventhal, M. 1989, Nature, 339, 122
- [117] The, L.-S., Burrows, A., & Bussard, R. 1990, ApJ, 352, 731
- [118] Timmes, F., Woosley, S., Hartmann, D. & Hoffman, R. 1996, ApJ, 464, 332
- [119] Timmes, F., Hoffman, R. & Woosley, S., 2000, ApJS, 129, 377
- [120] Tueller, J., Barthelmy, S., Gehrels, N., Teegarden, B. J., Leventhal, M., & MacCallum, C. J. 1990, ApJ, 351, L41

- [121] Turatto, M., Mazzali, P. A., Young, T. R., Nomoto, K., Iwamoto, K., Benetti, S., Cappallaro, E., Danziger, I. J., de Mello, D. F., Phillips, M. M., Suntzeff, N. B., Clocchiatti, A., Piemonte, A., Leibundgut, B., Covarrubias, R., Maza, J., Sollerman, J. 1998, *ApJ*, 498, L129
- [122] Umeda, H. & Nomoto, K. 2002, *ApJ*, 565, 385
- [123] Utrobin, V., Chugai, N., & Andronova, A. 1995, *A&A*, 295, 129
- [124] Veigele, W. J., 1973, *Atomic Data Tables* 5, 51
- [125] Vink, J., Laming, J. M., Kaastra, J., Bleeker, J., Bloemen, H. & Oberlack, U., 2001, *ApJ*, 560, L79
- [126] Wang, L., Howell, D. A., Höflich, P., Wheeler, J. C. 2001, *ApJ*, 556, 302
- [127] Warren, M. S. & Salmon, J. K. 1993, *Supercomputing '93*, IEEE Comp. Soc, pg. 12
- [128] Weaver, T. A., & Woosley, S. E. 1980, in *AIP Conf. Proc.* 63, *Supernovae Spectra*, ed. R. Meyerott & G. H. Gillespie (New York: AIP), 15
- [129] Weaver, T. A., & Woosley, S. E. 1993, *Phys. Rep.*, 227, 65
- [130] Witteborn, F.C., Bregman, J.D., Wooden, D.H., Pinto, P.A., Rank, D.M., Woosley, S.E., & Cohen, M. 1989, *ApJL*, 338, L9
- [131] Woosley, S., Arnett, D., & Clayton, D. 1973, *ApJS*, 26, 231
- [132] Woosley, S. E. 1988, *ApJ*, 330, 218
- [133] Woosley, S., Pinto, P., & Ensman, L. 1988, *ApJ*, 324, 466
- [134] Xu, Y., Sutherland, P., McCray, R., & Ross, R. 1988, *ApJ*, 327, 197
- [135] Woosley, S., & Weaver, T. 1995, *ApJS*, 101, 181